9-13-2019

Numerical Simulation of Unstable Laser Resonators with a High Gain Medium

Robert L. Lloyd

NUMERICAL SIMULATION OF UNSTABLE LASER RESONATORS WITH A HIGH GAIN MEDIUM

DISSERTATION

Robert L. Lloyd, Captain, USAF

AFIT/GAP/ENP/16-19

DEPARTMENT OF THE AIR FORCE
AIR UNIVERSITY

AIR FORCE INSTITUTE OF TECHNOLOGY

Wright-Patterson Air Force Base, Ohio

AFIT/GAP/ENP/16-19

NUMERICAL SIMULATION OF UNSTABLE LASER RESONATORS WITH A HIGH GAIN MEDIUM

DISSERTATION

Presented to the Faculty

Graduate School of Engineering and Management

Air Force Institute of Technology

Air University

Air Education and Training Command

in Partial Fulfillment of the Requirements for the

Degree of Philosophy of Science in Applied Physics

Robert L. Lloyd, B.S. Physics, M.S. Engineering Physics

Captain, USAF

13 September 2019

AFIT/GAP/ENP/16-19

NUMERICAL SIMULATION OF UNSTABLE LASER RESONATORS WITH A HIGH GAIN MEDIUM

DISSERTATION

Robert L. Lloyd, B.S. Physics, M.S. Engineering Physics
Captain, USAF

Committee Membership:

Dr. D. E. Weeks, PhD
Chairman

Dr. G. P. Perram, PhD
Member

Lt Col J. R. Komives, PhD
Member

ADEDJI B. BADIRU, PhD
Dean, Graduate School of Engineering and Management

AFIT/GAP/ENP/16-19

Abstract

This research focused on the numeric simulation of unstable laser resonators with high gain media. In order to accomplish the research, the modes and eigenvalues for various bare cavity resonator were computed followed by modes of a resonator in the presence of gain. Using a Fourier Split Step Method in a Fox and Li iteration scheme, different laser outputs for various laser cavities with gain were computed. Various parameters defining positive branch confocal unstable resonators were chosen corresponding to four studies. The four studies focused on modifying laser cavity Fresnel number, gain medium parameters, gain cell position, and gain cell length from a baseline laser cavity geometry. It was observed that the highest laser cavity efficiencies occurred when the laser cavity had a Fresnel number greater than 7 and was positioned at the back larger mirror of an unstable resonator. Longer gain cell lengths were found to correspond to higher beam qualities. Beam quality was found to be inversely related to laser efficiency. A theory for modifying simple laser models based upon a mode volume was derived and supported the results of the gain wave-optic simulations.

Table of Contents

Page

List of Figures

List of Abbreviations

ASE Amplified Spontaneous Emission.

ASM Angular Spectrum Method.

CFD Computational Fluid Dynamics.

DEM Direct Eigenvector Method.

DoD Department of Defense.

DPAL Diode Pumped Alkali Laser.

FFP Fresnel Forward Propagator.

FFT Fast Fourier Transform.

FSSM Fourier Split Step Method.

HELS High Energy Laser Systems.

NIST National Institute of Standards and Technology.

ODE Ordinary Differential Equation.

PDE Partial Differential Equation.

USAF United States Air Force.

VPIB Vertical Power in the Bucket.

NUMERICAL SIMULATION OF UNSTABLE LASER RESONATORS
WITH A HIGH GAIN MEDIUM

I. Introduction

To maintain aerial supremacy, the Air Force requires the next generation of weapons to be superior to current technology. High Energy Laser Systems (HELS) are a future type of weapon system with the potential of ensuring United States Air Force (USAF) superiority on the battlefield. To support this endeavor, the focus of the dissertation research will be on the numerical modeling of Diode Pumped Alkali Laser (DPAL) systems, a contending technology for high energy lasing applications.

The following chapter summarizes the reasoning behind the future importance of HELS within the Air Force, the history of DPAL weapon system development, the basics of DPAL operation, an example DPAL system that will be used throughout the rest of the document, a summary of previous DPAL modeling efforts, and the specific thrust of this research in modeling unstable resonators with a high gain medium.

A Requirement for Diode Pumped Alkali Laser (DPAL) Systems

In order to understand the need for DPAL technology, one must understand the history of laser technology. The laser was initially created in 1960 using a ruby lasing material. Since then, many different forms of lasers have been developed for a wide variety of applications, including sensing, communication, fabrication, and defense. For the purpose of this research, the focus will be on the last example with the idea of the laser being used as a defense/attack weapon. A weapon that uses either electromagnetic or sonic energy to kill or disable a target is a Directed Energy

weapon. The military has long been interested in a Directed Energy weapon that would either be used synergistically with modern kinetic energy weapons (munitions, missiles) or fielded as a solo device[1]. The reason behind this interest lies within the three promises of electromagnetic Directed Energy weapons:

- The promise of precision strike
- The promise of speed of light delivery
- The promise of an unlimited magazine

The Department of Defense (DoD) is very interested in the capability to deliver maximum destruction at a precise point. A high power laser system would further this capability to place destructive energy on a target many miles away, limited fundamentally by the diffraction of the light across the intervening distance following the far-field Airy Disk pattern, given by

$$\theta = \frac{1.22\lambda}{D}\,, \tag{1}$$

where λ is the wavelength of the associated light which tends to be on the order of 1 μm and D is the aperture of the optical system output which tends to be on the order of ≈ 10 cm. Equation (1) means that light from the hypothetical device is still focusable to under a meter at a distance 50 miles away from the device. This range of HELS, make them ideal for long range strategic applications, such as missile, base or aircraft defense[2].

The next promise of directed energy weapon systems is the capability of speed of light delivery on a target. Any energy delivered using the electromagnetic spectrum travels at the maximum speed of any known object in the universe. The speed of light greatly outstrips any convectional munition and even unconventional ones. By

comparison, hypersonic vehicles travel a little over a hundredth thousandth the speed of light. In other words, compared to directed energy, every other munition remains still on the battlefield.

Finally, directed energy promises the logistical dominance of an unlimited magazine. Lasers and other directed energy weapons may easily be powered electrically, which means that the cost of firing a directed energy weapon is essentially a few dollars for a shot. Lasers could be the key to winning the logistics battle in future wars.

Although directed energy systems hold much promise, they are also plagued by their own inherent issues. The first is that in regards to warfare, electromagnetic weapons are centuries behind kinetic weapons in terms of battlefield usage, meaning that tactics and strategies for warfare will need to be updated for proper use of Directed Energy weapon systems. Directed energy is also a new technology, leading to an initially large research and development cycle to deliver on the promises described above. Prior research systems, in the form of chemically pumped lasers, did not deliver on the unlimited magazine promise of HELS. They were also dangerous to operate, using chemicals for the laser gain that tended to not only be toxic, but had to be vented directly into the environment to work properly. Newer systems, such as fiber and solid state lasers deliver on the promise of an unlimited magazine, but fail to provide the power output needed to truly be lethally effective at a distance. These newer systems tend to deliver energy on the order of a tens of kilowatts where an effective system would require at least $50 - 100\,\mathrm{kW}$ output power to be effective on the battlefield. The reasoning behind this lack of power output usually comes from thermal management issues occurring at the lasing source (and other less pronounced effects occurring with these lower powered sources). From the current impasse seen

between these two systems, DPALs emerged as a contender into the Directed Energy environment.

A Quick History of Diode Pumped Alkali Laser (DPAL)

Optically pumped alkali systems were originally proposed as one of the first laser systems in 1958[3]. The system employed potassium pumped optically using a potassium lamp that was filtered to remove red radiation. Although theoretically feasible, the actual laser ran into difficulties in production because of the reactiveness of the alkali and the inability to get a strong violet source to excite the potassium vapor. Due to these difficulties, alkali systems were not the first lasing system, but were experimentally verified in 1962 by a cesium alkali laser pumped with a helium lamp[4]. Rabinowitz's system[4] was the first gaseous laser that utilized optical pumping, but despite this first, the experiment had a low output power of 50 μW for an 800 W pump power input. The low efficiency was understandable because of the wide spectrum associated with the optical pump and low system pressure ($\sim$ 4 Torr) available for widening the potassium absorption line. After the development of narrower pumps, the potential gain of alkali systems were realized with a series of "cavity-less" cesium and rubidium experiments completed by Sharma and Bhaskar in 1981[5]. The overall power output of the lasing system was low, but paved the way for the current incarnation of the optically pumped alkali systems present currently. Alkali systems were still pursued because of their high quantum efficiencies, 95.3% for cesium, 98.1% for rubidium, and 99.6% for potassium, compared to a typical 76% operating efficiency associated with Nd:YAG which had a similar efficiency for almost all other solid state laser media[6]. However, the laser systems with an alkali media overall power output would remain low until lasers replaced flash lamps for optical pumping in 2003.

In 2003, William Krupke filed a patent[7] for a new laser system consisting of an alkali vapor buffered with rare-gases and hydrocarbons. The lasing system was dedicated to the first three energy levels of alkalis, $^2P_{3/2}$, $^2P_{1/2}$, and $^2S_{1/2}$, with helium presented as a buffer gas to facilitate the spin transition between $^2P_{3/2}$ and $^2P_{1/2}$. The largest innovation was the use of a titanium sapphire laser to pump the gain medium which increased the efficiency of the system. The actual system created by Krupke had a 54% conversion efficiency compared to the pump[8]. However, in the actual experiment, ethane was added to the system. The use of hydrocarbons are only required for a cesium alkali because of the energy difference of the $6^2P_{3/2} \rightarrow 6^2P_{1/2}$ fine-structure mixing transition. Hydrocarbons are not a requirement for DPAL using rubidium or potassium as the alkali material. The study by Krupke and Beach was also the first to have demonstrated a parameter scan across pump power despite a 20% output coupling associated with the cavity[9].

Since Krupke's initial demonstration, DPAL systems have become a prime candidate for the future of lasing systems representing a quick path forward toward high power applications that require high beam quality.

What is a Diode Pumped Alkali Laser (DPAL)

The goal of this research is further investigation of the basic physics within the various components of the DPAL system, with the end goal of determining method to increase system performance. An understanding of the DPAL system may be gained from looking individually at two structures within the laser system

1. The Gain Medium

2. The Resonator

A diagram of the layout of these two system structures are shown in figure 1.

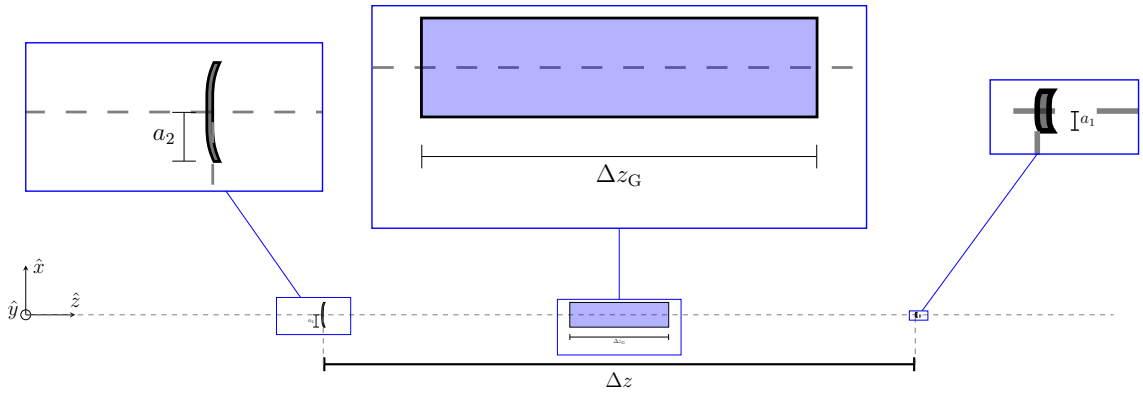

Figure 1. DPAL system layout, with the gain medium, marked in blue, with the laser cavity along the $\hat{z}$ axis, and the pump propagated along the $\hat{z}$ axis. The mirrors in the diagram indicate an unstable resonator structure.

The gain medium used for this research is a uniform mixture of helium and vaporized rubidium. As in other laser systems, the gain medium of the DPAL converts pump energy to lasing energy. The optical energy is provided by laser diodes tuned to the alkali transition wavelength. Lasing then occurs by the transition of alkali atoms from an excited state to a ground state through the emission of photons. The overall structure of this interaction between energy states for rubidium is pictured in figure 2. The picture illustrates the cycle followed by DPAL systems starting with a pump from $^2S_{1/2} \rightarrow {}^2P_{3/2}$ using an optical diode pump. The pump is then followed by a rapid collisional spin orbit relaxation, from $^2P_{3/2} \rightarrow {}^2P_{1/2}$, driven by collisions between atoms of the buffer gas and the alkali gas. The final transition consists of the lasing transition from $^2P_{1/2} \rightarrow {}^2S_{1/2}$, resulting in a photon. A further discussion of transitions, specifically the rates associated with those transitions are presented in chapter IV.

The other major component of a DPAL system is the laser resonator. For a typical DPAL system, the resonator consists two facing mirrors on an optical axis parallel to the lasing direction. Due to the large gain per unit length associated with DPAL and the intended strategic use of a DPAL system, the focus of this dissertation research will be on unstable resonators versus the stable resonator used within many

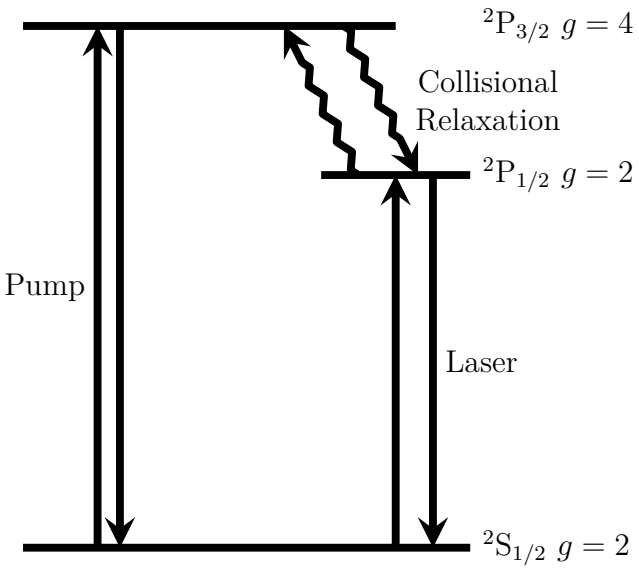

Figure 2. Three-level energy diagram for rubidium lasing interaction.

other laser systems. Stability in regard to a laser cavity references the tendency of photons to remain within the cavity per pass through the gain medium. Unstable resonators are made to allow photons to exit the cavity quickly and have good mode discrimination making them ideal for high gain media.

The Laser Resonator

In prior work concerning analysis of the DPAL, the focus of the work has not involved high powered wave-optic calculations. Hager[10, 11] assumed uniform intra-cavity intensities for the pump and laser. In his papers, he analyzed the steady-state gain and laser power out for narrowband[10] and broadband[11] optical pumps. Additional work concerning low power and a laser cavity mode has also been looked at by Endo in a series of wave optic simulations starting with his discussion of broadband wave optic simulation [12], followed by a further discussion of his wave optics code in unstable resonators[13], a discussion on transverse input pump shape[14], and a final paper that analyzed basic fluid effects on the beam quality for cesium DPAL[15].

Within these simulations, Endo used a gain wave-optic simulation to calculate the beam shape in an unstable resonator. However, Endo kept his simulations confined to the low power input/output scenarios.

Further work in modeling DPAL has also been completed by Barmashenko and Han[16, 17, 18, 19, 20, 21, 22] in modeling the thermal effects caused by the collisionaly mixing in an alkali. These simulations have dealt with both static and dynamic fluids within the cavity. Throughout the various studies, significant temperature gradients were observed for the static cases. These temperature gradients lead to the presence of significant phase variations within the beam of the laser. The dynamic cases focusing on fluid flow indicate that by flowing the fluid at a velocity greater then $5\,\frac{\mathrm{m}}{\mathrm{s}}$, the temperature gradients found in the static case may be mitigated[16].

Further work has been performed by Gavrielides[23] on analyzing unstable resonators with the inclusion of gain. However, for the previous work assumed a gain medium with a homogeneous effect on the laser along the axis of propagation. This research seeks to expand the understanding of the above models with a focus on relating the intracavity mode intensity of an an unstable resonator with both efficiency and beam quality. In order to accomplish this goal, an analysis of the methods typically used in determining the laser modes for bare cavities stable resonators was performed to analyze the strengths and weaknesses of said models. In addition, two unstable resonator cavities from the literature were chosen to further verify the models followed by an analysis of the losses for a positive branch confocal unstable resonator. The results of these bare cavity studies are addressed in chapter III. After the bare cavity models were analyzed, a gain medium was included to the wave-optics simulations in chapter IV. The gain wave-optics simulations were simplified with the use of a uniform pump for excitation of the laser medium. This choice was to simplify the problem in order to better find the underlying effects of coupling between the gain

medium and the transverse laser mode. Amplified Spontaneous Emission (ASE) was also ignored for all simulations to also keep the models simple. After establishing a baseline case, four different studies were performed involving varying Fresnel number, laser gain medium parameters, gain cell position and gain cell length. These four studies determined the effects of the intracavity transverse mode distribution on the laser cavity's output efficiency and beam quality.

II. Basic Theory

Paraxial Propagation

In order to properly model the unstable resonator, two numeric methods will be used for determining bare cavity modes for laser resonators. From these methods, a single method will be chosen to determine the steady-state laser intensity distribution throughout the cavity when gain is present within the system. The next few subsections will be used to derive the Helmholtz wave equation, the Green's Function associated with the Helmholtz Wave equation, the paraxial wave equation and finally the integral form of the paraxial wave equation. The reason for this derivation is that all methods that will be used in the discussion of the field within a bare cavity are essentiatlly different discretization schemes associated with the paraxial wave equation's integral form. Throughout the derivation it will be assumed that $\hat{z}$ is the direction of propagation.

Deriving the Helmholtz Wave Equation .

The wave equations for light propagation start with Maxwell's equations:

$$\boldsymbol{\nabla} \cdot \vec{\mathbf{E}} = \frac{\rho}{\epsilon} \tag{2}$$

$$\boldsymbol{\nabla} \cdot \vec{\mathbf{B}} = 0 \tag{3}$$

$$\boldsymbol{\nabla} \times \vec{\mathbf{E}} = -\frac{\partial \vec{\mathbf{B}}}{\partial t} \tag{4}$$

$$\boldsymbol{\nabla} \times \vec{\mathbf{B}} = \mu \vec{\mathbf{J}} + \mu\epsilon \frac{\partial \vec{\mathbf{E}}}{\partial t} \tag{5}$$

where $\vec{\mathbf{E}}$ and $\vec{\mathbf{B}}$ are vectors representing the electric and magnetic fields, ρ is a charge density and $\vec{\mathbf{J}}$ is the current density, ϵ and μ are the permittivity and permeability of the surrounding medium.

Applying the vacuum case, $\epsilon = \epsilon_0$, $\mu = \mu_0$, $\rho = 0$, and $\vec{\mathbf{J}} = 0$, allows rewriting equations (2), (3), (4), and (5) to

$$\boldsymbol{\nabla} \cdot \vec{\mathbf{E}} = 0\,, \tag{6}$$

$$\boldsymbol{\nabla} \cdot \vec{\mathbf{B}} = 0\,, \tag{7}$$

$$\boldsymbol{\nabla} \times \vec{\mathbf{E}} = -\frac{\partial \vec{\mathbf{B}}}{\partial t}\,, \tag{8}$$

$$\boldsymbol{\nabla} \times \vec{\mathbf{B}} = \mu_0 \epsilon_0 \frac{\partial \vec{\mathbf{E}}}{\partial t}\,. \tag{9}$$

Applying an additional curl to both sides of equations (8) and (9) gives

$$\boldsymbol{\nabla} \times \Big(\boldsymbol{\nabla} \times \vec{\mathbf{E}}\Big) = -\boldsymbol{\nabla} \times \frac{\partial \vec{\mathbf{B}}}{\partial t}\,, \tag{10}$$

$$\boldsymbol{\nabla} \times \Big(\boldsymbol{\nabla} \times \vec{\mathbf{B}}\Big) = \mu_0 \epsilon_0 \boldsymbol{\nabla} \times \frac{\partial \vec{\mathbf{E}}}{\partial t}\,. \tag{11}$$

Using the double curl vector identity for a general vector $\vec{\mathbf{A}}$,

$$\boldsymbol{\nabla} \times \Big(\boldsymbol{\nabla} \times \vec{\mathbf{A}}\Big) = \boldsymbol{\nabla}\Big(\boldsymbol{\nabla} \cdot \vec{\mathbf{A}}\Big) - \nabla^2 \vec{\mathbf{A}}\,, \tag{12}$$

equations (10) and (11) become

$$\boldsymbol{\nabla}\Big(\boldsymbol{\nabla} \cdot \vec{\mathbf{E}}\Big) - \nabla^2 \vec{\mathbf{E}} = -\frac{\partial\Big(\boldsymbol{\nabla} \times \vec{\mathbf{B}}\Big)}{\partial t}\,, \tag{13}$$

$$\boldsymbol{\nabla}\Big(\boldsymbol{\nabla} \cdot \vec{\mathbf{B}}\Big) - \nabla^2 \vec{\mathbf{B}} = \mu_0 \epsilon_0 \frac{\partial\Big(\boldsymbol{\nabla} \times \vec{\mathbf{E}}\Big)}{\partial t}\,. \tag{14}$$

Equations (6) and (7) may be used within (13) and (14) above to deduce the wave equations for the electric and magnetic fields in free space

$$\nabla^2\vec{\mathbf{E}} = \mu_0\epsilon_0\frac{\partial^2\vec{\mathbf{E}}}{\partial t^2}\,, \tag{15}$$

$$\nabla^2\vec{\mathbf{B}} = \mu_0\epsilon_0\frac{\partial^2\vec{\mathbf{B}}}{\partial t^2}\,, \tag{16}$$

where one can recognize $\mu_0\epsilon_0 = \frac{1}{c^2}$ with c representing the speed of light in a vacuum. Since equations (15) and (16) have the same structure, solutions to both wave equations will be identical in free space and may be calculated from a general wave equation where $\vec{\mathbf{E}}$ and $\vec{\mathbf{B}}$ are represented as $\vec{\mathbf{\Psi}}$ combining (15) and (16) into

$$\nabla^2\vec{\mathbf{\Psi}} - \frac{1}{c^2}\frac{\partial^2\vec{\mathbf{\Psi}}}{\partial t^2} = 0\,. \tag{17}$$

Equation (17) may be broken into temporal and spatial parts using separation of variables,

$$\vec{\mathbf{\Psi}}(x,y,z,t) = \vec{\psi}(x,y,z)\vec{\phi}(t)\,. \tag{18}$$

The use of this technique allows for the separation of the time-dependent component of Ψ, ϕ from the spatial-dependent component, $\vec{\psi}$. The splitting allows equation (17) to be written as

$$\frac{1}{\vec{\psi}}\nabla^2\vec{\psi} = \frac{1}{c^2\vec{\phi}}\frac{\partial^2\vec{\phi}}{\partial t^2}\,. \tag{19}$$

In order for equation (19) to be true across independent variables, both sides of the equation must be equal to a constant, allowing equation (19) to be broken into a system of equations, one a Partial Differential Equation (PDE) and the other an

Ordinary Differential Equation (ODE)

$$\frac{1}{\vec{\psi}}\nabla^2\vec{\psi} = -k^2\,, \tag{20}$$

$$\frac{1}{c^2\vec{\phi}}\frac{\partial^2\vec{\phi}}{\partial t^2} = -k^2\,. \tag{21}$$

Equation (21) has the solution

$$\vec{\phi} = \vec{\phi}_0 e^{i(\omega t+\delta)}\,. \tag{22}$$

Equation (22) represents the general solution of time where the solution gives insight in the link between the temporal, ω, and spatial, k frequencies of the wave in free space

$$\frac{\omega}{c} = k\,. \tag{23}$$

Also identified are the temporal phase shift (δ) and the amplitude $\vec{\phi}_0$, making equation (22) a general solution to equation (21). Equation (20), may be written as the PDE

$$\nabla^2\vec{\psi}(\vec{\mathbf{r}}) + k^2\vec{\psi}(\vec{\mathbf{r}}) = 0\,, \tag{24}$$

which is known as the Helmholtz wave equation.

Developing the Paraxial Wave Equation.

The spatial wave function, $\psi(x,y,z)$, in equation (24) may be factored into two parts, one involving the field variation due to the optical frequency dependence of the field and an envelope function, $U(x,y,z)$[24]

$$\psi(x,y,z) = U(x,y,z)e^{ikz}\,. \tag{25}$$

Using equation (25) allows for rewriting equation (24) as

$$\nabla_T^2 U + \frac{\partial^2 U}{\partial z^2} + 2ik\frac{\partial U}{\partial z} = 0\,. \tag{26}$$

In the case of a laser beam, it is important to recognize that the fields associated with the wave equation are highly collimated. Collimation implies very little spherical nature to the wave and that the field will go to zero of the axis of propagation. A consequence of the lack of spherical nature to the wave means that the envelope function, U, identified in equation (25) varies slowly as a function of z. Mathematically, the slow variation of U is known as the paraxial approximation or

$$\left|\frac{\partial^2 U}{\partial z^2}\right| \ll ik\left|\frac{\partial U}{\partial z}\right|. \tag{27}$$

The paraxial approximation allows for the Helmholtz wave equation of U to be simplified to

$$\nabla_T^2 U + 2ik\frac{\partial U}{\partial z} = 0\,, \tag{28}$$

which is known as the paraxial wave equation. The PDE is parabolic and will depend on boundary conditions in the transverse direction and an initial condition representing the field[25]. Solving equation (28) gives the solution for the envelope function of the field and the intensity distribution and phase of the envelope function is the same as that of the field,

$$\psi^\star\psi = U^\star U\,. \tag{29}$$

Equation (29) indicates that once the field envelope function is solved, the volumetric mode of intensity of the field shall be the same.

Converting the Paraxial Wave Equation to Integral Form.

A Laplace Transform applied in the $\hat{z}$ axis allows for a simplification of the three variable PDE (28),

$$\mathscr{L}_z\left[\nabla_T^2 U\right] + 2ik\mathscr{L}_z\left[\frac{\partial U}{\partial z}\right] = 0\,, \tag{30}$$

by making use of the Laplacian identity of the partial derivative in respect to z,

$$\mathscr{L}_z\left[\frac{\partial U}{\partial z}\right] = -U(x,y,0) + s\mathscr{L}_z[U]\,,$$

equation (30) is then reduced to a two variable partial differential equation

$$\nabla_T^2\mathscr{L}_z[U] + 2iks\mathscr{L}_z[U] = 2ikU_0\,, \tag{31}$$

where the source term $U(x,y,0) = U_0$. The application of a Laplace transform has allowed a PDE of three partial derivatives of x, y, and z to be reduced to a PDE of two partial derivatives. The overall structure of equation (28) remains the same in Laplace transform space, but now contains a source term based upon the wave equation at location z_0. The paraxial wave equation's integral form will provide the wave equation at a distance along the axis, z, based upon the value of the wave equation at an initial location, z_0.

Applying a two-dimensional Fourier Transform in x and y allows for Equation (31) to be rewritten as

$$\mathscr{F}_{x,y}\left[\nabla_T^2\mathscr{L}_z[U]\right] + 2iks\mathscr{F}_{x,y}[\mathscr{L}_z[U]] = 2ik\mathscr{F}_{x,y}[U_0]\,, \tag{32}$$

and simplified using the Fourier Transform identity

$$\mathscr{F}_{x,y}\left[\nabla_T^2\mathscr{L}_z[U]\right] = \left(k_x^2 + k_y^2\right)\mathscr{F}_{x,y}[\mathscr{L}_z[U]]\,, \tag{33}$$

to an algebraic function

$$\mathscr{F}_{x,y}[\mathscr{L}_z[U]] = \frac{2ik}{2iks - k_x^2 - k_y^2}\mathscr{F}_{x,y}[U_0]\,. \tag{34}$$

The traditional cost of replacing the "analytic" computation of equation (28) is recaptured in the "analytic difficulty" of applying the inverse Fourier Transform to equation (34) shown in

$$\mathscr{L}_z[U] = \mathscr{F}_{x,y}^{-1}\left[\frac{2ik}{2iks - k_x^2 - k_y^2}\mathscr{F}_{x,y}[U_0]\right]. \tag{35}$$

Writing out the Fourier transform and the inverse Fourier transforms give

$$\mathscr{L}_z[U] = \frac{1}{2\pi}\iint_{-\infty}^{\infty}\frac{2ike^{i(k_x x + k_y y)}}{2iks - k_x^2 - k_y^2}\left[\frac{1}{2\pi}\iint_{-\infty}^{\infty}U(x',y',z)e^{-i(k_x x' + k_y y')}\,\mathrm{d}x'\,\mathrm{d}y'\right]\mathrm{d}k_x\,\mathrm{d}k_y\ , \tag{36}$$

for which coordinates x and y at the source coordinates have been relabeled as x' and y'. k_x and k_y have also been identified as the angular spatial frequencies. k_x and k_y are not dependent on x' and y' allowing one to rewrite the order of the two integrals in equation (36) to

$$\mathscr{L}_z[U] = \frac{1}{4\pi^2}\iint_{-\infty}^{\infty}U(x',y',z)\left[\iint_{-\infty}^{\infty}\frac{2ik}{2iks - k_x^2 - k_y^2}e^{i[k_x(x-x') + k_y(y-y')]}\,\mathrm{d}k_x\,\mathrm{d}k_y\right]\mathrm{d}x'\,\mathrm{d}y'\ . \tag{37}$$

The inner integration in equation (37) is a Green's function in Laplace Transform space and should be solved prior to solving equation (37). The Green's Function,

$G(\vec{\mathbf{x}}, \vec{\mathbf{x}}', s)$, for the integration in equation (37) is

$$G(\vec{\mathbf{x}}, \vec{\mathbf{x}}', s) = \frac{1}{4\pi^2} \iint_{-\infty}^{\infty} \frac{2ik}{2iks - k_x^2 - k_y^2} e^{i[k_x(x-x') + k_y(y-y')]} \, \mathrm{d}k_x \, \mathrm{d}k_y \ , \tag{38}$$

and using a change of coordinates:

$$\begin{gathered} k_x = \eta \cos(\xi) r_x = (x - x') = r \cos(\theta) \\ k_y = \eta \sin(\xi) r_y = (y - y') = r \sin(\theta) \\ \Downarrow \\ k_x^2 + k_y^2 = \eta^2 \, \mathrm{d}k_x \, \mathrm{d}k_y = \eta \, \mathrm{d}\eta \, \mathrm{d}\xi \end{gathered} \tag{39}$$

simplifies equation (38) to

$$G(r, \theta, s) = \frac{1}{4\pi^2} \int_0^{\infty} \int_0^{2\pi} \frac{2ik}{2iks - \eta^2} e^{ir\eta[\cos(\xi)\cos(\theta) + \sin(\xi)\sin(\theta)]} \eta \, \mathrm{d}\xi \, \mathrm{d}\eta \ . \tag{40}$$

Using a trigonometric identity, equation (40) becomes

$$G(r, \theta, s) = \frac{1}{4\pi^2} \int_0^{\infty} \int_0^{2\pi} \frac{2ik}{2iks - \eta^2} e^{ir\eta\cos(\xi - \theta)} \eta \, \mathrm{d}\xi \, \mathrm{d}\eta \ , \tag{41}$$

and the identity associated with the Bessel function

$$J_n(x) = \frac{1}{2\pi} \int_0^{2\pi} e^{ix\eta\cos(\xi - \theta)} \, \mathrm{d}\xi \ , \tag{42}$$

allows the Green's function to be rewritten as

$$G(r, \theta, s) = \frac{1}{2\pi} \int_0^{\infty} \frac{2ik}{2iks - \eta^2} J_0(\eta r) \eta \, \mathrm{d}\eta \ . \tag{43}$$

Equation (43) may be rewritten using the Bessel function identity,

$$\begin{aligned} J_0(\eta r) &= \frac{1}{2}\left[H_0^1(\eta r) + H_0^2(\eta r)\right], \\ H_0^2(-\eta r) &= -H_0^1(\eta r), \end{aligned} \tag{44}$$

into an integral equation with limits of integration from $-\infty$ to ∞

$$G(r,\theta,s) = \frac{1}{2\pi}\int_{-\infty}^{\infty} \frac{ik\eta}{2iks - \eta^2} H_0^1(\eta r)\,\mathrm{d}\eta\ , \tag{45}$$

which allows for the solution to be computed with Cauchy's residue theorem and fractional decomposition. The Green's function of equation (37) is therefore

$$G(r,\theta,s) = \frac{kH_0^1\left(\sqrt{ks}(1+i)r\right)}{2}\,. \tag{46}$$

Placing equation (46) into equation (37) gives the integral form of equation (28) in Laplace transform space,

$$\mathscr{L}_z[U] = \iint_{-\infty}^{\infty} U(x',y',z)\frac{kH_0^1\left(\sqrt{ks}(1+i)r\right)}{2}\,\mathrm{d}x'\,\mathrm{d}y'\ . \tag{47}$$

Equation (47) is also the solution to the paraxial wave equation in response to a source at z. However, the solution would be much more useful if converted from Laplace transform space into coordinate space. The conversion may be performed either with the inverse Laplace Transform (Bromwich Integral) on the right hand side,

$$U(x,y,z+\Delta z) = \frac{k}{2}\iint_{-\infty}^{\infty} U(x',y',z)\mathscr{L}_z^{-1}\left[H_0^1\left(\sqrt{ks}(1+i)r\right)\right]\mathrm{d}x'\,\mathrm{d}y'\ , \tag{48}$$

or by recognizing that the Laplace transform,

$$\mathscr{L}_z\left[-\frac{ik}{2\pi\Delta z}e^{\frac{ikr^2}{2\Delta z}}\right] = -\frac{ik}{\pi}K_0\left[\sqrt{ks}r(1-i)r\right], \tag{49}$$

and the identity

$$K_0(z) = \frac{i\pi}{2}H_0^1(i\Delta z), \tag{50}$$

may be used together to rewrite the inverse Laplace Transform term in equation (48) to be

$$U(x,y,z+\Delta z) = \frac{ik}{2\pi\Delta z}\iint_{-\infty}^{\infty} U(x',y',0)e^{\frac{ik\left[(x-x')^2+(y-y')^2\right]}{2\Delta z}}\,\mathrm{d}x'\,\mathrm{d}y'\ , \tag{51}$$

which is the integral form for the envelope function associated with the field.

Using the definition of the envelope function in equation (25), equation (51) may be rewritten to calculate the field of an initial intensity distribution at point z at an axial distance Δz as

$$\psi(x,y,z+\Delta z) = \frac{ike^{ik\Delta z}}{2\pi\Delta z}\iint_{-\infty}^{\infty} \psi(x',y',z)e^{\frac{ik\left[(x-x')^2+(y-y')^2\right]}{2\Delta z}}\,\mathrm{d}x'\,\mathrm{d}y'\ . \tag{52}$$

Equation (52) is the Huygen's integral calculated for the paraxial approximation, also known as the Fresnel diffraction integral[24]. As stated previously, because of the equivalence in the phase and intensity of the envelope function and field, equation (51) will be used as the primary method to propagate the field along the $\hat{z}$ axis.

Steady-State Bare Cavity

The Fresnel diffraction integral shown in equation (52) propagates the field in the $\hat{z}$ direction. In operator notation equation (51) would act as an operator propagating

the field for a certain length, Δz, and is written as

$$\mathscr{P}_{x,y}[U(x',y')] = -\frac{ik}{2\pi\Delta z}\int_{-\infty}^{\infty}\int_{-\infty}^{\infty} e^{\frac{ik}{2\Delta z}\left[(x-x')^2+(y-y')^2\right]}U(x',y')\,\mathrm{d}x'\,\mathrm{d}y' \ . \tag{53}$$

Any simulation techniques of the beam traversing the laser cavity involve the application of this propagation operator. The form of the above operator shall be modified for the different simulation techniques to take advantage of various properties of the simulation methods. However, the propagation operation is only a part of the calculation, the full propagation of the laser also involves the use of a reflection operator

$$\mathscr{R}_i[U(x,y)] = H(x,y)e^{i\frac{k}{2\pi}\Delta_R(x,y)}U(x,y)\,, \tag{54}$$

where $\Delta_R(x,y)$ is the off axis geometric difference from the position of the mirror and mirror curvature and $H(x,y)$ is a function representing the apodization caused by the finite extent of the mirror. For a spherical mirror, the additional phase shift applied transversely to the field is the function

$$\Delta_{R_i}(x,y) = \mathrm{sgn}(R_i)\left(|R_i| - \sqrt{R_i^2 - x^2 - y^2}\right), \tag{55}$$

allowing equation (54) to be written for spherical mirrors as

$$\mathscr{R}_i[U(x,y)] = H(x,y)e^{i\frac{k}{2\pi}\mathrm{sgn}(R_i)\left(|R_i|-\sqrt{R_i^2-x^2-y^2}\right)}U(x,y)\,. \tag{56}$$

If the distance from the axis is small compared the the curvature of the mirror,

$$|R_i| - \sqrt{R_i^2 - x^2 - y^2} \approx \frac{x^2+y^2}{2R_i}\,, \tag{57}$$

the reflection operator may then be approximated with

$$\mathscr{R}_i[U(x,y)] = H(x,y)e^{i\mathrm{sgn}(R_i)\frac{k\left(x^2+y^2\right)}{4\pi R_i}}U(x,y)\,. \tag{58}$$

The propagation of a laser through a resonator is shown in figure 3. The steps for the transverse laser field traveling through the cavity involve an initial application of the effects of mirror 1, propagation of the distance, Δz, from mirror 1 to mirror 2, the application of mirror 2 effects and the return propagation from mirror 2 to mirror 1. The complete propagation acts to transform the the envelope function, $U(x,y)$, to a final new envelope function, $U'(x,y)$. When represented mathematically the full transformation is

$$U'(x,y) = \mathscr{P}\mathscr{R}_2\mathscr{P}\mathscr{R}_1U(x,y)\,. \tag{59}$$

Originally, Fox and Li[26] recognized that the steady field will have a steady volumetric profile within the lasing cavity. The only difference will be a complex scalar, γ_{Mode}, applied for each transit in the cavity. A transverse field intensity which displays a steady volumetric profile is defined as a transverse cavity mode of the laser resonator[24]. If the initial envelope of the transverse field, U, represents a cavity mode then equation (59), becomes

$$U'_{\mathrm{Mode}} = \gamma_{\mathrm{Mode}}U_{\mathrm{Mode}}\,. \tag{60}$$

Fox and Li, in the same paper, also recognized that the loss associated with a mode of the cavity, α_{loss} will be

$$\alpha_{\mathrm{loss}} = 1 - |\gamma_{\mathrm{Mode}}|\,, \tag{61}$$

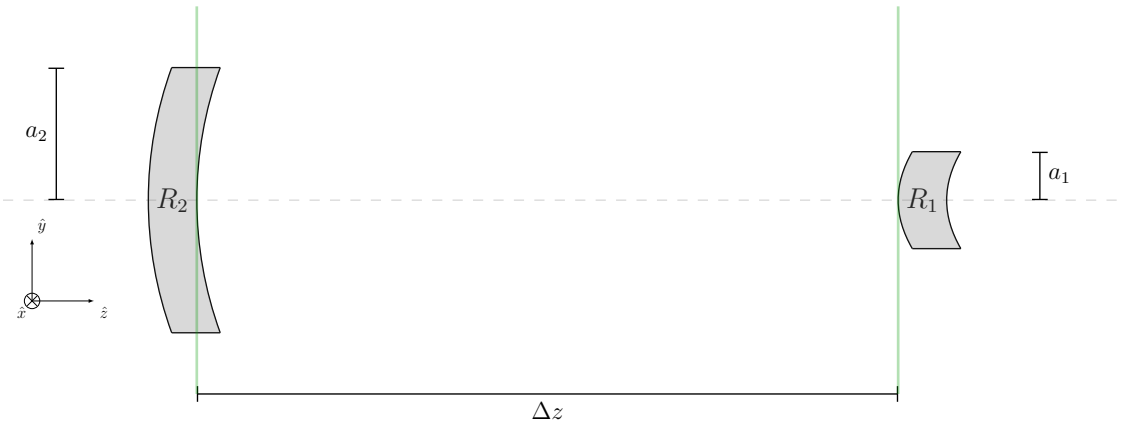

Figure 3. An example picture of the unstable resonator illustrating the setup of the cavity geometry for the rest of the document. R_1 and R_2 are the radii of curvature of the mirrors, a_1 and a_2 are the respective radii of the circular mirrors, and Δz is the separation beween the mirrors.

and the phase shift experienced by a mode for each pass in the resonator, ϕ_{shift} is

$$\phi_{\text{shift}} = \text{angle}(\gamma_{\text{Mode}})\,, \tag{62}$$

where the angle operator calculates the phase of the complex eigenvalue. The ϕ_{shift} may be used with the longitudinal mode[27] of the laser to calculate the frequency of the cavity mode

$$\nu = \left(\frac{c}{2\Delta z}\right)\left[q + \left(\frac{\phi_{\text{shift}}}{2\pi}\right)\right]. \tag{63}$$

The definition of the transverse mode of a laser resonator presented in this section will be continually used throughout the research presented in this document. The definition applies for both bare cavity cases and in cases where a gain medium is added to the bare cavity.

Determining Cavity Modes with the Direct Eigenvector Method (DEM)

In his Prony method paper, Siegman[27] also recognized that the operations in equation (59) could be considered matrix operations and that the modes of the cavity

and the complex scalar in equation (60) multiple were the respective eigenmodes and eigenvalues of the matrix. Siegman then simplified the problem with cylindrical azimuthal symmetry, allowing for the Fresnel integral to be written as a function of a single coordinate, determined by choosing a particular azimuthal mode. However, as will be seen in a future section, to make such a simplification, the back mirror has to be treated as having infinite mirror extents.

More recently, Yuanying [28] recognized that modern computers possessed enough processing power to directly evaluate the complete operation defined in equation (59) for two dimensions. Numerically, the propagation from mirror 1 to mirror 2 is,

$$\vec{\mathbf{U}}_m = \mathbf{A}_{m,n}\vec{\mathbf{U}}_n \,, \tag{64}$$

where $\vec{\mathbf{U}}$ is a one dimensional vector quantity representing the transverse field with n representing the components of the field at mirror 1 and m are the components at mirror 2. $\mathbf{A}_{m,n}$ is then a matrix defined by

$$\mathbf{A}_{m,n} = \mathscr{R}_{\frac{1}{2},2}\mathscr{P}_{m,n}\mathscr{R}_{\frac{1}{2},1}. \tag{65}$$

Likewise, the return propagation is defined by

$$\vec{\mathbf{U}}_n = \mathbf{A}_{n,m}\vec{\mathbf{U}}_m \,, \tag{66}$$

where

$$\mathbf{A}_{n,m} = \mathscr{R}_{\frac{1}{2},1}\mathscr{P}_{n,m}\mathscr{R}_{\frac{1}{2},2} \,. \tag{67}$$

The complete propagation is defined as

$$\mathbf{A}_{\text{Full Pass}} = \mathbf{A}_{n,m}\mathbf{A}_{m,n} \,, \tag{68}$$

where $\mathbf{A}_{\text{Full Pass}}$ is a $n \times n$ matrix representing the full propagation of the transverse envelope function through the cavity. As stated above, the final cavity output field, $\vec{\mathbf{U}}_1'$, is defined by the input field, $\vec{\mathbf{U}}_1$ at mirror 1 is the operation

$$\vec{\mathbf{U}}_1' = \mathbf{A}_{\text{Full Pass}} \vec{\mathbf{U}}_1 \,. \tag{69}$$

In practice, the input and output vectors are treated as abstract concepts and are only used for determining the elements of $\mathbf{A}_{\text{Full Pass}}$. As stated previously, the different eigenvalues of $\mathbf{A}_{\text{Full Pass}}$ are the complex scalars defined by Fox and Li in equation (60), and the eigenvectors of $\mathbf{A}_{\text{Full Pass}}$ are the cavity modes.

For bare-cavity calculations, DEM can determine cavity modes with a single iteration. Unlike typical Fox and Li iterator methods that shall be covered in the next sections, DEM offers the potential to solve every cavity mode present within the bare cavity along with their respective losses and phase shift per pass in a single iteration. However, the method, while very effective in determining every mode of an unstable resonator tends to be computationally intense. For example, two two-dimensional mirrors sampled 20 times along each coordinate, require two grids of 400 elements each leading to $\mathbf{A}_{\text{Full Pass}}$ containing over 160000 complex values. If sampling along each coordinate is quadrupled to have 80 elements, there will be over 40 million complex values. Therefore, The scaling of the problem goes as $\mathcal{O}(N^4)$, where N is the sampling along each coordinate represents a computational difficulty in using DEM to calculate scenarios requiring high grid resolution.

Discretizing the Propagation.

Using DEM requires the scheme presented for the matrix computation to be properly discretized. The propagation operation representing the propagation from a grid,

n, m to grid p, q becomes

$$U^{p,q} = \frac{ik}{2\pi\Delta z^{p,q}_{n,m}} \sum_{n=1,m=1}^{N,M} e^{-\frac{ik}{2\Delta z^{p,q}_{n,m}}\left(\rho^{p,q}_{n,m}\right)^2} r'_{n,m}\mathbf{1}^{p,q}\Delta r'\Delta\theta' U^{n,m}. \tag{70}$$

where the definition

$$\rho^{p,q}_{n,m} = \sqrt{\left(\Delta x^{p,q}_{n,m}\right)^2 + \left(\Delta y^{p,q}_{n,m}\right)^2}\,, \tag{71}$$

was used to simplify equation (70). At this point, one identifies the geometry that will be present within the problems of the simulation. In order to prevent the artifacts associated with imposing a rectangular grid structure on circular mirrors, a cylindrical coordinate system was used for the DEM calculation meaning that Δx Δy, and Δz in equation (71) were defined as

$$\begin{aligned}
\Delta x^{p,q}_{n,m} &= r^{p,q}\mathbf{1}_{n,m}\cos(\theta^{p,q}\mathbf{1}_{n,m}) - r'_{n,m}\mathbf{1}^{p,q}\cos(\theta'_{n,m}\mathbf{1}^{p,q})\,,\\
\Delta y^{p,q}_{n,m} &= r^{p,q}\mathbf{1}_{n,m}\sin(\theta^{p,q}\mathbf{1}_{n,m}) - r'_{n,m}\mathbf{1}^{p,q}\sin(\theta'_{n,m}\mathbf{1}^{p,q})\,,\\
\Delta z^{p,q}_{n,m} &= \Delta z\mathbf{1}^{n,m}_{p,q}\,.
\end{aligned} \tag{72}$$

In actual practice, it is important to define $U^{p,q}$ as covariant vector that is pq in size (the two variables are to remind that there are two coordinates present within the system), $U_{n,m}$ a contravariant vector that is nm in size, and $A^{p,q}_{m,n}$ a rank two tensor with pq columns and nm rows. k is the wavenumber, and $r_{n,m}$ is the transverse vector.

Discretizing Mirror Effects.

Previously in section , the scheme for handling the mirror was derived to get the mirror operator mention in equation (56). The operator may be discretized as

$$\Gamma_{n,m} = e^{-2ik\Delta_{n,m}}\,, \tag{73}$$

with $\Delta_{n,m}$ identified as

$$\Delta_{n,m} = \text{sign}(R_1 \mathbf{1}_{n,m}) \left[|R_1 \mathbf{1}_{n,m}| - \sqrt{R_1^2 \mathbf{1}_{n,m} - (r'_{n,m})^2} \right]. \tag{74}$$

Combined Discretization.

Combining the above discretizations into one complete operation nets a rank two tensor, $A^{p,q}_{n,m}$, which was defined earlier as the matrix corresponding to the half propagation of the field in the system, with

$$A^{p,q}_{m,n} = \frac{ike^{ik\Delta z^{p,q}_{n,m}}}{2\pi \Delta z^{p,q}_{n,m}} \Gamma_{n,m} \mathbf{1}^{p,q} e^{-\frac{ik}{2\Delta z^{p,q}_{n,m}} \left(\rho^{p,q}_{n,m}\right)^2} r'_{n,m} \mathbf{1}^{p,q} \Delta r' \Delta \theta' \,, \tag{75}$$

giving a the representation of the half pass from the initial mirror, with coordinates corresponding to n and m to the second mirror, with coordinates as p and q, of

$$U^{p,q} = A^{p,q}_{n,m} U^{n,m} \,. \tag{76}$$

In order to complete the trip through the cavity, the entire pass may be completed with the propagation from n and m to p and q followed by the corresponding propagation/mirror operation going from p and q back to n and m. Represented in discretized notation the complete trip becomes

$$U^{n,m}_{\text{New}} = A^{n,m}_{p,q} A^{p,q}_{n,m} U^{n,m} \,, \tag{77}$$

where

$$A^{n,m}_{p,q} = \frac{ike^{ik\Delta z^{n,m}_{p,q}}}{2\pi \Delta z^{n,m}_{p,q}} e^{\frac{ik}{2\Delta z^{n,m}_{p,q}} \left(\rho^{m,n}_{p,q}\right)^2} r_{p,q} \mathbf{1}^{n,m} \Gamma_{p,q} \mathbf{1}^{n,m} \delta r \delta \theta \,. \tag{78}$$

and all parameters are defined as

$$\begin{aligned}
\rho_{p,q}^{n,m} &= \sqrt{\left(\Delta x_{p,q}^{n,m}\right)^2 + \left(\Delta y_{p,q}^{n,m}\right)^2} \\
\Gamma_{p,q} &= e^{-2ik\Delta_{p,q}}\,, \\
\Delta_{p,q} &= \mathrm{sign}(R_2\mathbf{1}_{p,q})\left[|R_2\mathbf{1}_{p,q}| - \sqrt{R_2^2\mathbf{1}_{p,q} - (r_{p,q})^2}\right], \\
\Delta x_{p,q}^{n,m} &= r'^{n,m}\mathbf{1}_{p,q}\cos\left(\theta'^{n,m}\mathbf{1}_{p,q}\right) - r_{p,q}\mathbf{1}^{n,m}\cos(\theta_{p,q}\mathbf{1}^{n,m})\,, \\
\Delta y_{p,q}^{n,m} &= r'^{n,m}\mathbf{1}_{p,q}\sin\left(\theta'^{n,m}\mathbf{1}_{p,q}\right) - r_{p,q}\mathbf{1}^{n,m}\sin(\theta_{p,q}\mathbf{1}^{n,m})\,, \\
\Delta z_{p,q}^{n,m} &= \Delta\mathbf{1}_{p,q}^{n,m}\,,
\end{aligned} \tag{79}$$

where δr and $\delta\theta$ are the respective resolutions of the radial and azimuthal coordinates.

The two operations may then be combined with simple matrix multiplication to become

$$A_{\mathrm{Tot}}{}_{n,m}^{n,m} = A_{p,q}^{n,m}A_{n,m}^{p,q}\,. \tag{80}$$

As stated above, this final operation represents the total propagation of the envelope function through the cavity. The eigenvectors of the combined tensor in equation (80) are the modes of the cavity, conveniently in the coordinate basis that was originally used to define $\theta_{m,n}$ and $r_{m,n}$. The eigenvalues of equation (80) represent the scaling of the envelope function for each pass associated with corresponding modes.

Fox and Li Iteration

Although DEM is an excellent method for solving for all cavity modes in a single calculation, the memory requirements for the method can quickly overwhelm modern systems. Fox and Li iterative calculations may be used to solve equation (60) for only the least-loss mode with a decreased computational difficulty. Each laser cavity mode, U_{Mode} experiences different losses per pass through the cavity. Simulating the cavity propagation for an initial "guess" transverse envelope function, U, and

then renormalizing leads to a transverse envelope function with less content that is not associated with the lowest loss cavity mode. Iterating the above process multiple times leaves a transverse envelope function whose form does not change for additional passes. Per the definition of cavity mode, this converged transverse function is the lowest loss cavity mode. The eigenvalue is then the complex scalar renormalization applied to the field. A simulation is considered converged when the transverse field profile remains constant for successive passes. The above procedure has come to be known as Fox and Li iteration, named for it's initial use in Fox and Li's 1961 paper for calculating laser modes in laser resonators possessing mirrors of finite extent[26].

Fox and Li iteration tends to be computationally lighter than DEM, especially because the propagation operation mentioned in equation (53) may be rewritten as single or a series of Fast Fourier Transform (FFT) operations. However, the iterative method may become computational intense for cases where the losses between the first and second lowest loss cavity modes are small. For unstable resonators, the difference in losses between the first and second mode tend to be large for most cavity configurations, leading to convergence within a hundred passes through the cavity. However, the stable resonator, where the losses for various cavity modes have small differences compared to each other, required at least four thousand passes within the cavity.

Another reason to use Fox and Li iteration within the cavity comes from the recognition that the lighter computational load associated with the iteration allows for the eventual addition of gain within the cavity. DEM could be used for such techniques, but the time and memory requirements would be prohibitive compared to the Fox and Li iteration computation cost.

Fox and Li iteration requires all operations defined in equation (59), but the propagation operation may be handled differently to take advantage of different compu-

tational simplifications and to also enable certain grid configurations for the system. Angular Spectrum Method (ASM) and Fresnel Forward Propagator (FFP) are the two propagation methods that were used for this research and are discussed in the next two subsections followed by a subsection discussing some of the constraints of the methods.

The Fresnel Forward Propagator (FFP) .

FFP starts with expanding equation (53),

$$\mathscr{P}_{x,y}[U(x',y')] = -\frac{ik}{2\pi\Delta z} e^{i\frac{k}{2\Delta z}\left[x^2+y^2\right]} \iint_{\infty}^{\infty} U(x',y') e^{i\frac{k}{2\Delta z}\left[x'^2+y'^2\right]} e^{-i\frac{k}{\Delta z}[xx'+yy']}\,\mathrm{d}x'\,\mathrm{d}y' \ . \tag{81}$$

From the expansion, one may recognize the integral is a Fourier Transform

$$\mathscr{F}_{f_{x'},f_{y'}}[f(x',y')] = \iint_{\infty}^{\infty} f(x',y') e^{-i\frac{k}{\Delta z}[xx'+yy']}\,\mathrm{d}x'\,\mathrm{d}y' \ , \tag{82}$$

operating on a function

$$f(x',y') = U(x',y') e^{i\frac{k}{2\Delta z}\left[x'^2+y'^2\right]} . \tag{83}$$

The Fourier Transform moves the field from a coordinate space at x' and y' to the frequency space defined as

$$f_{x'} = \frac{k}{2\Delta z} x \, , \tag{84}$$

$$f_{y'} = \frac{k}{2\Delta z} y \, . \tag{85}$$

As Schmidt[29] recognized, the above frequency definitions require the grid have a certain sampling if the grid resolution between propagation planes is constant. The

grid resolution, δ, is then a function of the sampling, N, the laser angular spatial frequency, k, and the propagation distance, Δz,

$$\delta = \sqrt{\frac{2\pi\Delta_z}{Nk}}\,. \tag{86}$$

From the above definitions, one may rewrite equation (81) into a complete operation

$$\mathscr{P}_{x,y}[U(x',y')] = -\frac{ik}{2\pi\Delta z} e^{i\frac{k}{2\Delta z}\left[x^2+y^2\right]} \mathscr{F}\left[U(x',y') e^{i\frac{k}{2\Delta z}\left(x'^2+y'^2\right)}\right]. \tag{87}$$

The Angular Spectrum Method (ASM) .

Much like FFP in the previous section, ASM starts with rewriting the Fresnel integral defined in equation (53). However, instead of separating terms, the integral may be rewritten as a convolution of the source function, U and the exponential propagation function,

$$\mathscr{P}_{x,y}[U(x',y')] = -\frac{ik}{2\pi} \int_{-\infty}^{\infty} \frac{e^{\frac{ik}{2\Delta z}\left[(x-x')^2+(y-y')^2\right]}}{\Delta z} U(x',y')\,\mathrm{d}x'\,\mathrm{d}y'\ , \tag{88}$$

or more easily seen as

$$\mathscr{P}_{x,y}[U(x',y')] = -\frac{ik}{2\pi}\left[\frac{e^{\frac{ik}{2\Delta z}\left[(x-x')^2+(y-y')^2\right]}}{\Delta z} * U(x',y')\right]. \tag{89}$$

The relationship between convolution and the Fourier Transform[25] may be used to rewrite equation (89)

$$\mathscr{P}_{x,y}[U(x',y')] = \mathscr{F}^{-1}\left[\mathscr{F}\left[\frac{ke^{\frac{ik}{2\Delta z}\left[(x-x')^2+(y-y')^2\right]}}{2i\pi\Delta z}\right]\mathscr{F}[U(x',y')]\right], \tag{90}$$

where the first Fourier Transform is known as the propagator. In order to simplify the calculation, the propagator may then be transformed analytically

$$\mathscr{F}\left[\frac{e^{\frac{ik}{2\Delta z}\left[(x-x')^2+(y-y')^2\right]}}{\Delta z}\right] = e^{\frac{i\Delta z}{2k}\left[k_x^2+k_y^2\right]}, \tag{91}$$

where the angular spatial frequencies, k_x and k_y are used to define frequency space. Equation (90) may then be rewritten with equation (91) to develop the ASM propagation operation

$$\mathscr{P}_{x,y}[U(x',y')] = \mathscr{F}^{-1}\left[e^{\frac{i\Delta z}{2k}\left[k_x^2+k_y^2\right]}\mathscr{F}[U(x',y')]\right]. \tag{92}$$

Unlike FFP, ASM does not place a constraint on sampling versus resolution. However, it does require additional considerations to prevent aliasing within both the spatial coordinate grid and the spatial frequency grid. The next subsection will be dedicated to analyzing the grid requirements for both propagation methods, with an additional focus applied to ASM.

Resolution Requirements.

The overall goal of the research was to understand the effects of varying parameters of unstable resonators, specifically that of the positive branch confocal stable resonator, and understanding the effects of that variation on mode loss and the mode shape. Therefore, in order to use both FFP and ASM for such a calculation, it is important to identify grid constraints for the positive branch confocal resonator much as Schmidt did for the general case [29] using geometric optics.

Minimum Sampling Required by Geometry.

To determine the minimum sampling associated with a problem requires analyzing the propagation of U from an initial plane to a final plane separated by a distance Δz. A picture of this simple propagation is shown in figure 4, giving definitions to Δz, M, a, $f_{x,\max}$, and α.

From the figure, α can be seen to follow the relationship

$$\frac{2(Ma+a)}{2\Delta z} = \tan(\alpha) \approx \alpha \,. \tag{93}$$

The α approximation follows from the paraxial limit used in both propagation schemes. In the spatial frequency coordinate, the relationship between $k_{x,\max}$ and k also has the relationship with α,

$$\frac{k_{x,\max}}{k} = \sin(\alpha) \approx \alpha \,. \tag{94}$$

Based upon requirements of the Nyquist frequency[30], a relationship exists between $k_{x,\max}$ and the minimum spatial coordinate resolution δ_x

$$\frac{1}{2\delta_x} \geq f_{x,\max} \,, \tag{95}$$

$$\frac{\pi}{\delta_x} \geq k_{x,\max} \,, \tag{96}$$

$$\frac{\pi}{k\delta_x} \geq \frac{k_{x,\max}}{k} \,. \tag{97}$$

Combining equations (93) and (94) along with the Nyquist Criteria gives a constraint on the minimum resolution of the optical grid based upon the problem geometry

$$\frac{\pi}{k\delta_x} \geq \frac{2(Ma+a)}{2\Delta z} \,, \tag{98}$$

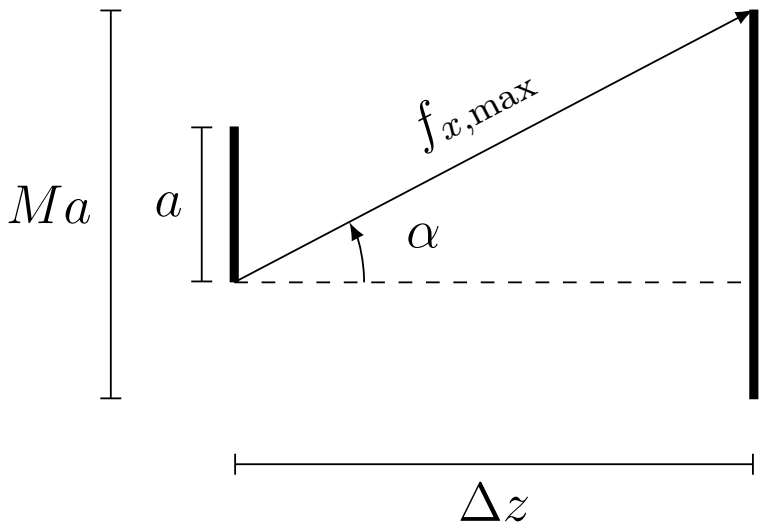

Figure 4. Propagation of U from an initial plane to a final plane, with the extent of the field being assumed to be the size M. Figure has been tailored from an illustration from Schmidt's *Numerical Simulation of Optical Wave Propagation*[29].

which may be rewritten in terms of Fresnel number, N_{f}, and the geometric magnification, M, of the problem

$$\frac{1}{\delta_x} \geq \frac{2(M+1)N_{\mathrm{f}}}{a}\,. \tag{99}$$

For the purposes of large scale simulation, the resolution should be rewritten in terms of the total grid extent. The total grid extent be a function of the size of the largest mirror's radius, Ma defined in figure 4 with the relationship

$$\Delta x = 2G_{\mathrm{Band}}Ma\,, \tag{100}$$

where G_{Band} scales the total grid extent as a function of the size of the large mirror. By multiplying both sides of equation (99) by $2G_{\mathrm{Band}}Ma$

$$\frac{G_{\mathrm{Band}}2Ma}{\delta_x} \geq \frac{4MaG_{\mathrm{Band}}(M+1)N_{\mathrm{f}}}{a}\,, \tag{101}$$

and then recognizing that the sampling, N_x is the ratio of the total grid extent to the grid resolution,

$$N_x = \frac{\Delta x}{\delta_x}\,, \tag{102}$$

equation (99) may be rewritten as

$$N \geq 4G_{\text{Band}}\left(1 + \frac{1}{M}\right)M^2 N_{\text{f}}\,. \tag{103}$$

Equation (103) may then be rewritten as a function of the outer Fresnel number, $N_{\text{f,O}}$, which is the Fresnel number associated with the larger mirror of the cavity and has the relationship

$$N_{\text{f,O}} = M^2 N_{\text{f}}\,, \tag{104}$$

simplifying equation (103) and tying the computational difficulty with the outer Fresnel number,

$$N \geq 4G_{\text{Band}}\left(1 + \frac{1}{M}\right)N_{\text{f,O}}\,. \tag{105}$$

Minimum Sampling Required by Optical Grid.

The above constraint is motivated purely by the cavity geometry. There is also a requirement generated by propagating the field in the optical grid. The propagation through the optical field is shown in figure 5.

From the picture, one may define an extent of illumination, D_{illum}, as a function of radius of the largest plane of optical interaction. The largest plane occurs for the large mirror which has a radius of Ma. The maximum angle for which the field will be transmitted, $\alpha_{\max}$, and the propagation distance, Δz. may then be used to define the extent of illumination

$$D_{\text{Illum}} = 2Ma + 2\alpha_{\max}\Delta z\,. \tag{106}$$

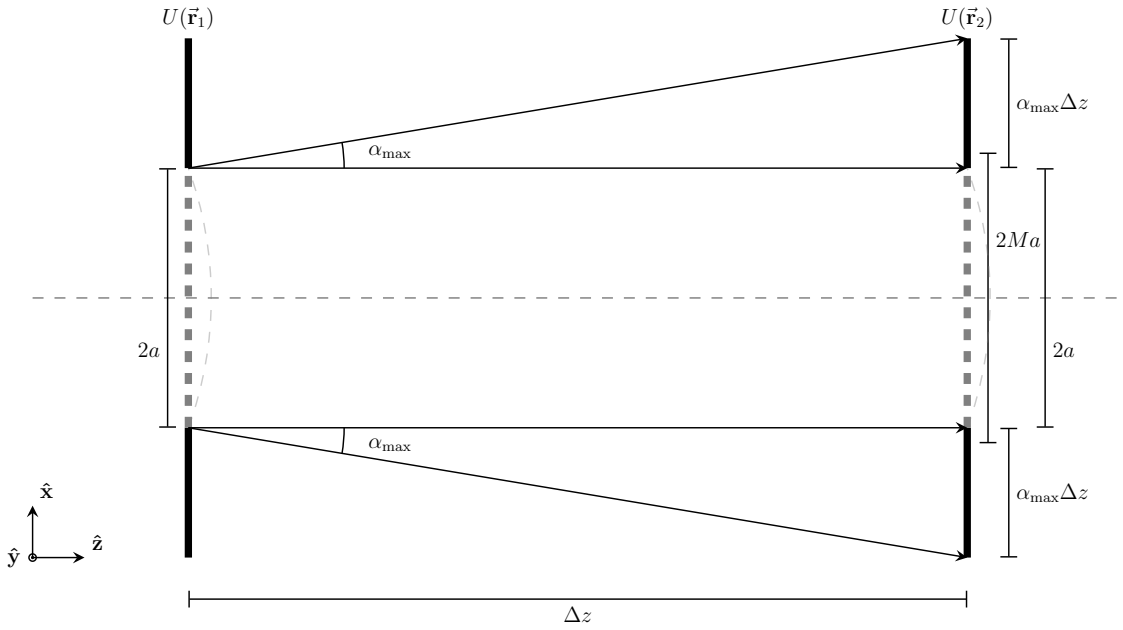

Figure 5. Propagation of the field from an initial to a final plane showing the total grid extents of the final plane as based upon the maximum spread angle, $\alpha_{\max}$. Figure has been tailored from an illustration from Schmidt's *Numerical Simulation of Optical Wave Propagation*[29].

The optical grid's total extent, Δx_{Tot}, must be large enough to support the illuminated image. The usage of a Fourier Transform for the propagation means that as if the field illuminates a larger area than the total grid extent, the image will be wrapped around the other side of the transverse grid. Recognizing this places a constraint on the total grid extent

$$\Delta x_{\text{Tot}} \geq \frac{2Ma + 2a + 2\alpha_{\max}\Delta z}{2} = Ma + a + \alpha_{\max}\Delta z\,. \tag{107}$$

Applying the definition for total grid extent mentioned in equation (100) allows for the constraint to be written as

$$2G_{\text{Band}}Ma \geq a(1+M) + \alpha_{\max}\Delta z\,, \tag{108}$$

where $\alpha_{\max}$ is related to the maximum extent of the frequency grid, Δk_x, and is also related to the resolution of the spatial grid,

$$\Delta k_x = \frac{\pi}{\delta_x} \,. \tag{109}$$

The relations (109), (102) and (100) allow for $\alpha_{\max}$ to be rewritten as,

$$\alpha_{\max} = \frac{N\lambda}{4G_{\text{Band}}Ma} \,. \tag{110}$$

Finally, one may use the constraint for the total optical grid extent to be

$$\Delta x_{\text{Tot}} \geq (1+M)a + \frac{N\lambda\Delta z}{4G_{\text{Band}}Ma} \,, \tag{111}$$

and rewriting Δx_{Tot} as a function of cavity parameters and solving for N, gives the requirement on sampling to be

$$N \leq 2G_{\text{Band}}^2 4N_{\text{f,O}} - \left(1 + \frac{1}{M}\right) 4G_{\text{Band}} N_{\text{f,O}} \,. \tag{112}$$

Constraint (112) is a light constraint which only applies for ASM. FFP already includes the constraint by requiring

$$N = 4G_{\text{Band}}^2 N_{\text{f,O}} \,. \tag{113}$$

Maximum Sampling Required by Problem Geometry.

The variation of phase across the optical grid also places a maximum sampling constraint on the problem[29]. In spatial coordinates, the phase variation is the phase factor imparted on the field by the mirror. According to the mirror operation present

in equation (58), the phase factor, ϕ_{R}, is

$$\phi_{\mathrm{R}} = k\frac{x^2}{2R}\,. \tag{114}$$

Schmidt[29] and Goodman[30] recognize the local frequency space variation, k_{loc} is the gradient of the phase used within the propagator,

$$k_{\mathrm{loc}} = \boldsymbol{\nabla}\phi\,, \tag{115}$$

and applying equation (115) to the phase factor of the mirror gives the local variation of the frequency grid caused by the problem geometry, $k_{\mathrm{loc},x}$,

$$k_{\mathrm{loc},x} = \frac{kx}{R}\,. \tag{116}$$

Applying the Nyquist Criterion to the localized frequency gives the constraint

$$\frac{ka}{R} \leq \frac{\pi}{\delta_x}\,, \tag{117}$$

and applying the relationship between the resolution and the total grid extent gives

$$N \geq \frac{4kG_{\mathrm{Band}}a^2}{2\pi R}\,. \tag{118}$$

Finally, by recognizing that the radii of curvature of positive confocal mirrors is related to the geometric magnification and then applying the definitions in equations equation (178) give,

$$N \geq \frac{4G_{\mathrm{Band}}\left(1-\frac{1}{M}\right)N_{\mathrm{f,O}}}{2}\,. \tag{119}$$

Maximum Sampling Required by Optical Grid.

If the sampling of a simulation is increased without modifying the corresponding optical field extents, problems may occur in frequency space due to a lack of resolution. This requirement requires that the local k value, $k_{\mathrm{loc},k}$, needs to vary less than half the total grid extent, in this case written as $N\delta_x$

$$k_{\mathrm{loc},k} \leq \frac{N\delta_x}{2}. \tag{120}$$

From equation (92), the phase in the propagator is defined as

$$\phi_{\mathrm{k}} = \frac{\Delta z}{2k} k_x^2 \,. \tag{121}$$

Using the definition with equation (121) inside equation (115) allows for equation (120) to be written as

$$\frac{\pi \Delta z}{k \delta_x} \leq \frac{N\delta_x}{2} \,. \tag{122}$$

Applying the previous definition for total grid extents allows for rewriting (122) as

$$N \leq 4 G_{\mathrm{Band}}^2 N_{\mathrm{f,O}} \,. \tag{123}$$

Much as the minimum sampling constraint in equation (112) was identified as a light constraint, equation (123) is also a light constraint that will only apply to ASM, because FFP already induces the hard constraint,

$$N = 4 G_{\mathrm{Band}}^2 N_{\mathrm{f,O}} \,. \tag{124}$$

Using all Constraints.

For large scale simulations, having constraints based on the number of samples makes the computational complexity vary depending on parameter. However, considering the use of Fourier Transforms within the problem means that the best computational performance occurs for simulations which have sampling of $N = 2^l$ where l is a positive integer. Meeting all constraints and keeping a factor of 2 number of samples is difficult. The difficulty in dealing with sampling of multiple problem may be handled by instead recasting the constraints above in terms of the additional spatial extent beyond the optical area, G_{Band}. Rewriting all constraints in terms of G_{Band} gives the final system constraints

$$G_{\text{Band}} \geq \sqrt{\frac{N}{4N_{f,0}}}\,, \tag{125}$$

$$G_{\text{Band}} \geq \frac{1}{4}\left[\left(1+\frac{1}{M}\right)+\sqrt{\left(1+\frac{1}{M}\right)^2+8\left(\frac{N}{4N_{f,0}}\right)}\right], \tag{126}$$

$$G_{\text{Band}} \leq \frac{1}{1+\frac{1}{M}}\left(\frac{N}{4N_{f,0}}\right), \tag{127}$$

$$G_{\text{Band}} \leq \frac{2}{\left(1-\frac{1}{M}\right)}\left(\frac{N}{4N_{f,0}}\right), \tag{128}$$

As indicated in Schmidt[29], propagating multiple times only modifies one equation (125)

$$G_{\text{Band}} \geq \sqrt{R_z}\sqrt{\frac{N}{N_{f,0}}}\,, \tag{129}$$

where R_z is defined as the ratio of the step length, Δz_i compared to the propagation length

$$R_z = \frac{\Delta z_i}{\Delta z}\,. \tag{130}$$

For bare cavity simulations, propagation will only occur once between the mirrors, $R_z = 1$. Figure 6 is an example plot of the constraints in equations (125), (126), (127), and (128) representing a positive branch confocal unstable resonator. The plot treats the lower bound of G_{Band} by using the more restrictive of equations (127) and (128). Likewise, the upper bound of the plot is the most restrictive constraints of (125) and (126) Figure 6 also indicates a value of $\frac{N}{N_{\text{f,O}}}$ below which the equations (125), (126), (127), and (128) may not be true. This cross-over of the upper and lower bounds indicates a minimum value of $\frac{N}{N_{\text{f,O}}}$ required for the simulation. In other words, there is a minimum sampling required for a simulation driven by the laser cavity's outer Fresnel number. Figure 6 also defines an ideal G_{Band}, based on being 10% greater than the lower constraint, which was used for the bare cavity simulations in a bare cavity eigenvalue study at the end of chapter III.

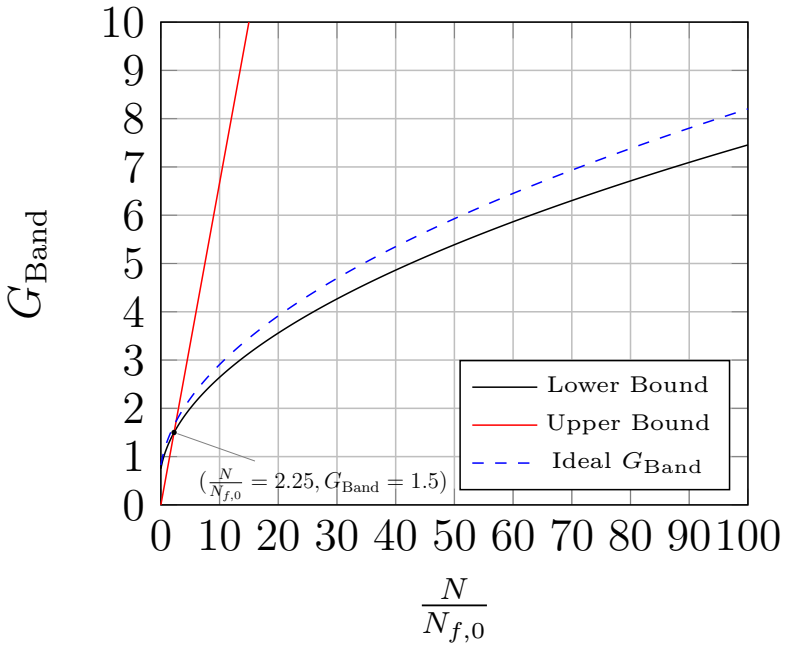

Figure 6. Example requirements on G_{Band} which bookmarks the available band size of the system. The upper band represents the maximum value of G_{Band} and lower band gives a minimum value of G_{Band} required to eliminate aliasing.

III. Simulation of the Bare Cavity Laser Resonator

There is no analytic expression that can completely express the modes of a laser cavity with finite apertures. For the a stable laser resonator, the aperture size is assumed to be infinite in size allowing for the analytic derivation of the modes for a stable laser resonator cavity. Usually this assumption works fairly well and the modes of a stable resonator are well approximated by the analytic solution with an infinite aperture size. Unfortunately the diffraction due to a limited aperture size always effects the modes of an unstable resonator cavity, requiring that the mode always be computed with bare cavity numeric methods. This chapter is dedicated to the analysis of these bare cavity numeric methods, which were previously described in chapter II.

The first section of the chapter is dedicated to a brief discussion of laser resonator stability followed by a section concerning testing of the three methods covered in chapter II, for a stable half-symmetric cavity layout. The testing was performed to compare the numeric method calculations against the stable cavity mode predicte by analytic techniques. Following the comparison of the numeric methods and the stable resonator is a brief discussion of geometric loss expected for unstable resonators. After this discussion of unstable resonator cavities, the methods were again compared with each other and a result Yuanying's[28] results for an unstable resonator calculation. Following the discussion, the general unstable resonator results is a definition followed by a study of a positive branch confocal unstable resonator described in papers by Siegman and Sziklas[31, 32]. The final bare cavity study involved Siegman's eigenvalue method, which is defined and then used to calculate and compare eigenvalue predictions from Siegman's 1970 Prony paper[27], DEM, and Fox and Li Iteration using ASM as a propagator for a variety of positive branch confocal unstable resonators.

The discussion will begin by defining some of the terminology of laser resonators and about stability of those resonators.

What is the Stability of a Laser Resonator?

Previously within the document, the stability of laser resonators has been mentioned as a differentiator between resonators. However, what classifies the difference between a stable and unstable resonator has yet to be mentioned. This section is dedicated to defining laser resonator stability. The qualitative characteristic in differentiating stable and unstable resonators is the repetition of the mode intensity distribution per pass through a laser resonator for mirrors with infinite extent. If the the intensity distribution of the propagating field is reproduced for every pass within the laser resonator, then the system is considered stable, otherwise it is unstable. Further definition requires a geometric analysis of mode propagation in a system similar to that shown in figure 7.

The geometric ray optics starts with a picture of wave propagation much like the one given by Siegman[24], and illustrated in figure 8, where one sees that the relationship between the transverse position of a wave, x, and its change in transverse position, x', are related axially by the operation of an ABCD matrix

$$\begin{pmatrix} x_2 \\ x_2' \end{pmatrix} = \begin{pmatrix} A & B \\ C & D \end{pmatrix} \begin{pmatrix} x_1 \\ x_1' \end{pmatrix}. \tag{131}$$

As shown in figure 8, the ABCD matrix, may be written as a cumulative effect of all operations performed by the field[34]. The combined propagation operations for the field as it passes through the generalized laser resonator system illustrated in figure 7

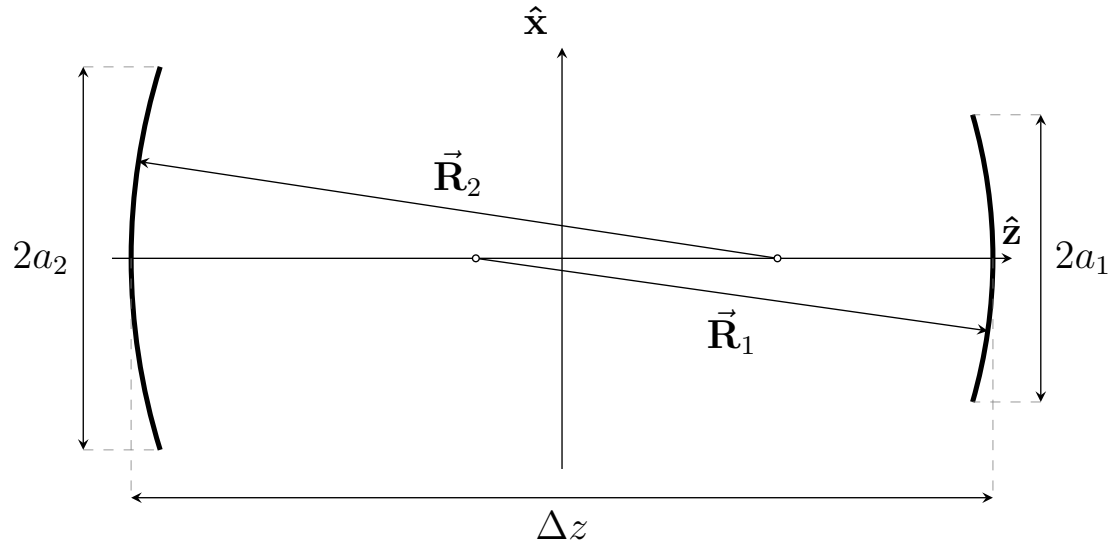

Figure 7. Spherical mirror resonator with respective mirror radii of R_1 and R_2 and width $2a_1$ and $2a_2$ with a mirror spacing of Δz. The illustration is a duplicate with minor changes to symbols of Gordon's picture of a cavity from his paper on the equivalence relations for spherical mirror resonators[33].

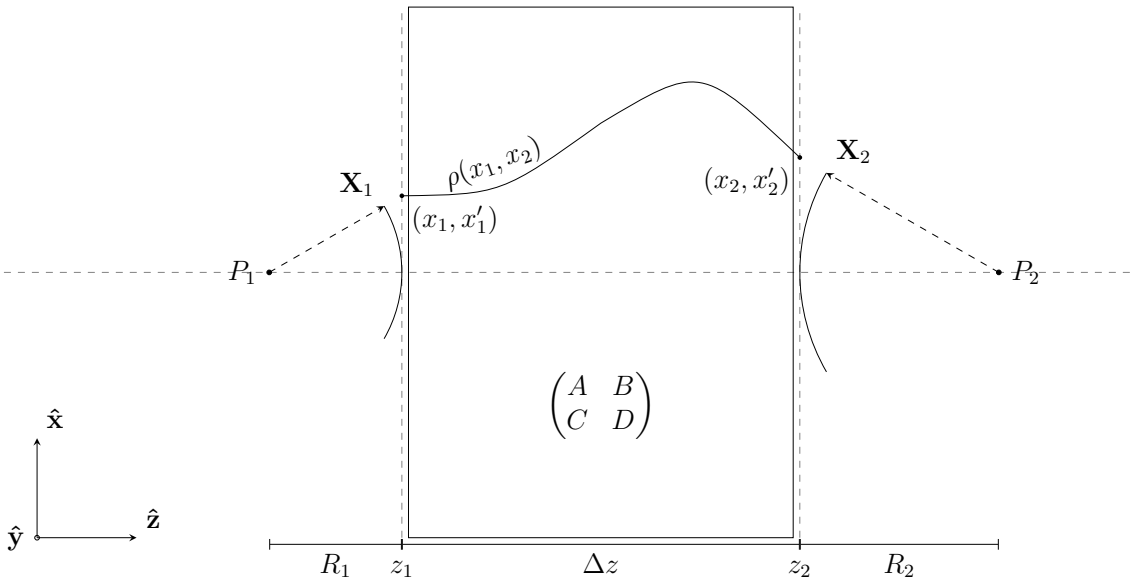

Figure 8. An illustration of the ABCD geometric optical propagation through the cavity. The figure is a rough replication of Siegman's illustration from his textbook, *Lasers*[24], used to discuss a geometric analysis of paraxial wave optics.

is

$$\begin{bmatrix} A & B \\ C & D \end{bmatrix} = \begin{bmatrix} \left(1-\frac{2\Delta z}{R_1 n}\right)\left(1-\frac{2\Delta z}{R_2 n}\right)-\frac{2\Delta z}{R_2 n} & 2\frac{\Delta z}{n}\left(1-\frac{\Delta z}{R_1 n}\right) \\ \frac{4\Delta z}{R_1 R_2 n}-\frac{2}{R_2}-\frac{2}{R_1} & 1-\frac{2\Delta z}{R_1 n} \end{bmatrix}, \tag{132}$$

for which n is the index of refraction of the material in the laser resonator, Δz is the distance between mirrors, and R_1 and R_2 are the radii of curvature of the mirrors. One may recognize that the matrix in equation (132) will always have a determinant of 1. The eigenvalues, γ_i, of the ABCD matrix in equation are (132) are also recognized as the transverse growth factors that the field experiences for each pass through a laser resonator cavity and may be written as

$$\gamma_1, \gamma_2 = m \pm \sqrt{m^2 - 1}\,, \tag{133}$$

where m is

$$m = \frac{(A+D)}{2} = 2\left(1-\frac{\Delta z}{R_1}\right)\left(1-\frac{\Delta z}{R_2}\right) - 1\,. \tag{134}$$

Using the previously qualitative definition for stability, a stable system requires $|\lambda_1|, |\lambda_2| = 1$. In order for this to be true, a stable system requires the discriminant in equation (133) to be imaginary or zero, or that $m^2 \leq 1$. A stable resonator will therefore have the following relationship for cavity parameters

$$0 \leq \left(1-\frac{\Delta z}{R_1}\right)\left(1-\frac{\Delta z}{R_2}\right) \leq 1\,, \tag{135}$$

or

$$0 \leq g_1 g_2 \leq 1\,, \tag{136}$$

where the definition of g_1 and g_2 are

$$g_1 = 1 - \frac{\Delta z}{R_1}\,, \tag{137}$$

$$g_2 = 1 - \frac{\Delta z}{R_2}\,. \tag{138}$$

Figure 9 is a stability diagram indicating in gray laser resonator stability parameters, g_1 and g_2, representing a stable resonator configuration.

Understanding Cavity Resonator Parameters

Due to the parameter-scan nature of the research, many equivalent numbers were used as dimensionless quantities for the simulation. This section derives and defines three of those dimensionless quantities.

Gordon[33] summarized the equivalence relations for a bare laser cavity by drawing equivalence relations from Fresnel integral propagator. He summarized the integral equations as

$$\gamma_1 U_1(x_1) = \sqrt{\frac{ik}{2\pi\Delta z}} \int_{-a_2}^{a_2} K(x_1, x_2) U_2(x_2)\, \mathrm{d}x_2\ , \tag{139}$$

$$\gamma_2 U_2(x_2) = \sqrt{\frac{ik}{2\pi\Delta z}} \int_{-a_1}^{a_1} K(x_2, x_1) U_1(x_1)\, \mathrm{d}x_1\ , \tag{140}$$

to describe the propagation of field of a strip mirror defined by a single coordinate, x_1, to a strip mirror defined by another single coordinate, x_2. Equations (139) and (140) contain a kernel function, defined as

$$K(\vec{\mathbf{x}}_1, \vec{\mathbf{x}}_2) = K(\vec{\mathbf{x}}_2, \vec{\mathbf{x}}_1) = e^{-i\left(\frac{k}{2\Delta z}\right)\left[g_1 x_1^2 + g_2 x_2^2 - 2x_1 x_2\right]}\,, \tag{141}$$

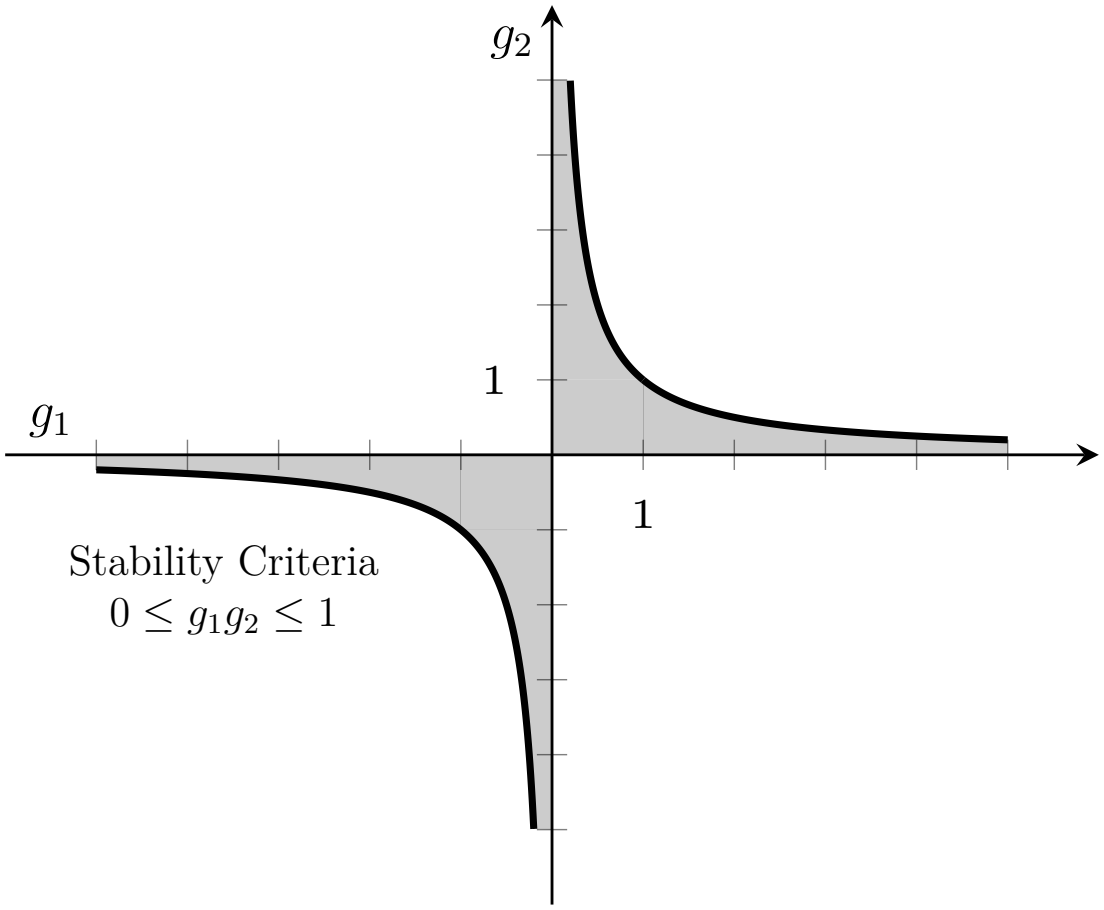

Figure 9. The stability diagram highlighting bare cavity laser resonator parameters which will give stable laser cavity behavior.

for which both the mirror and propagator operations defined in equations (58) and (53) have been wrapped into the g_1 and g_2 parameters defined in equations (137) and (138).

Making the system dimensionless requires the following two substitutions for the single dimension variables in equations (139), (140) and (141),

$$x_i = a_i \xi_i \qquad \text{for} \qquad i = 1, 2\,, \tag{142}$$

and

$$v_i(\xi_i) = u_i(\xi_i)\sqrt{a_i} \qquad \text{for} \qquad i = 1, 2\,. \tag{143}$$

When these dimensionless units are applied, they transform equation (141) into

$$K(\xi_1, \xi_2) = K(\xi_2, \xi_1) = e^{-i(\pi N_{\text{col}})\left[G_1 \xi_1^2 + G_2 \xi_2^2 - 2\xi_1 \xi_2\right]}\,, \tag{144}$$

with equations (139) and (140) becoming

$$\gamma_1 v_1(\xi_1) = \sqrt{iN_{\text{col}}} \int_{-1}^{1} K(\xi_1, \xi_2) v_2(\xi_2)\, \mathrm{d}\xi_2\ , \tag{145}$$

$$\gamma_2 v_2(\xi_2) = \sqrt{iN_{\text{col}}} \int_{-1}^{1} K(\xi_2, \xi_1) v_1(\xi_1)\, \mathrm{d}\xi_1\ . \tag{146}$$

The three dimensionless quantities defined in equations (145) and (146) are defined as

$$N_{\text{col}} \equiv \frac{a_1 a_2 k}{2\pi \Delta z}\,, \tag{147}$$

$$G_1 \equiv g_1 \left(\frac{a_1}{a_2}\right), \tag{148}$$

$$G_2 \equiv g_2 \left(\frac{a_2}{a_1}\right), \tag{149}$$

where a_1 and a_2 may be related by the geometric magnification of the system

$$a_2 = Ma_1 \,. \tag{150}$$

The collimated Fresnel number, N_{col}, will be an important parameter defining the number of fringes seen within the output wave of an unstable resonator. The collimated Fresnel is related to two other important parameters measuring the Fresnel number, N_{f}, based upon the small mirror

$$N_{\text{f}} = \frac{ka_1^2}{2\pi\Delta z} \,, \tag{151}$$

and the outer Fresnel number

$$N_{\text{f,O}} = \frac{ka_2^2}{2\pi\Delta z} \,. \tag{152}$$

In general, Fresnel numbers measure the number of Fresnel zones or ripples across a diameter. The Fresnel number, defined in equation (151), is very important in determining the losses of cavity modes in the stable and unstable resonator. The outer Fresnel number, defined in equation (152), is useful for determining the computational effort that is required for different simulations. A final Fresnel number called the equivalent Fresnel number, N_{Eq}, which will be defined later for the unstable resonator is used to determine multi-modal competition within unstable resonator cavities.

Comparing the Methods to the Analytic Solution for a Stable Resonator

In order to ensure that the eventual analysis with gain included is giving correct results, the methods will be verified against prior calculated results. These prior results range from being analytic, in the case of the stable resonator, to numeric, in the case of the unstable resonator.

This section will devote itself to the solution of the stable resonator with both DEM and the Fox and Li Itreation using both the FFP and ASM. The reason for the analysis is that the stable resonator has analytic solutions which are defined by the transverse electric and magnetic fields, $\text{TEM}_{m,n}$, where m and n identify the mode number. These solutions for a plane z are the Hermite-Gaussian modes,

$$\psi_{n,m}(x,y) = \left(\frac{2}{\pi}\right)^{1/2}\left(\frac{e^{i[(2n+1)\psi_x(z)+(2m+1)\psi_y(z)]}}{2^{n+m}n!m!w_x(z)w_y(z)}\right)^{1/2} H_n\left(\frac{\sqrt{2}x}{w_x(z)}\right)H_m\left(\frac{\sqrt{2}y}{w_y(z)}\right)e^{-ikz-i\frac{kx^2}{2R_x(z)}-i\frac{ky^2}{2R_y(z)}-\frac{x^2}{w_x(z)}-\frac{y^2}{w_y(z)}}, \quad (153)$$

where $H_n(x)$ is a Hermite polynomial of degree n, R_y and R_x are the curvatures of the wave respective of x and y, w_x and w_y are the respective beam waists in x and y, and ψ_x and ψ_y are the respective x and y phase shifts.

The Bare Cavity Half-Symmetric Resonator.

Figure 10 illustrates the stable resonator shown for the analysis of the numeric methods. The specific layout used for the simulation was the half-symmetric confocal resonator, defined by a concave and flat mirror ensemble, with the distance between the mirrors, Δz, set to be half the radii of curvature of the concave mirror. This specific stable resonator is equivalent in configuration to the stable negative branch confocal resonator. However, its position on the stability diagram places is at $g_1, g_2 = 1, \frac{1}{2}$ which is assumed to be more stable in relation to the actual stable negative branch confocal configuration located at $g_1, g_2 = 0, 0$, which is close to an unstable regime. The increased stability associated with the half-symmetric confocal resonator prevents minor numerical error, associated floating point and round-off, from causing unstable answers to develop in the numeric analysis system.

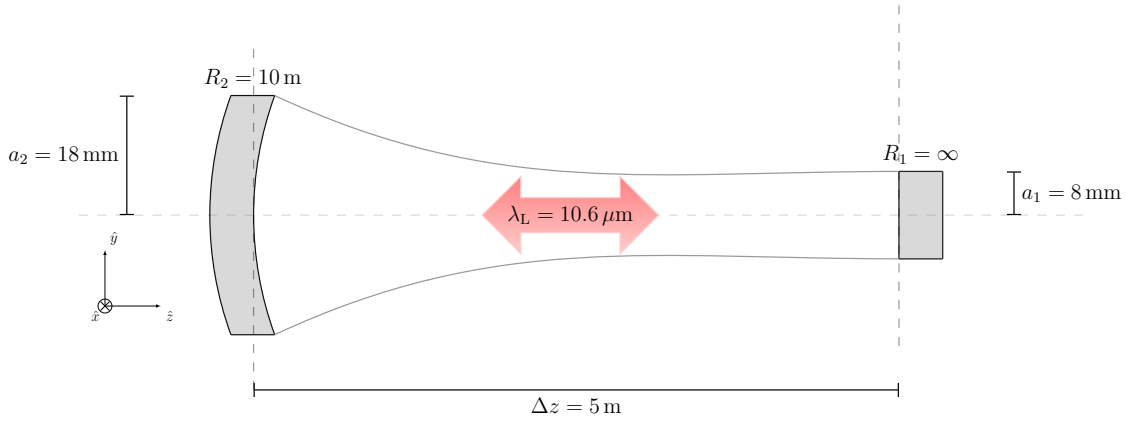

Figure 10. Geometry of the half-symmetric confocal resonator.

The mode present in the system should be the Hermite-Gaussian solution defined in equation (153), with a minimum beam waist located at the flat mirror. The analytic Hermite Gaussian $\mathrm{TEM}_{0,0}$ Mode is shown in figure 11. The next lowest loss analytic mode, $\mathrm{TEM}_{0,1}$, is then shown in figure 12. These analytically determined modes may then be compared with the results from the three different calculation methods highlighted in chapter II. The above analytic solutions do not take account of the finite radii of the circular mirrors. The losses due to diffraction associated with limited extent of the mirrors will modify the solution from the methods, so that the actual mode will be different than the predicted modes above by a small extent. The radii of extent of the mirrors in figure 10 are

$$\begin{aligned} a_1 &= 0.8\,\mathrm{cm}\,, \\ a_2 &= 1.8\,\mathrm{cm}\,, \end{aligned} \tag{154}$$

with the radii of curvature of the concave mirror is $R_2 = 10\,\mathrm{m}$ and a mirror distance of $\Delta z = 5\,\mathrm{m}$. The assumed wavelength of the radiation between both mirrors is $10.6\,\mu\mathrm{m}$ corresponding to a CO_2 laser, which was chosen to compare to previous papers by Siegman, Sziklas, and Yuanying [27, 31, 32, 28] published on the unstable resonator. These dimensions were chosen to coincide with a cavity representing a system with

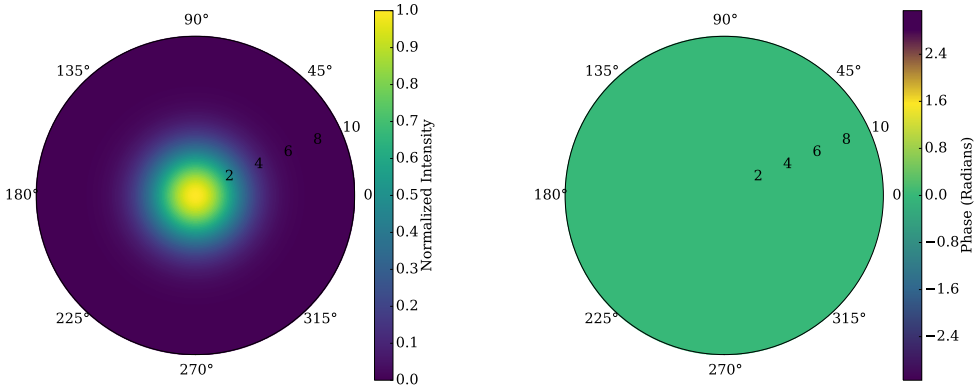

(a) Normalized Intensity **(b) Phase**

Figure 11. Contour plots of the $TEM_{0,0}$ mode of as predicted by the analytic analysis of a stable resonator.

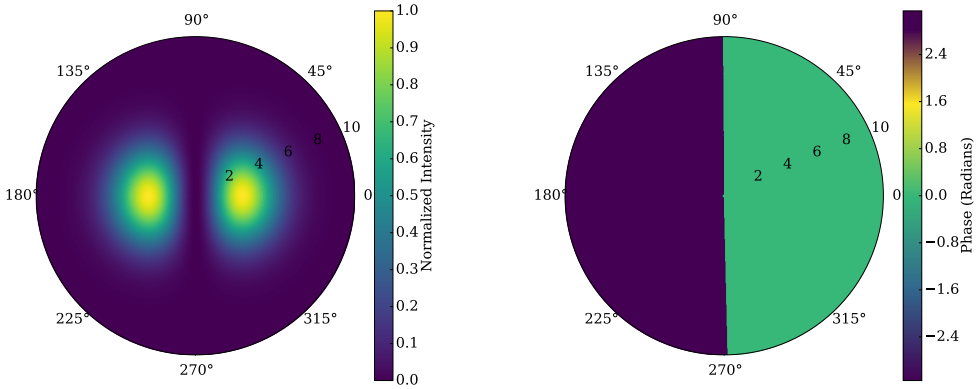

(a) Normalized Intensity **(b) Phase**

Figure 12. Contour plots of the $TEM_{0,1}$ mode of as predicted by the analytic analysis of a stable resonator.

$N_f = 1.201$ which was calculated to give an appropriate mode loss that will lead to $TEM_{0,0}$ being the dominate mode of the cavity while minimizing the diffractive effects of limited mirror extent.

Comparison of Analytic, Direct Eigenvector Method (DEM), Fresnel Forward Propagator (FFP), and Angular Spectrum Method (ASM) Calculated Results.

As stated previously, DEM calculates all the modes associated with the bare cavity stable resonator. For the stable resonator, contour plots of the transverse intensity and phase at the flat mirror are shown in figure 13 of the least-loss mode, $TEM_{0,0}$. Contour plots of the second least-loss mode's, $TEM_{1,0}$, intensity and phase are also presented in figure 14. From both of the contour plots one may see good agreement between DEM and the analytic methods. However, there was a minor discrepancy with the contour plots of phase due to the limited extent of the mirrors simulated. The absolute value of the eigenvalues determined with DEM are pictured in figure 15. Roughly three regimes exist within the plot of eigenvalue as a function of the least loss mode, the first representing a gradual slight decrease in the eigenvalues which come about due the most of the energy of the modes being contained within the the mirror. The next region has a much larger increase in loss as the mode increases when the mode is larger than can be supported by the mirrors. Finally, the region representing the limit of associated with numerical error located at the end of the curve. The eigenvalues are color coded to highlight that there are degenerate cavity modes possessing the same eigenvalue. This degeneracy is due to the radial symmetry of the mirrors.

The $TEM_{0,0}$ mode were also numerically calculated with the FFP and ASM methods and are shown in the contour plots in figure 16 and figure 17 respectively. In

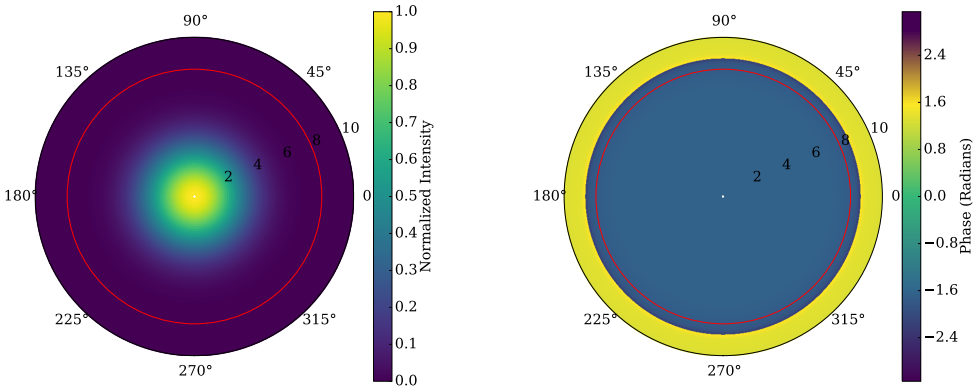

(a) Normalized Intensity **(b) Phase**

Figure 13. Contour plots of the $TEM_{0,0}$ mode predicted by DEM for the half-symmetric confocal stable resonator. The red line indicates the edge of the outcoupling mirror, the transverse field in the red circle is not transmitted out of the cavity.

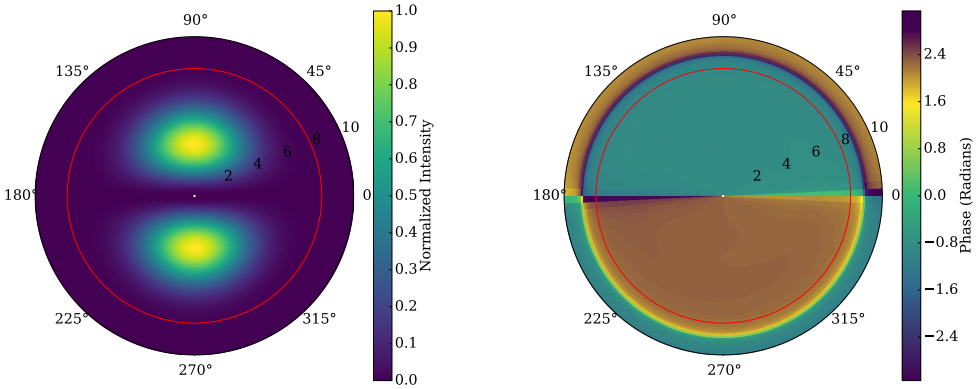

(a) Normalized Intensity **(b) Phase**

Figure 14. Contour plots of the $TEM_{1,0}$ mode predicted by DEM for the half-symmetric confocal stable resonator. The red line indicates the edge of the outcoupling mirror, the transverse field in the red circle is not transmitted out of the cavity.

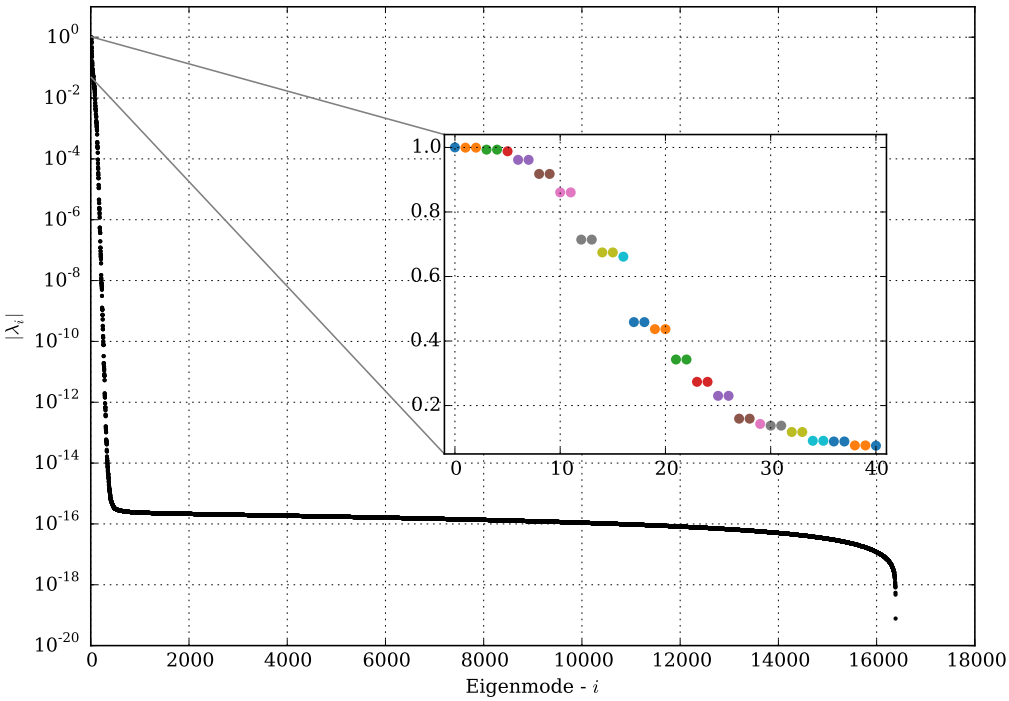

Figure 15. The absolute value of the eigenvalue plotted against mode number, where mode numbers are defined by the lowest loss to the greatest loss mode. Eigenvalues next to each other sharing a color indicate degenerate modes with the same eigenvalue.

both cases, there is rough agreement with the $TEM_{0,0}$ modes previously calculated with DEM and the analytically determined modes. Due to the nature of Fox and Li iteration methods, only the least loss mode of the stable resonator was calculated.

In order to further verify the solutions, the two-dimensional intensity information is also plotted as a one-dimensional function of radius in figure 18. One may notice a couple of important take-aways from the figure, the first is that all three modes do not match the analytic solution for a stable mode and the second is that all three methods match each other. The difference suggests that the methods are capturing a real physical effect. As mentioned previously, the analytic solution to the problem does not consider the diffraction effects associated with a finite mirror. By changing the size of the mirror and then recalculating the mode using ASM for each mirror size one can verify that the mode calculated through numeric methods will approach the mode calculated analytically. Figure 19 shows that as the radii of the small mirror, a_1 is increased, the predicted cavity mode converges to the analytic solution of the system for ASM, indicating that the differences between the mode computed numerically with DEM, ASM, and FFP and the computed analytically is the apodization caused by the finite extent of the mirrors.

Furthermore, the effects of diffraction on the least loss mode may be approximated by multiplying the intensity of the $TEM_{0,0}$ mode by the "jinc" function defined by Goodman in his book, *Introduction to Fourier Optics*[30],

$$I(x,y) = P_{\text{Tot}} e^{-2\left(\frac{r}{w}\right)^2} \left[\frac{2w\mathrm{J}_1\left(\frac{\pi r}{w}\right)}{\pi r}\right]^2, \tag{155}$$

where J_1 is the first order Bessel function. The "jinc" function was identified by Siegman as the Farfield apodization of a circular aperture, and was used to approximate the Farfield of a diffracted stable resonator. In this research, it may be used to approximate the diffractive effects of the small mirror with an example comparison

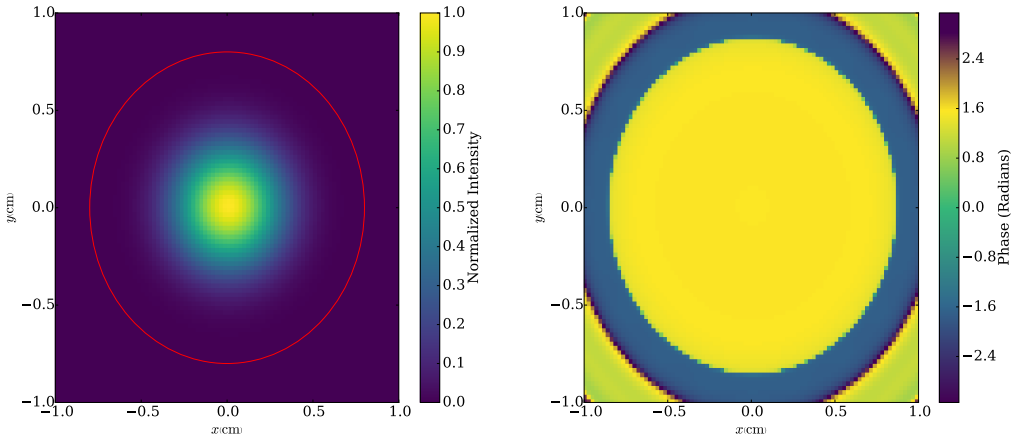

(a) Normalized Intensity (b) Phase

Figure 16. Contour plots of the $TEM_{0,0}$ mode predicted by FFP for the half-symmetric confocal stable resonator. The red line indicates the edge of the outcoupling mirror, the transverse field in the red circle is not transmitted out of the cavity.

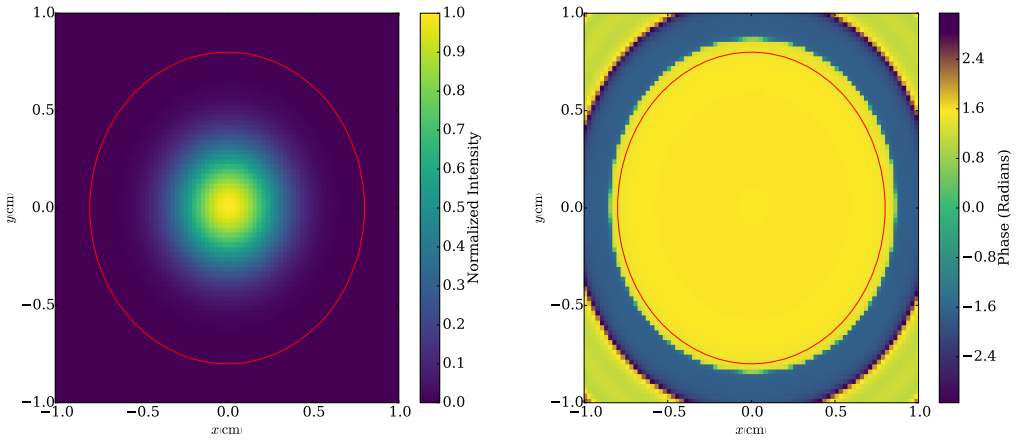

(a) Normalized Intensity (b) Phase

Figure 17. Contour plots of the $TEM_{0,0}$ mode predicted by ASM for the half-symmetric confocal stable resonator. The red line indicates the edge of the outcoupling mirror, the transverse field in the red circle is not transmitted out of the cavity.

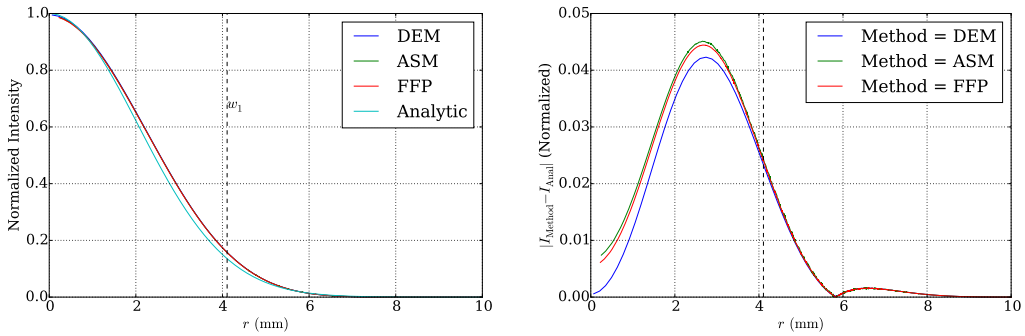

(a) Normalized intensity of all methods

(b) The difference between the three methods and the analytic solution

Figure 18. The comparison of DEM, FFP, and ASM methods against the analytic solution for the half-symmetric stable resonator.

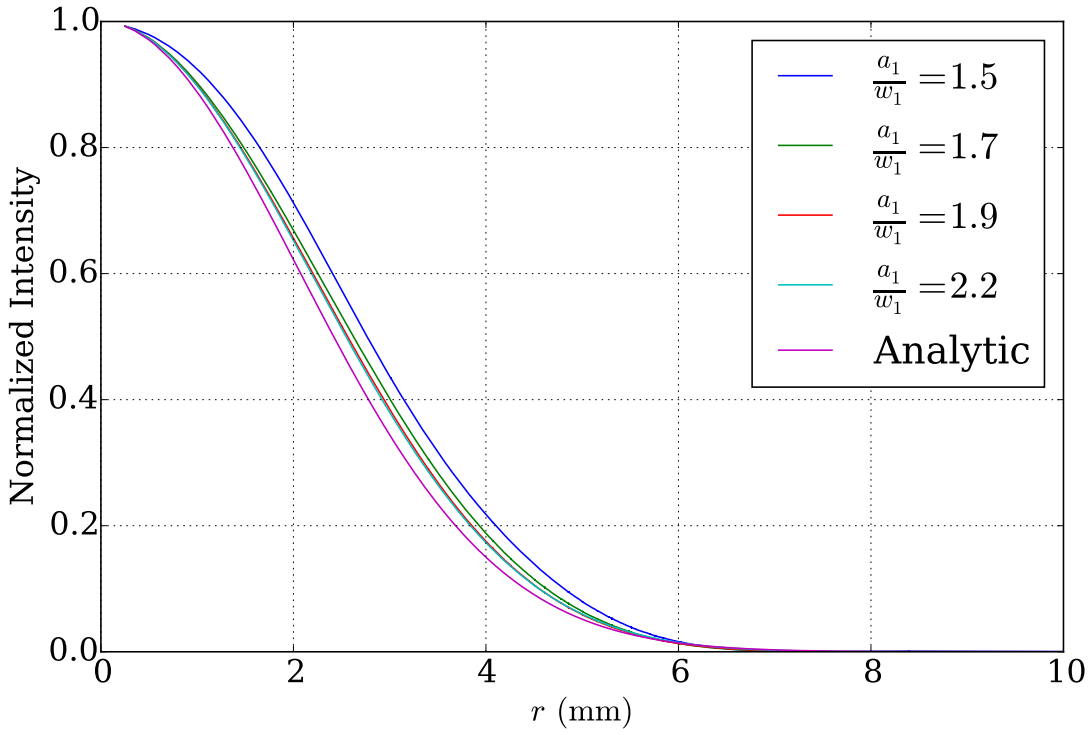

Figure 19. A series of ASM results of the mode intensity indicated that as the radii of the small mirror is increased, the mode calculated with ASM approaches the analytic solution of the system.

shown in figure 20. When comparing figure 20 with figure 18, many features are found to be shared between the ideal and diffracted mode example and the comparison of the numeric and analytic modes. Two regions within the output mode seem to be shared between both simulations. The first occurs a little prior to the beam waist of the $TEM_{0,0}$ mode, with a difference observed between the ideal and diffracted modes of approximately 4% for both the numeric and analytic mode comparison as well as for the ideal and diffracted example. The second difference occurs at a radial distance that is twice the beam waist of the system, with a small bump that is approximately 0.1% the normalized intensity. These similarity of differences and the change in the mode predicted by ASM as the radius of the small mirror is varied further indicates the differences between the the mode calculated with ASM, FFP, and DEM and the Hermite-Gaussian Modes of a stable resonator are due to the diffraction induced by the finite mirror extent of the numeric simulations.

The Unstable Resonator

Stable laser resonators are desired because of the low cavity diffractive losses that occur when the mirrors are no longer assumed to be infinite. The lack of apodization in the system also means that stable laser resonators are well understood, with transverse fields following the Hermite-Gauss Modes[35]. However, stable resonators tend to have mode competition as the Fresnel number of the cavity increases. The simple stable resonator layout illustrated above also requires any output to be transmitted through the output coupler, which means that absorption of laser radiation within the output coupler may become a problem in higher power systems.

These problems may be dealt with by using an unstable resonators. Siegman[36] summarized the beneficial properties of unstable resonators in three parts:

1. Capability to have large mode volumes

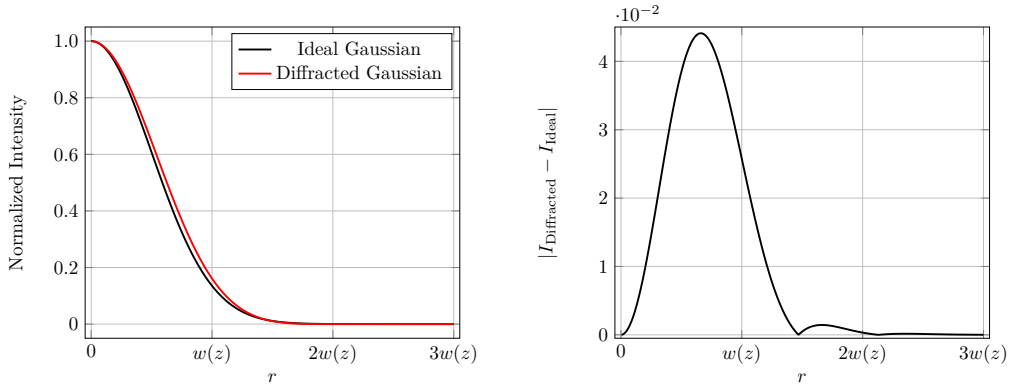

(a) Normalized Intensity of ideal Gaussian mode and a "diffracted" mode.

(b) The Difference in Normalized Intensity of ideal Gaussian mode and a "diffracted" mode.

Figure 20. The comparison of an ideal Gaussian mode compared to a "diffracted" mode. The difference between the two is similar to the one shown in figure 18.

2. Adjustable diffractive output coupling

3. Discrimination of higher order transverse modes

which are ideal for high power, high gain laser resonators. He also recognized a specific class of unstable resonators which have a collimated beam output, the confocal resonators.

Due to the ever-increasing transverse fill of the mode per pass in the laser cavity, aperture effects will play a role in understanding the properties of an unstable resonator. In fact, methods to determine unstable resonator modes have been built using the diffraction caused by the apodization[37, 38] of the output mirror. As the geometric optics helped in achieving understanding regarding stable cavity laser operation, unstable cavity laser operation may also be understood through geometric optics. A helpful parameter for understanding an unstable cavity is the geometric loss.

The shape of the mirrors in an unstable resonator will determine the geometric loss of the cavity. In an actual wave-optic analysis of a system, geometric loss will be coupled with diffractive losses allowing for the determination the total loss of the

cavity. Verdeyen[39] provides excellent illustrations of this loss shown in the initial pass of the laser through the cavity, displayed in figure 21, and the return pass of the radiation through the cavity, displayed in figure 22.

Based upon the setup of figure 23, the following relationship must be true for the initial pass

$$\frac{1}{(r_1+1)\Delta z} - \frac{1}{r_2 \Delta z} = \frac{2}{R_2}\,, \tag{156}$$

where r_1 is the normalized distance of the image plane from the mirror. r_1 is normalized by the distance between the mirrors, Δz, and the radius of curvature of second mirror, R_2. Equation (156) may be rewritten using the definition of g_2 in equation (138) to be

$$\frac{1}{(r_1+1)} - \frac{1}{r_2} = 2(g_2 - 1)\,. \tag{157}$$

Conversely, the return pass described in figure 22, is related to the stability definition in equation (137) by

$$\frac{1}{(r_2+1)} - \frac{1}{r_1} = 2(g_1 - 1)\,. \tag{158}$$

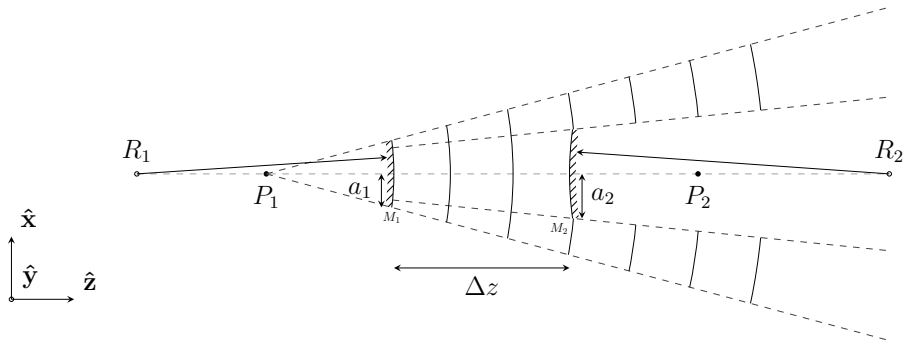

Figure 21. Pictoral description of initial radiation pass through the cavity. The figure is from Verdeyen's *Laser Electronics* textbook[39], specifically from the chapter concerning unstable resonators.

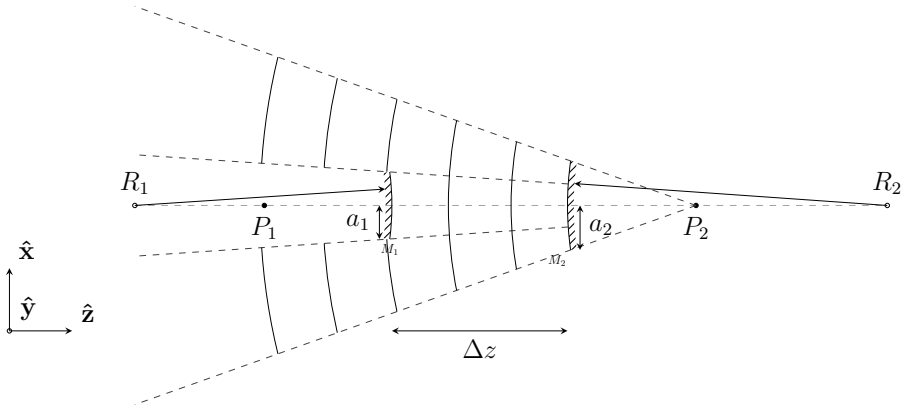

Figure 22. Pictoral description of return radiation pass through the cavity. The figure is from Verdeyen's *Laser Electronics* textbook[39], specifically from the chapter concerning unstable resonators.

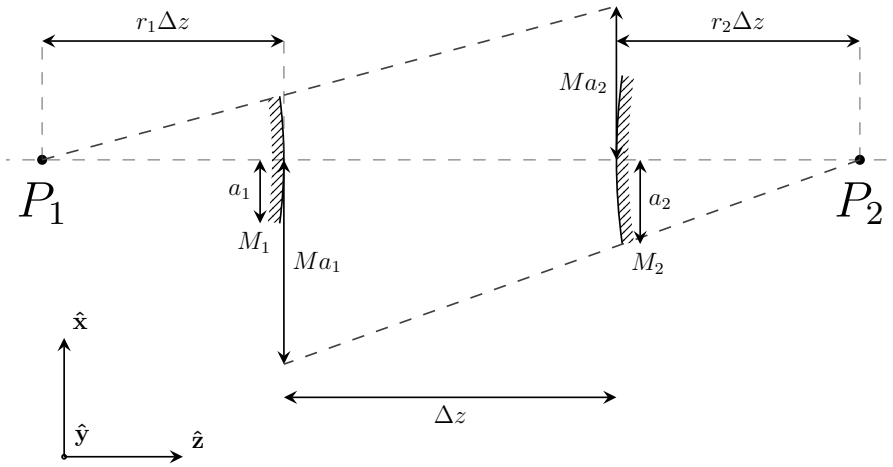

Figure 23. Cavity geometry in the unstable resonator, notice that the distance of imaged points from the mirror are described in normalized units $\Delta z r_1$. The figure is from Verdeyen's *Laser Electronics* textbook[39], specifically from the chapter concerning unstable resonators.

The symmetry displayed in r_1 and r_2 allows for equations (157) and (158) to be written as a system of equations defined by the stability parameters

$$\begin{aligned} r_1 &= \frac{\left[1-(g_1g_2)^{-1}\right]^{1/2}-1+g_1^{-1}}{2-g_1^{-1}-g_2^{-1}}\,, \\ r_2 &= \frac{\left[1-(g_1g_2)^{-1}\right]^{1/2}-1+g_2^{-1}}{2-g_1^{-1}-g_2^{-1}}\,, \end{aligned} \tag{159}$$

where r_1 and r_2 are now recognized to be the distances to the cavity's virtual sources, which are inherent to the mirrors in the system. The above geometries indicate that the reflected power going from one mirror to the other is the solid angle of the reflected power over the total angular extent of the wave. Therefore, the power reflected on the initial pass is going to be

$$\begin{aligned} \Gamma_2 &= \frac{\text{solid angle of } M_2 \text{ with origin at } P_1}{\text{angular extent of wave originating at } M_2}\,, \\ &= \frac{\frac{\pi a_2^2}{4\pi(r_1+1)^2d^2}}{\frac{\pi a_2^2}{4\pi r_1^2 d^2}}\,, \\ &= \frac{r_1^2}{(r_1+1)^2}\,, \end{aligned} \tag{160}$$

and for the return pass the amount reflected will be

$$\begin{aligned} \Gamma_1 &= \frac{\text{solid angle of } M_1 \text{ with origin at } P_2}{\text{angular extent of wave originating at } M_1}\,, \\ &= \frac{\frac{\pi a_2^2}{4\pi(r_2+1)^2d^2}}{\frac{\pi a_2^2}{4\pi r_2^2 d^2}}\,, \\ &= \frac{r_2^2}{(r_2+1)^2}\,. \end{aligned} \tag{161}$$

The product of the survival factors, Γ_1 and Γ_2, defined in equations (160) and (161) is the total fraction of power, Γ, that survives a round-trip

$$\Gamma^2 = \Gamma_1\Gamma_2 = \left[\frac{r_1 r_2}{(r_1+1)(r_2+1)}\right]^2, \tag{162}$$

or more simply

$$\Gamma = \pm\frac{r_1 r_2}{(r_1+1)(r_2+1)}\,. \tag{163}$$

Equation (159) then allows for the cavity survival to be defined by the product of $g_1 g_2$,

$$\Gamma = \pm\frac{1-\left[1-(g_1g_2)^{-1}\right]^{1/2}}{1+\left[1-(g_1g_2)^{-1}\right]^{1/2}}\,. \tag{164}$$

If $0 < g_1 g_2 < 1$ the quantity in the square root of equation (164) is imaginary, which means that there is no loss predicted by geometric optics for a stable resonator with non-transmissive mirrors. The sign of $g_1 g_2$ gives two different branches for equation (164)

$$\begin{array}{rr} \text{Positive Branch} & \text{Negative Branch} \\ g_1g_2 > 1 & g_1g_2 < 0 \\ \Gamma = \dfrac{1-\left[1-(g_1g_2)^{-1}\right]^{1/2}}{1+\left[1-(g_1g_2)^{-1}\right]^{1/2}} & \Gamma = \dfrac{\left[1-(g_1g_2)^{-1}\right]^{1/2}-1}{\left[1-(g_1g_2)^{-1}\right]^{1/2}+1} \end{array} \tag{165}$$

which may then be rewritten in terms of the product of $g_1 g_2$

$$g_1g_2 = \tfrac{(\Gamma+1)^2}{4\Gamma} \quad g_1g_2 = -\tfrac{(1-\Gamma)^2}{4\Gamma}\,. \tag{166}$$

The above equation allows for the addition of loss contours to figure 9 displayed in figure 24. For which the geometric loss of the cavity increases as the stability parameters of the cavity increase.

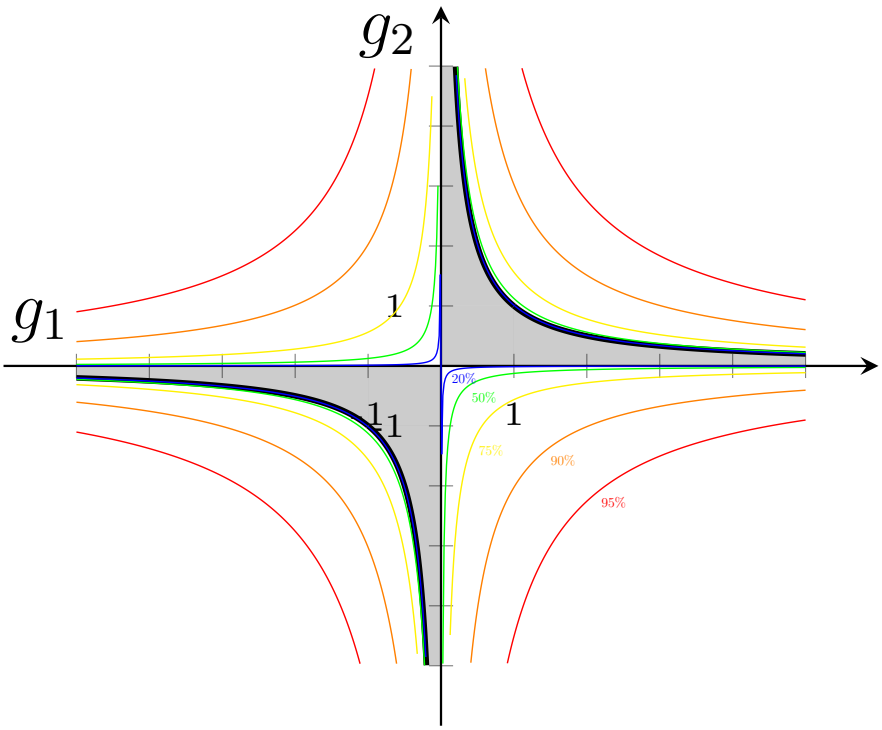

Figure 24. $g_1 g_2$ **stability plot including the losses represented in contours along the plot.**

Yuanying's Unstable Resonator

After verifying the methods with the stable resonator, the methods were applied to the topic of this research, unstable laser cavities. Unfortunately, the unstable resonator as indicated prior has modes that are not easily expressed in terms of analytic functions. In order to further verify the simulation methods, the modes predicted by the three methods for two different previously published unstable resonator configurations were compared with each other and the results previously published. The first resonator was pulled from Yuanying's 2004 paper[28] in which he pioneers the 2D expansion of the DEM originally investigated by Siegman in his Prony Paper[27]. Further discussion of the results associated with that method will be discussed in section .

Yuanying's simulation involved looking at an Unstable Resonator resonator for stability parameters

$$\begin{aligned} g_1 &= 1.525\,, \\ g_2 &= 0.740\,. \end{aligned} \tag{167}$$

The actual dimensions of the layout are illustrated in figure 25. Yuanying solved the above cavity configuration using DEM. He then propagated the cavity mode to the farfield. The farfield prediction was then qualitatively compared to experiment.

For the comparison of the three mode calculation methods, the cavity mode configuration based on Yuanying's reported cavity configuration were calculated. The transverse mode intensities at the back mirror were compared as functions of radius. The picture of this comparison is figure 26, which also includes Yuanying's original published results.

The three different methods had good agreement with one another, with a maximum disagreement that was less than 2% of the normalized intensity, attributed to minor aliasing observed in the FFP method. However, the results did not agree with the simulation results presented in Yuanying's paper[28]. It is believed that the difference between the published results and our calculations is due to an issue with

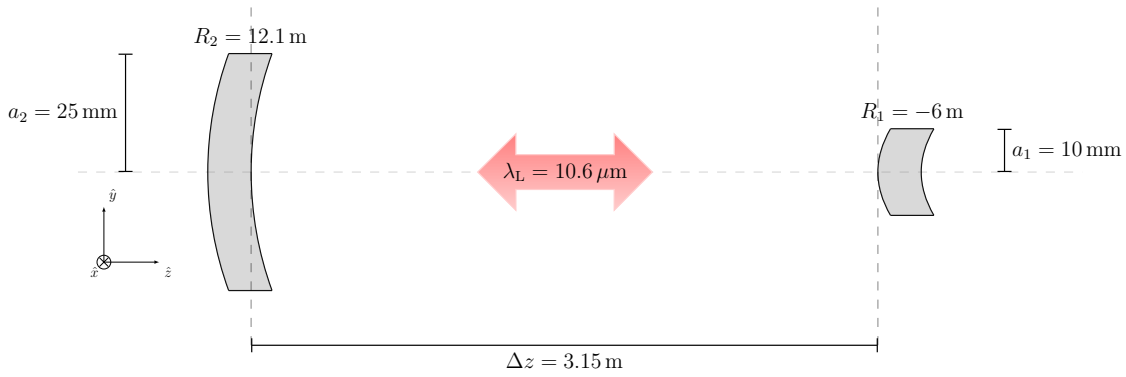

Figure 25. Geometry of the Yuanying unstable resonator.

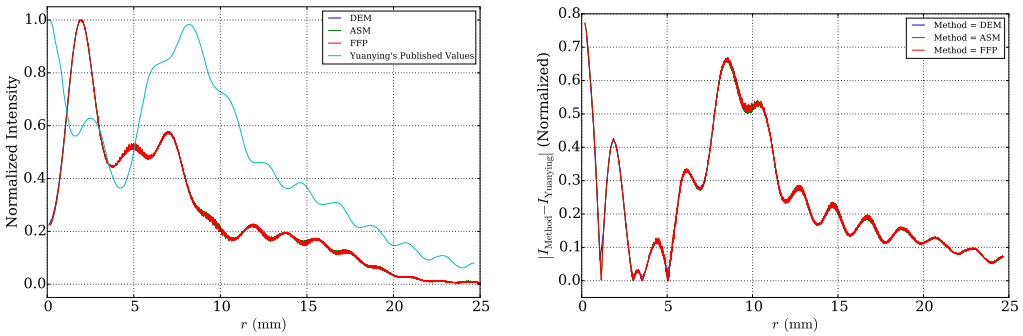

(a) Normalized intensity of all methods and Yuanying's results

(b) The difference between the three methods and Yuanying's results

Figure 26. A comparison radial field intensity for the Yuanying unstable resonator simulated output using FFP, ASM, and DEM, for field on the back mirror. Also plotted are the results originally published by Yuanying[28].

the geometries mentioned within the paper. Further extrapolation of the cavities geometry is difficult due to the non-analytic nature of unstable resonator systems. The survival factors calculated with all three methods were identical, having a value of $|\gamma_0| = 0.682$. Unfortunately, Yuanying did not publish his survival factor calculated with his two-dimensional DEM.

Confocal Resonators

Confocal resonators are a specific type of laser resonator which have the special property for which the laser output field will always have a transversely uniform phase front from the system. In order for the flat phase front to be achieved, the focal points of the two mirrors within the system must sum to the separation between those mirrors[40]

$$\Delta z = f_1 + f_2 = \frac{R_1}{2} + \frac{R_2}{2}\,, \tag{168}$$

where f_i and R_i are mirror i's respective focal points and radii of curvature and Δz is the distance between mirrors. Translating equation (168) into a requirement on the

g_1 and g_2 parameters defined in equations (137) and (138) gives

$$2 = \frac{1}{1-g_1} + \frac{1}{1-g_2}, \tag{169}$$

which when solved for g_2 as a function of g_1 allows marking the confocal resonators on figure 9, shown in figure 27. Equation (168) may be rewritten in terms of products

$$2 - \frac{2\Delta z}{R_1} = 1 + \frac{R_2}{R_1}, \tag{170}$$

and

$$2 - \frac{2\Delta z}{R_2} = 1 + \frac{R_1}{R_2}, \tag{171}$$

which when the definition of equations (137) and (138) are applied gives

$$2g_1 = 1 + \frac{R_2}{R_1}, \tag{172}$$

$$2g_2 = \frac{\left(1 + \frac{R_2}{R_1}\right)}{\frac{R_2}{R_1}}. \tag{173}$$

Multiplying equations (172) and (173) together give

$$g_1 g_2 = \frac{\left(1 + \frac{R_1}{R_2}\right)^2}{4\frac{R_1}{R_2}}. \tag{174}$$

Comparing equation (174) with equation (166) identifies that the survival factor of a confocal resonator is dependent on the ratio of the radii of curvature for a positive branch unstable resonator

$$\Gamma^2 = \left(\frac{R_1}{R_2}\right)^2. \tag{175}$$

Looking at the geometry of the system shown in figure 23, the geometric magnification, M, of the cavity per pass is defined as the inverse of the survival factor, which

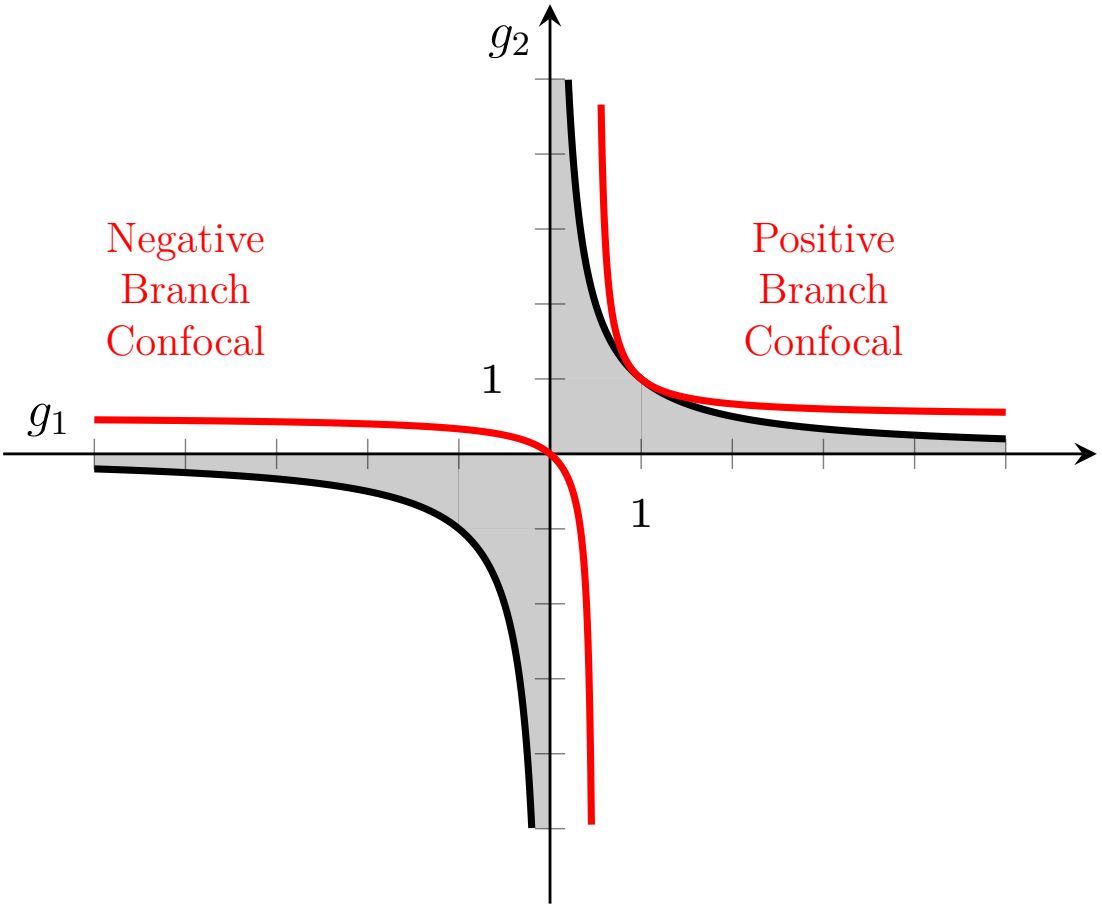

Figure 27. The stability diagram highlighting bare cavity laser resonator parameters which will give stable laser cavity behavior. The negative and positive branches of the confocal requirement are shown in red.

for a positive branch confocal resonator is

$$-\left(\frac{R_2}{R_1}\right) = M\,, \tag{176}$$

and for the negative branch is

$$-\left(\frac{R_2}{R_1}\right) = M\,. \tag{177}$$

The geometric magnification may be used to completely define the resonator radii of curvature for the positive branch confocal resonator

$$\begin{aligned} R_1 &= \frac{2\Delta z}{(1-M)}\,, \\ R_2 &= \frac{2M\Delta z}{(M-1)} \end{aligned} \tag{178}$$

and

$$\begin{aligned} R_1 &= \frac{2\Delta z}{(1-M)}\,, \\ R_2 &= \frac{2M\Delta z}{(M-1)} \end{aligned} \tag{179}$$

for the negative branch confocal resonator.

For the high power applications the positive branch confocal resonator is preferred for use as a laser resonator. The preference is due to a focal point occurring within the cavity of a negative branch confocal resonator[24] which may cause problems within a cavity with the introduction of a gain. The positive branch confocal resonator will produce a collimated output beam, much like a confocal telescope acting in reverse.

Siegman's Unstable Resonator

Siegman's simulation involved looking at a positive branch confocal unstable resonator. The dimensions of the resonator are shown in figure 28. Siegman and Sziklas solved the resonator twice using Fox and Li analysis with an ASM propagator [32] and a propagator involving as Hermite-Gauss Basis [31]. The Hermite Gaussian Basis numerically smoothed over the results removing striations associated with the unstable resonator, and was more computationally intensive then ASM, leading Siegman to abandon the Hermite-Gauss Basis techniques for ASM. A comparison of the three methods is shown in figure 29, showing excellent agreement between the three methods with a difference of less than 2% of the normalized intensity. The methods also agreed qualitatively with the results present in Szikla's and Siegman's paper[32]. A direct comparison with Siegman would have been performed, but Sziklas presented the mode in a three-dimensional plot making it difficult to perform a direct comparison. The eigenvalues calculated with all three methods was $|\gamma| = 0.5634$ which agreed with the calculation performed by Siegman and Sziklas. A contour plot of the intensity and phase of the transverse mode at the output coupler is present in figure 30, illustrating some interesting features associated laser modes present in a confocal resonator. The phase of the mode at the cavity exit is flat, demonstrating

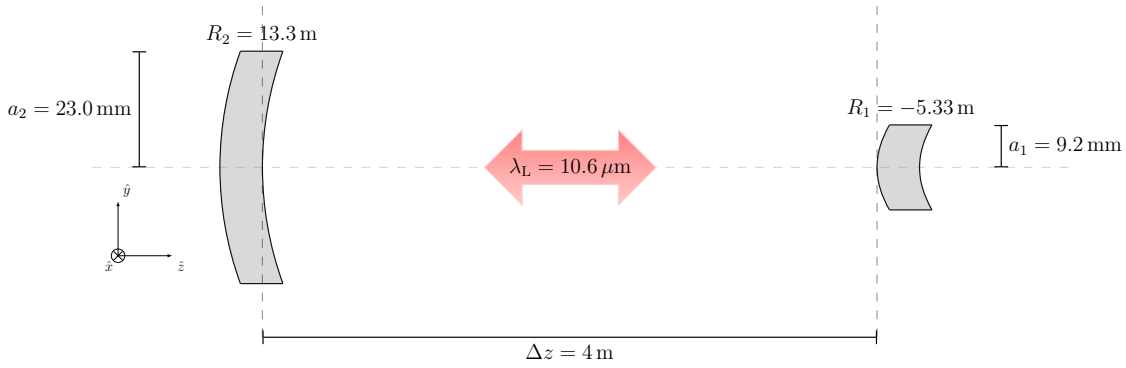

Figure 28. Geometry of the Siegman unstable resonator.

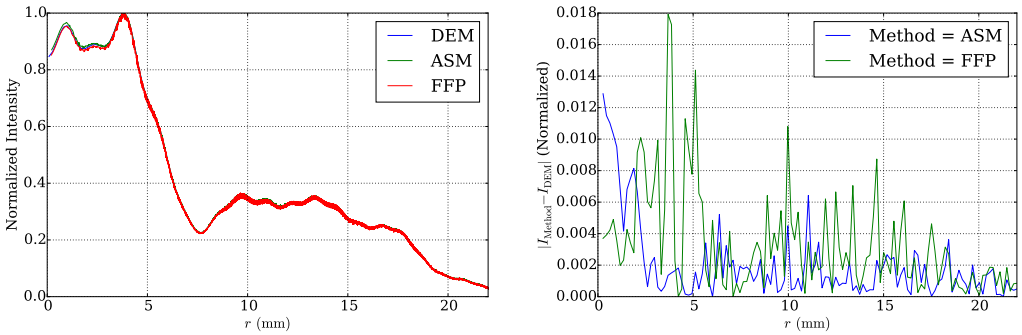

(a) Normalized Intensity of all Methods

(b) The difference between the three methods and the analytic solution

Figure 29. A comparison radial field intensity for the Siegman unstable resonator simulated output using FFP, ASM, and DEM.

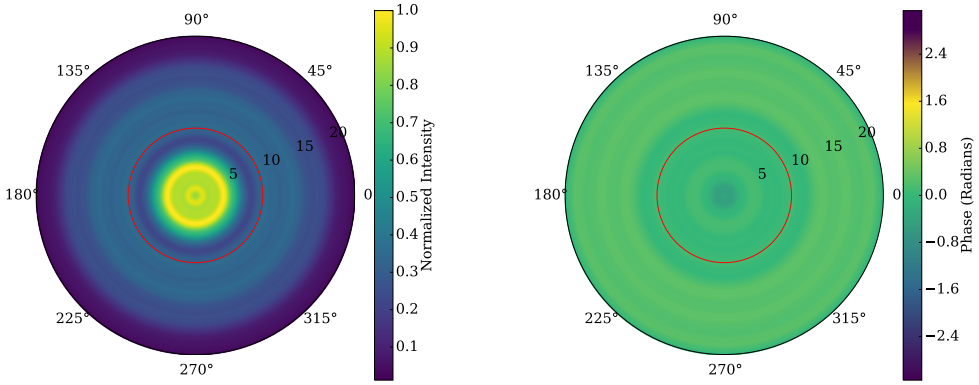

(a) Normalized Intensity

(b) Phase

Figure 30. Contour plots of the bare cavity field output of the Siegman unstable resonator simulated with DEM. The red line indicates the edge of the outcoupling mirror, the transverse field in the red circle is not transmitted out of the cavity.

the collimated nature of a confocal laser cavity. The layout of the intensity within the cavity also shows ringing throughout the mode occurring from the diffractive effects of the smaller mirror shown in figure 28.

The Phase on the Outcoupling Mirrors

An interesting facet of the confocal unstable resonator was the collimated phase observed in the resonator output and pictured in figure 30. Due to the collimated output of the system, the phase of the field incident on the outcoupling mirror will not be uniform transversely on the mirror surface. The difference between the two is counterintuitive to the understanding built with stable resonators. For example, in figure 31 one sees the the phase on the outcoupling mirror is uniform across the mirror surface.

Applying the same analysis of the output wave phase for the Siegman unstable resonator in figure 32, shows that the the phase of the forward traveling wave is not uniform across the outcoupling mirror. However the combination of the phases of the forward traveling wave incident on the outcoupling mirror and the backward traveling mode reflected from the outcoupling mirror are constant. The constant phase of both waves combined on the mirror edge uphold the boundary conditions imposed by the mirrors on the magnetic and electric fields on the system.

A question that arises concerning the non-constant phase of a wave incident on the mirror is, "Why is the phase of the forward traveling wave incident on the outcoupler mirror uniform for a stable resonator, but nonuniform for an unstable resonator?" This question may be answered by observing the phase of the output of a stable resonator when the outcoupler mirror is a much smaller size than the $TEM_{0,0}$ mode. The phases of such a resonator are shown in figure 33. Along the mirror the one-way incident wave's phase is observed to no longer be uniform across the smaller

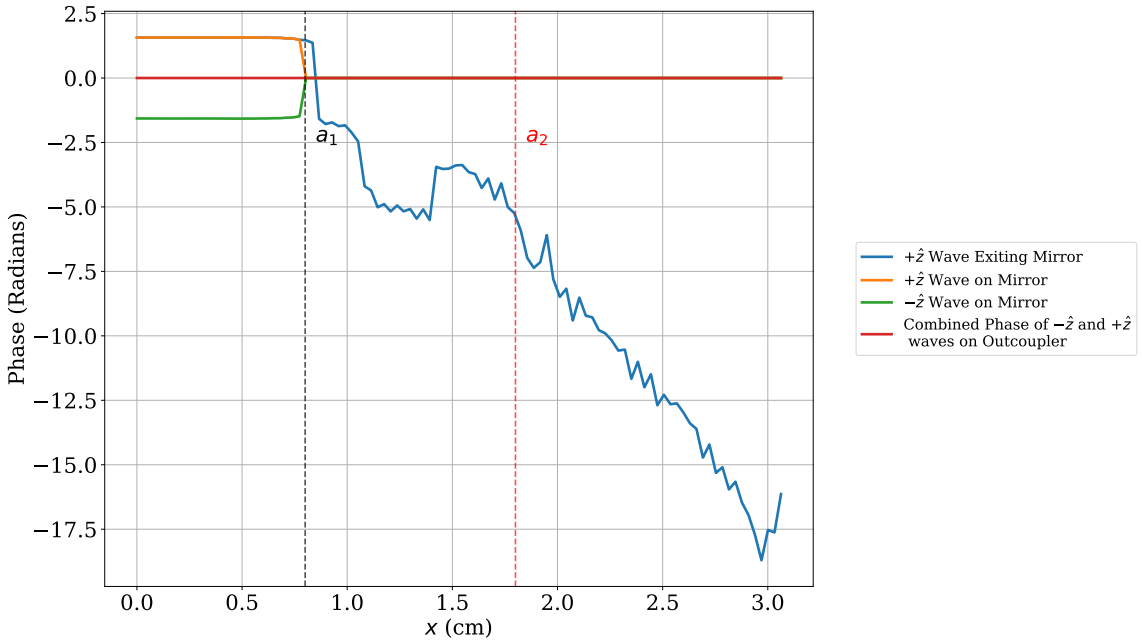

Figure 31. A comparison of the phases of the output field for the half-symmetric confocal stable resonator described in figure 10, the forward and backward traveling field on the actual mirror surface, and the addition of the phases of the forward and backward waves on the mirror edge. The front mirror and back mirror radii, a_1 and a_2, are also displayed.

outcoupler mirror surface. Based upon these results, it is recognized that the non-uniformity of the phase observed in both figure 33 and in figure 32 is due to the diffraction associated with mirror apodization.

The Equivalent Fresnel Number

Siegman identifies that the unstable resonator mode is a superposition of the magnifying and demagnifying wave solutions for an unstable cavity[24]. The parameters of the demagnifying solution may be seen from the geometry in figure 34. The phase imparted by the radii of the mirrors R_0 and R_1 is

$$\begin{aligned} \Delta_0 &= \frac{2\pi}{\lambda}\left[|R_0| - \sqrt{R_0^2 - a^2}\right], \\ \Delta_1 &= \frac{2\pi}{\lambda}\left[|R_1| - \sqrt{R_1^2 - (Ma)^2}\right], \end{aligned} \tag{180}$$

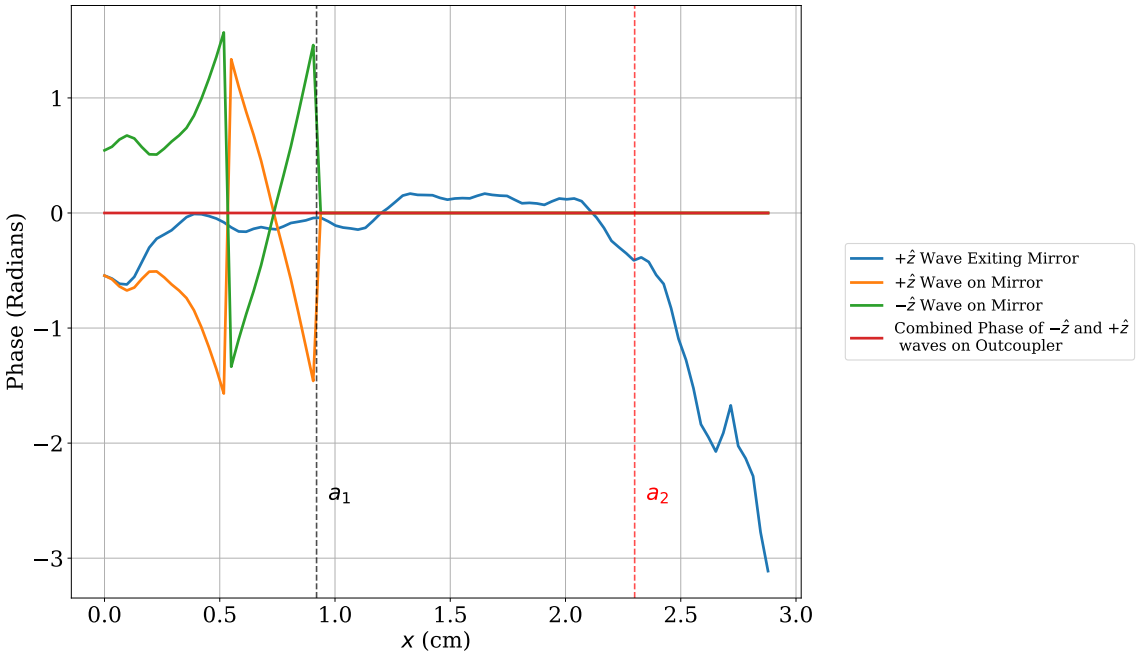

Figure 32. A comparison of the phases of the output field for the Siegman unstable resonator described in figure 28, the forward and backward traveling field on the actual mirror surface, and the addition of the phases of the forward and backward waves on the mirror edge. The front mirror and back mirror radii, a_1 and a_2, are also displayed.

which may be approximated with

$$\begin{aligned} \Delta_0 &= \frac{\pi a^2}{\lambda R_0}\,, \\ \Delta_1 &= \frac{\pi M^2 a^2}{\lambda R_1}\,. \end{aligned} \tag{181}$$

Both phase variations must be the same, $\Delta_0 = \Delta_1$, for the mirrors to have an equivalent effect on the magnifying and demagnifying fields. Therefore, $R_1 = M^2 R_0$ and R_2 must be equal to the summation of R_1 and the propagation distance, Δz

$$R_2 = R_1 + M\Delta z\,, \tag{182}$$

or

$$R_2 = M^2 R_0 + M\Delta z\,. \tag{183}$$

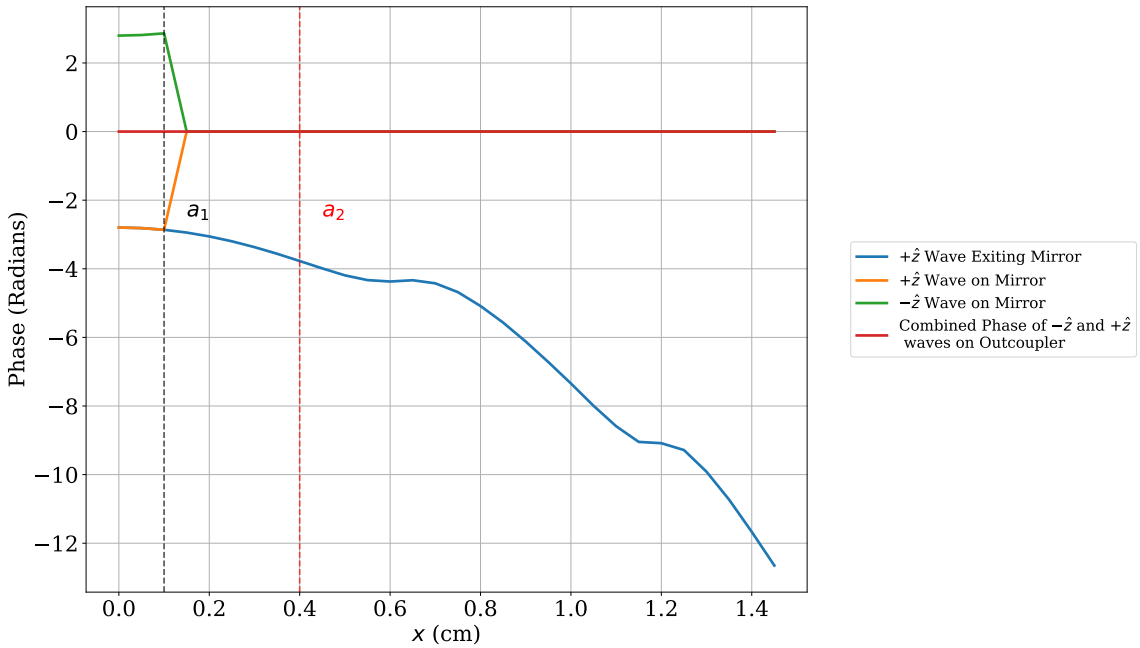

Figure 33. A comparison of the phases of the output field for the half-symmetric confocal stable resonator with a much smaller outcoupling mirror compared to the one described in figure 10, the forward and backward traveling field on the actual mirror surface, and the addition of the phases of the forward and backward waves on the mirror edge. The front mirror and back mirror radii, a_1 and a_2, are also displayed.

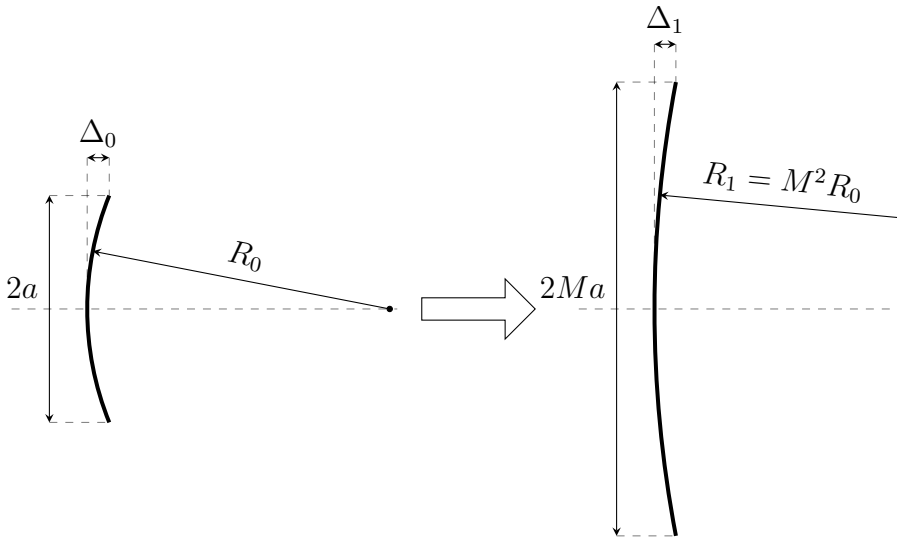

Figure 34. The spherical curvature of a wave from the outcoupling mirror to the back mirror. The magnifying spherical wave has a M^2 term, due to the relationship with the spherical curvature to the overall size of a. The picture is a duplication of the one used by Siegman in his *Lasers* textbook[24] for describing the equivalent Fresnel number.

However, in order to have R_2 replicate the wave for multiple trips, it also must be the same as R_0. Which means that

$$R_0 = M^2 R_0 + M\Delta z\,, \tag{184}$$

and R_0 is solved to be

$$R_0 = \frac{M\Delta z}{1 - M^2}\,. \tag{185}$$

R_0 is negative due to the curvature representing the converging solution of the resonator. The demagnifying solution will be highly dominated by diffraction effects due to the demagnification constantly shrinking the beam to the point where diffraction effects imparted by the aperture growing to dominate the magnifying wave solution. The relative phase difference between the magnification and demagnification solution is used to define the equivalent Fresnel number, N_{eq},

$$|\Delta\phi_{\text{Mag}} - \Delta\phi_{\text{Demag}}|\Big|_{x=a} = \frac{\pi a^2}{|R_0|\lambda} = 2\pi N_{\text{eq}}\,. \tag{186}$$

Equation (186) may be solved for equivalent Fresnel number to get

$$N_{\text{eq}} = \frac{\pi(M^2-1)a^2}{M\Delta z\lambda} = \frac{\pi(M^2-1)Ma^2}{M^2\Delta z\lambda} = \frac{(M^2-1)}{M^2}N_{\text{col}}\,. \tag{187}$$

The equivalent Fresnel number, due to its characterization of the relationship between the demagnifying and magnifying solution's phase becomes an important number when analyzing multimodal behavior of unstable resonators.

Siegman's Single Dimension Direct Eigenvector Method (DEM)

The final comparison of methods for research and prior work was chosen to be a study of the absolute value of cavity eigenvalues as a function of varying Fresnel

number. The comparison was between prior research performed by Siegman[27], Fox and Li iteration using ASM, and DEM. Due to the hard grid constraint, FFP was not included within this analysis.

To compare the modes to Siegman's simplified DEM method[27] required re-deriving the method in order to recalculate the comparison. Originally, Siegman used the Prony Method to compute the eigenvalues of the matrix operation. However, computation has advanced since the work was originally performed in 1970, meaning that the Prony method used to calculate eigenvalues is no longer required to solve the simplified DEM problem.

Siegman assumes circular resonator modes and then splits the envelope function into azimuthal and radial components,

$$U_{nl}(r,\theta) = \varphi_{nl}\left(\frac{r}{a}\right)e^{-il\theta}\,, \tag{188}$$

where the indices n and l are the radial and azimuthal indices, φ_{nl} is the n^{th} radial eigenfunction corresponding to the l^{th} azimuthal index. By separating the azimuthal function, the DEM problem is greatly simplified in determining the cavity mode.

For a symmetric laser cavity, the radial eigenfunctions have a propagation kernel

$$\gamma_{1,n,l}\varphi(x) = i^{l+1}2\pi N_f \int_0^1 y\mathrm{J}_l(2\pi N_f xy)e^{-i\left(\pi N_f g\right)\left(x^2+y^2\right)}\varphi(y)\,\mathrm{d}y\ , \tag{189}$$

where J_l is Bessel function of order l, N_f is the Fresnel number, g is the stability parameter associated by the small mirror The single propagation represents the full travel through the cavity. The circular eigenfunction is orthogonal if written as a function $x^{1/2}\varphi(x)$,

$$\int_0^1 x\varphi_{nl}\varphi_{ml}\,\mathrm{d}x = \delta_{mn}\,. \tag{190}$$

Siegman recognizes presence of the oscillatory Bessel Function, $J_l(2\pi N_f xy)$, requires a sampling of at least eight units per fringe in the cavity, meaning that the computational effort is roughly $\mathcal{O}(N^2)$ versus $\mathcal{O}(N^4)$ computation effort associated with the two-dimensional DEM.

Throughout the rest of Siegman's paper the equivalent Fresnel number, N_{eq}, is used versus the Fresnel number, because the equivalent Fresnel number defines the eigenvalues associated with the changing cavity better than the Fresnel number. Based upon equations (164), (175), and (176), g may be related to the geometric magnification of the positive branch confocal resonator cavity

$$M = g + \left(g^2 - 1\right)^{1/2}, \tag{191}$$

with the equivalent Fresnel number being related to g by

$$N_{\text{eq}} = N_f \left(g^2 - 1\right)^{1/2}. \tag{192}$$

Asymmetric Circular-Mirror Unstable Optical Resonator.

After deriving the above symmetric relationship, Siegman breaks geometric symmetry by generating equivalence relationships between the asymmetric problem's variables and the variables defined within the symmetric problem.

The complete eigenmode may be calculated from two coupled integral equations

$$\gamma_1 \varphi_1(x) = i^{l+1} \left(\frac{2\pi}{\lambda \Delta z}\right) \int_0^{a_2} y \mathrm{J}_l \left(\frac{2\pi xy}{\lambda \Delta z}\right) e^{-i\left(\frac{\pi}{\lambda \Delta z}\right)\left[g_1 x^2 + g_2 y^2\right]} \varphi_2(y)\, \mathrm{d}y \ , \tag{193}$$

$$\gamma_2 \varphi_2(y) = i^{l+1} \left(\frac{2\pi}{\lambda \Delta z}\right) \int_0^{a_1} z \mathrm{J}_l \left(\frac{2\pi yz}{\lambda \Delta z}\right) e^{-i\left(\frac{\pi}{\lambda \Delta z}\right)\left[g_1 z^2 + g_2 y^2\right]} \varphi_1(z)\, \mathrm{d}z \ . \tag{194}$$

If the mirror radius a_2 is larger than the mode size of the mirror so that $\varphi_2(y) \approx 0$ for $y \geq a_2$ then the second integral's upper bound may be considered to be ∞. With

this assumption and a Bessel function identity presented by Bateman[41] equations (193) and (194) may be combined into

$$\gamma_1\gamma_2\varphi(x) = i^{l+1}\left(\frac{\pi a_1^2}{g_2\lambda\Delta z}\right)\int_0^1 y\mathrm{J}_l\left(\frac{\pi a_1^2 xy}{\lambda g_2\Delta z}\right)e^{-i\left(\frac{\pi a_1^2}{2g_2\lambda\Delta z}\right)(2g_1g_2-1)\left(x^2+y^2\right)}\varphi_1(y)\,\mathrm{d}y\ , \tag{195}$$

where g_1, g_2 and the Fresnel number associated with mirror 1, $N_{f,1}$, may be combined to form the generalized parameters defined in the symmetric case

$$N_f = \left|\frac{N_{f,1}}{2g_2}\right|, \tag{196}$$

$$g = |1 - 2g_1g_2|\,, \tag{197}$$

$$|\gamma| = |\gamma_1\gamma_2|\,, \tag{198}$$

$$N_{\mathrm{eq}} = N_{f,1}\left[\frac{g_1}{g_2}(g_1g_2 - 1)\right]^{1/2}. \tag{199}$$

Although the magnitude of γ versus the magnitude of the product of γ_1 and γ_2 is a simple relationship, the actual relationship between γ and $\gamma_1\gamma_2$ is more complex due to the phase associated with the eigenvalues. Taking the stability parameters g_1 and g_2 into account lets the complex value of γ be defined

$$\gamma = \begin{cases} \gamma_1\gamma_2 & (g_1g_2 > 1, g_2 > 0) \\ \gamma_1^\star\gamma_2^\star & (g_1g_2 > 1, g_2 < 0) \\ (-1)^{l+1}\gamma_1^\star\gamma_2^\star & (g_1g_2 < 0, g_2 > 0) \\ (-1)^{l+1}\gamma_1\gamma_2 & (g_1g_2 < 0, g_2 < 0) \end{cases}. \tag{200}$$

Bare Cavity Eigenvalue Study Results

Using the Siegman method presented in the previous section, DEM, and ASM, a study was performed comparing eigenvalues for a resonator system. A baseline geometry defined in figure 35 was used across multiple simulations were ran for positive confocal resonator arrangements with a set geometric magnification of $M = 2$. The wavelength was chosen to be $\lambda = 10.6\,\mu$m to represent a CO_2 laser, and the separation between mirrors, $\Delta z = 4\,$m was held constant. The front mirror radius was varied in order to modify the equivalent Fresnel number. The back mirror radius was set to be $1.1Ma$. The reason that the back mirror is a little larger than Ma is to duplicate the assumption of an infinitely sized back mirror for Siegman's Prony Method.

The survival factors of the resonator modes as a function of equivalent Fresnel number are displayed in figure 36. The results demonstrate the relationship of mode crossover occurring at integer equivalent Fresnel numbers. The least-loss laser cavity modes experienced the least loss for cavity geometries corresponding to half integer equivalent numbers. Compared to the results originally presented by Siegman[27], the curves presented in figure 36 have much more structure then their counterparts, but are more reminiscent of later results[24].

Shrinking the back mirror to be Ma, the eigenvalues are modified as shown in figure 37. The difference between the survival factors in figure 37 and figure 36 are recognized to be the diffractive losses of the back mirror. As Siegman noted in *Lasers*[24], diffractive losses have a larger impact on the unstable resonator compared to the stable resonator leading to the differences in the magnitude of the eigenvalues calculated for the cavity being large.

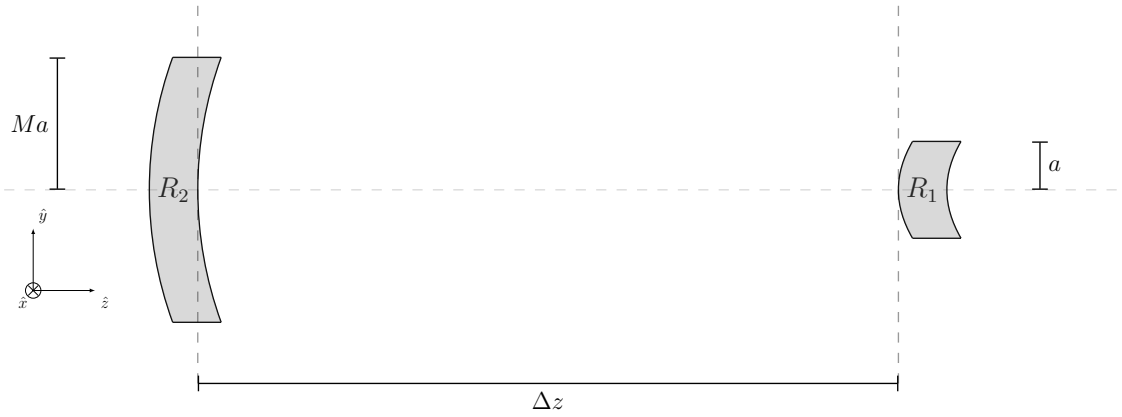

Figure 35. The geometry of used for the eigenvalue study as a function of $N_{\mathbf{Eq}}$. M was held at 2 throughout the eigenvalue study.

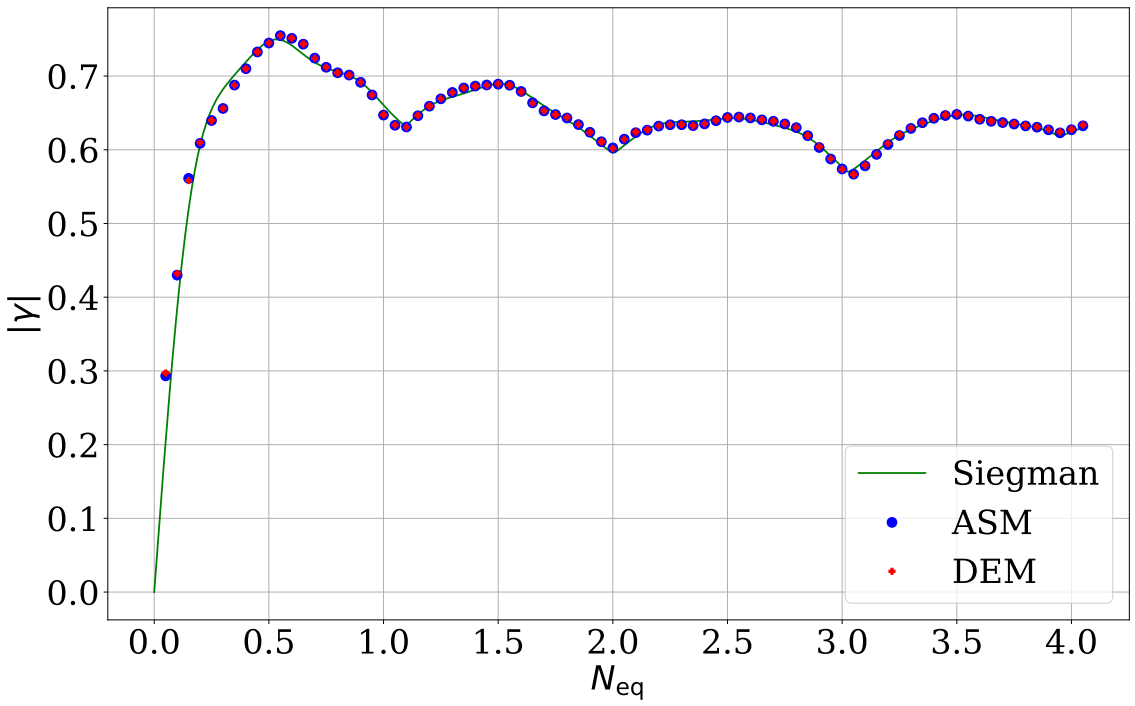

Figure 36. The absolute value of the eigenvalue associated with the per pass field propagation through the laser cavity as a function of the cavity equivalent Fresnel number. The eigenvalues are for a cavity with a back mirror 10% larger than Ma. The eigenvalues were calculated with Siegman's DEM covered in , the two-dimensional DEM, and Fox and Li iteration.

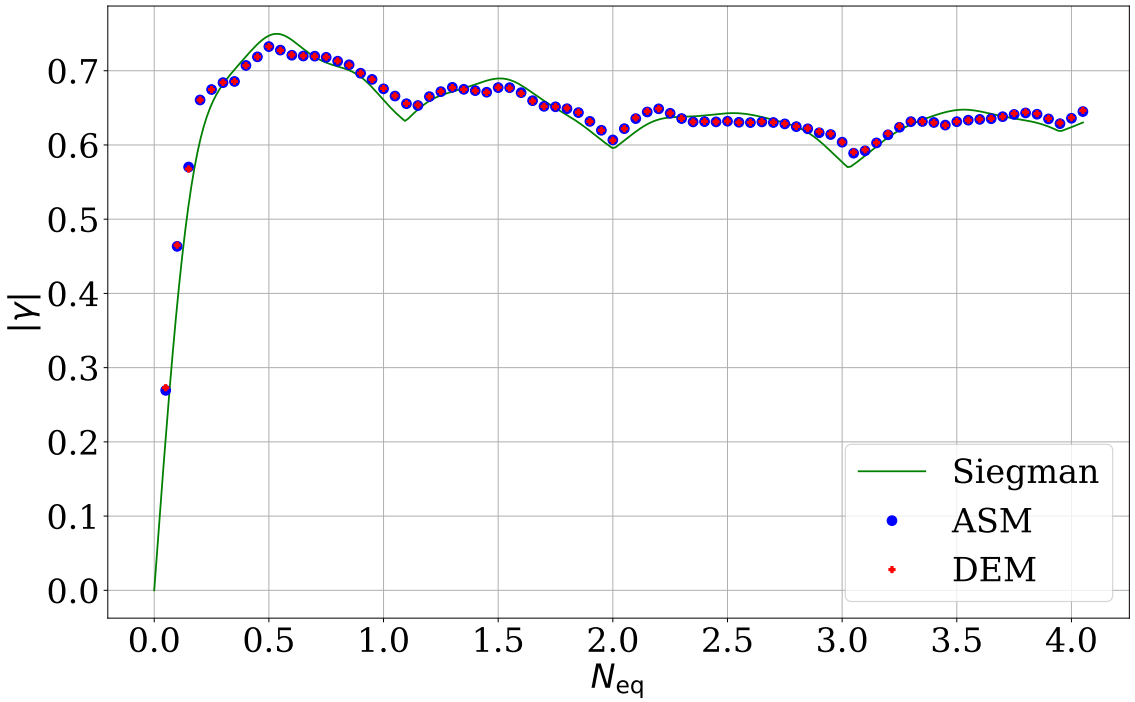

Figure 37. The absolute value of the eigenvalue associated with the per pass field propagation through the laser cavity as a function of the cavity equivalent Fresnel number. The eigenvalues are for a cavity with a back mirror equal to Ma. The eigenvalues were calculated with Siegman's DEM, the two-dimensional DEM, and Fox and Li iteration.

IV. Gain in the Cavity

Although analyzing the modes of a bare cavity provide insight into the unstable resonator, an important aspect of laser design to understand how the cavity mode couples into the gain of a laser system. In the following sections, this coupling is analyzed using a gain wave-optic simulation. The first section derives and defines the simulation techniques used to handle the field propagation through the gain medium. The simulation method will then be used to perform four separate studies involving the variation of cavity parameters from a defined baseline cavity arrangement and gain medium. In order to measure beam quality throughout the studies, VPIB, which is a measurement of beam quality comparing the cavity power output against an ideal Gaussian laser output is defined and used within all of the studies. In order have comparison for the calculated system efficiency, Hager's Model[10, 11] is presented. A new simplified model, which includes the effects of the unstable resonator mode is also presented, accounting for the differences between the results of the gain wave-optics simulation and the Hager model.

The Simulation of the Cavity

The inclusion of gain within the laser cavity requires a few additional calculation steps compared to the bare cavity simulations using Fox and Li Iteration. The principle of the simulation is the same, an initial field is propagated in the cavity for multiple passes until the difference in the volumetric laser, pump, and gain properties decreases to the order of machine precision. The simulation starts by defining two different grids, a gain grid and an optical grid. The gain grid is a subset of the optical grid possessing the same grid resolution as the optical grid, but having different grid extents, with the gain grid only extending to the axial extents of the gain cell, with

the optical grid extending across the entire laser resonator. As indicated in figure 38, the simulation involves the repetition of three primary steps, the pump propagation, updating the medium's gain and loss based upon the pump and laser intensity distribution within the cavity, and the laser propagation. The pump propagation consists of either a wave-optics or scaling code simulation of an input pump intensity distribution chosen by the researcher traveling in one way through the cavity. Updating the gain consists of calculating the gain for each grid position within the gain cell in order to appropriately handle the amplification to the laser and loss to the pump intensity distribution. Finally, the laser is then propagated using wave-optics forward and backward within the cavity, taking into account the mirror effects at each end of the cavity. The completion of all three steps indicate a pass of the laser and pump in the cavity. After many passes, the variation of the spatially dependent gain parameters as well as the spatial distribution of pump and laser intensity become negligible between successive passes of the calculation. When the variation becomes negligible, the system is said to have converged on the laser cavity solution.

The following subsections involve a derivation of the wave optics code for the propagation of the laser and pump followed by the calculation of the gain medium using a three energy level model.

The Wave-Optics Simulation.

One of the seminal texts regarding numerical propagation of a laser field through an interacting material is *Nonlinear Fiber Optics* by Agrawal[22]. In it, he defines the Fourier Split Step Method (FSSM) based upon the pulse propagation through fibers. The following subsection uses Agrawal's[22] and Siegman's[24] definitions to determine a wave equation for the propagation of an electromagnetic wave through material.

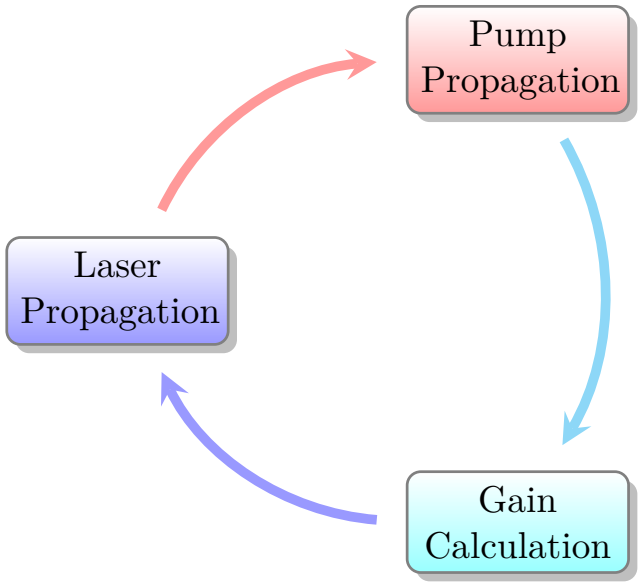

Figure 38. The sequence of events in a single pass for the simulation.

The wave propagation through material may be derived by starting with Maxwell's Equations for materials,

$$\boldsymbol{\nabla} \times \vec{\mathbf{E}} = -\frac{\partial \vec{\mathbf{B}}}{\partial t}\,, \tag{201}$$

$$\boldsymbol{\nabla} \times \vec{\mathbf{H}} = \vec{\mathbf{J}} + \frac{\partial \vec{\mathbf{D}}}{\partial t}\,, \tag{202}$$

$$\boldsymbol{\nabla} \cdot \vec{\mathbf{D}} = \rho_{\text{free}}\,, \tag{203}$$

$$\boldsymbol{\nabla} \cdot \vec{\mathbf{B}} = 0\,, \tag{204}$$

where $\vec{\mathbf{D}}$ and $\vec{\mathbf{H}}$ are the respective electric and magnetic fields that deal with free charge and current, $\vec{\mathbf{E}}$ and $\vec{\mathbf{B}}$ are the electric and magnetic fields, and ρ_{free} is the free charge. $\vec{\mathbf{E}}$ and $\vec{\mathbf{B}}$ are related to $\vec{\mathbf{H}}$ and $\vec{\mathbf{D}}$ through the following relationships

$$\vec{\mathbf{D}} = \varepsilon \vec{\mathbf{E}} + \vec{\mathbf{P}}_A\,, \tag{205}$$

$$\vec{\mathbf{B}} = \mu_0 \vec{\mathbf{H}} + \vec{\mathbf{M}}\,. \tag{206}$$

The term $\vec{\mathbf{P}}_A$, in equation (205), is a special notation indicating that the polarization of the atomic line transition of the laser media will be the only polarization present within the system. All other material effects are assumed to be included within the ε term, including the field effects of the dielectric outside of the atomic line transition of the laser medium. Essentially the linear effects on the electric field have been separated from the nonlinear effects.

The magnetic field associated with bound current $\vec{\mathbf{M}}$ will be assumed to be zero, with the magnetic field traveling as if it were in free space. $\vec{\mathbf{B}}$ is then only related to $\vec{\mathbf{H}}$ by the permeability of the magnetic field within a vacuum, μ_0.

Combining equations (201), (202), (203), and (204) gives a partial differential equation for the electric field

$$\boldsymbol{\nabla} \times \boldsymbol{\nabla} \times \vec{\mathbf{E}} = -\mu_0 \frac{\partial \vec{\mathbf{J}}}{\partial t} - \frac{n_{\text{ind}}^2}{c^2} \frac{\partial^2 \vec{\mathbf{E}}}{\partial t^2} - \mu_0 \frac{\partial^2 \vec{\mathbf{P}}'_A}{\partial t^2}\,, \tag{207}$$

where $\mu_0 \varepsilon = n^2/c^2$, and c is the speed of light in vacuum along with n representing the index of refraction of the material in which the wave is propagated. If the free current is considered to be a linear function of $\vec{\mathbf{E}}$

$$\vec{\mathbf{J}} = \sigma \vec{\mathbf{E}}\,, \tag{208}$$

the free charge in the system decreases exponentially

$$\frac{\partial \rho_f}{\partial t} = -\sigma \boldsymbol{\nabla} \cdot \vec{\mathbf{E}}\,, \tag{209}$$

$$\frac{\partial \rho_f}{\partial t} = -\frac{\sigma}{\epsilon} \rho_f\,, \tag{210}$$

$$\rho_f(t) = \rho_{f,0} e^{-\frac{\sigma}{\epsilon} t}\,. \tag{211}$$

If σ is large $\rho_f(t) \approx 0$, $\boldsymbol{\nabla} \cdot D = 0$, allowing for the entire wave equation to be written as

$$\nabla^2 \vec{\mathbf{E}} - \mu_0 \sigma \frac{\partial \vec{\mathbf{E}}}{\partial t} - \frac{n^2}{c^2} \frac{\partial^2 \vec{\mathbf{E}}}{\partial t^2} - \mu_0 \frac{\partial^2 \vec{\mathbf{P}}_A}{\partial t^2} = 0 \,. \tag{212}$$

where $\vec{\mathbf{P}}'_A$ is the polarization that effects growth and decay in the field. $\vec{\mathbf{P}}'_A$ may be calculated by recognizing that the entire polarization, $\vec{\mathbf{P}}_A$, is coupled to the optical field traveling within the medium

$$\frac{\partial^2 \vec{\mathbf{P}}_A}{\partial t^2} + \Delta\omega_A \frac{\partial \vec{\mathbf{P}}_A}{\partial t} + \omega_a^2 \vec{\mathbf{P}}_A = \kappa' \vec{\mathbf{E}} \,, \tag{213}$$

where κ' is the number of total dipole oscillations associated with the bound field

$$\kappa' = \frac{N q_e^2}{m\varepsilon} \,. \tag{214}$$

Equation (213) may be recast in Fourier space and then solved to be

$$\tilde{P}_A = \frac{\kappa'}{i\Delta\omega_A \omega + (\omega_a^2 - \omega^2)} \tilde{E} \,. \tag{215}$$

Assuming $\omega_a \approx \omega$ reduces equation (215) to

$$\tilde{P}_A = -i \frac{\kappa'}{\Delta\omega_A \omega} \frac{1}{1 + 2i \frac{(\omega - \omega_a)}{\Delta\omega_A}} \varepsilon \tilde{E} \,. \tag{216}$$

Splitting the relationship for the polarization, $\tilde{P}_A$ into real and imaginary parts gives

$$\tilde{P}_A = -\frac{\kappa' \tilde{E}}{\Delta\omega_A \omega_A} \left[\frac{\left(\frac{2(\omega - \omega_a)}{\Delta\omega_A} \right)}{1 + \left(\frac{2(\omega - \omega_a)}{\Delta\omega_A} \right)^2} + i \frac{1}{1 + \left(\frac{2(\omega - \omega_a)}{\Delta\omega_A} \right)^2} \right] . \tag{217}$$

Equation (217) contains the complete effects of the polarization generated by the medium. The real term corresponds to phase changes induced by the medium and

the imaginary term represents the growth or decay terms[42] that will effect the electric field in equation (212), and therefore

$$\tilde{P}'_A = -\frac{\kappa'\tilde{E}}{\Delta\omega_A\omega_A}\left[\frac{1}{1+\left(\frac{2(\omega-\omega_a)}{\Delta\omega_A}\right)^2}\right]. \tag{218}$$

At this point, the definition for $\frac{\kappa'}{\Delta\omega_A\omega_A}$ may be rewritten as a function of κ and γ_{rad}

$$\frac{\kappa'}{\Delta\omega_A\omega_A} = N\kappa\,, \tag{219}$$

where

$$\kappa = \frac{3^\star\lambda_A^3\gamma_{\text{rad}}}{4\pi^2\Delta\omega_A}\,, \tag{220}$$

$$\gamma_{\text{rad}} = \frac{q_e^2\omega^2 n^3}{3^\star\ 2\pi\varepsilon mc^3}\,, \tag{221}$$

where the $3^\star$ is either 3 for a material made up of fully aligned atoms or 1 for a material made up of randomly aligned atoms. Normally γ_{rad}, is determined experimentally[24] for a system. Equation (218) is then a function of

$$\tilde{P}_A = -i\kappa\Delta n\varepsilon\tilde{E}\frac{1}{1+\left(\frac{2(\omega-\omega_a)}{\Delta\omega_A}\right)^2}\,. \tag{222}$$

Using equation (222) in (212) and then applying a temporal Fourier transform gives

$$\nabla^2\tilde{E} - i\mu_0\sigma\omega\tilde{E} + \frac{\omega^2 n^2}{c^2}\tilde{E} + i\mu_0\omega^2\kappa\Delta n\varepsilon\tilde{E}\frac{1}{1+\left(\frac{2(\omega-\omega_a)}{\Delta\omega_A}\right)^2} = 0\,. \tag{223}$$

Assuming no conduction within the system, $\sigma = 0$, equation (223) becomes a new Helmholtz wave equation, one which includes the effects of the laser medium,

$$0 = \nabla^2 \tilde{E} + k^2 \left[1 + i \frac{1}{k} \sigma(\nu) \Delta n \right] \tilde{E} \,, \tag{224}$$

where $\sigma(\nu)$ is the cross section of interaction between the field and the medium. Based upon equations (224) and (223), $\sigma(\nu)$ is defined as

$$\sigma(\nu) = \frac{c^2 \gamma_{\text{rad}}}{8\pi n^2 \nu_A^2} \frac{1}{2\pi} \frac{\Delta\nu_A}{\left(\frac{\Delta\nu_A}{2}\right)^2 + (\nu - \nu_A)^2} \,, \tag{225}$$

where ν_A is the line center frequency of the material, $\Delta\nu_A$ is the linewidth associated with the medium, and k is the angular spatial frequency of the radiation in the material.

Solving the Partial Differential Equation (PDE) - Split Step.

Equation (224) is the PDE which represents the field of optical radiation going through the gain medium. However, as completed previously in chapter II, the PDE may be simplified with the paraxial wave assumption. Replacing $\tilde{E}$ with a more general wave function, ψ, gives a general wave equation for all scalar field components

$$\frac{\partial^2 \psi}{\partial z^2} = -\nabla_T^2 \psi - k^2 \left[1 + i \frac{1}{k} g_{ij}(x, y, z) \right] \psi \,, \tag{226}$$

where $\sigma(\nu)\Delta n$ has been rewritten as a function of gain, g_{ij}, associated with the transition $i \to j$,

$$g_{ij}(x, y, z) = \sigma(\nu) \Delta n \,. \tag{227}$$

Much as in chapter II, ψ is rewritten as a function of the freespace spatial angular frequency effects and an envelope function

$$\psi(x,y,z) = e^{ik_0 z}U(x,y,z)\,, \tag{228}$$

where k_0 is the angular spatial frequency of the oscillating electric field.

The definition of the envelope function allows for the left-hand side of equation (226) to be rewritten as

$$\frac{\partial^2 e^{ik_0 z}U}{\partial z^2} = \left(-k_0^2 U + 2ik_0\frac{\partial U}{\partial z} + \frac{\partial^2 U}{\partial z^2}\right)e^{ik_0 z}\,, \tag{229}$$

and with the paraxial assumption,

$$\left|2ik_0\frac{\partial U}{\partial z}\right| \gg \left|\frac{\partial^2 U}{\partial z^2}\right|, \tag{230}$$

becomes,

$$\frac{\partial^2 e^{ik_0 z}U}{\partial z^2} \approx \left(-k_0^2 U + 2ik_0\frac{\partial U}{\partial z}\right)e^{ik_0 z}\,. \tag{231}$$

Applying this relationship to equation (229) leads to

$$\frac{\partial U}{\partial z} = \frac{i}{2k_0}\nabla_T^2 U + \frac{ik_0}{2}\left(\frac{k^2}{k_0^2} - 1\right)U + \frac{k}{2k_0}g_{ij}(x,y,z)U\,, \tag{232}$$

and recognizing the index of refraction as

$$n_{\text{ind}} = \frac{k}{k_0}\,, \tag{233}$$

allows equation (232) to be written as

$$\frac{\partial U}{\partial z} = \frac{i}{2k_0}\nabla_T^2 U + \frac{ik_0}{2}\left(n_{\text{ind}}^2 - 1\right)U + \frac{n_{\text{ind}}}{2}g_{ij}(x,y,z)U\,. \tag{234}$$

Finally, if the material has an index of refraction which is approximately one, which is the case for most gases, equation (234) may be approximated to be

$$\frac{\partial U}{\partial z} = \frac{i}{2k_0}\nabla_T^2 U + ik_0(n_{\text{ind}} - 1)U + \frac{1}{2}g_{ij}(x, y, z)U \,. \tag{235}$$

$\frac{\partial U}{\partial z}$ and $\frac{i}{2k_0}\nabla_T^2 U$ in equation (235) represent the wave propagation terms of the PDE. These propagation terms remain the same in a vacuum as well as in a material. The $k_0(n_{\text{ind}} - 1)$ term are the effects of the medium on the phase of the propagating optical radiation. Finally, $\frac{1}{2}g_{ij}(x, y, z)$ represents the effects of the medium on the propagating radiation's amplitude. Equation (235) is a parabolic PDE, which means that it may be solved only by defining boundaries in the transverse direction and an initial value in the axial direction. Equation (235) must be modified to propagate a field defined at an initial point, U_0 a distance Δz.

The Fourier Split Step Method.

Equation (235) may be rewritten in terms of two operators

$$\frac{\partial U}{\partial z} = [\mathbf{L} + \mathbf{N}]U \,, \tag{236}$$

where the operators are defined as

$$\mathbf{L} = i\frac{1}{2k_0}\nabla_T^2 \,, \tag{237}$$

$$\mathbf{N} = ik_0(n_{\text{ind}}(x, y, z) - 1) + \frac{1}{2}n_{\text{ind}}(x, y, z)g_{ij}(x, y, z) \,. \tag{238}$$

Equation (236) represents a first order ODE, which may be generally solved to propagate the envelope function, U, exactly by

$$U(x, y, z + \Delta z) = e^{\int_z^{z+\Delta z} [\mathbf{L}+\mathbf{N}]\mathrm{d}z} U(x, y, z)\,, \tag{239}$$

where $\mathbf{N}$ may be assumed to vary little across small steps of Δz. The assumption of small variation allows equation (239) to be rewritten as

$$U(x, y, z + \Delta z) = e^{\Delta z \mathbf{L}} e^{\Delta z \mathbf{N}} U(x, y, z)\,, \tag{240}$$

Ignoring $\mathbf{L}$, the effects of $\mathbf{N}$ may be applied as a scalar multiplication on $\mathbf{U}$,

$$U(x, y, z + \Delta z) = e^{\mathbf{N}\Delta z} U(x', y', z)\,. \tag{241}$$

If the $\mathbf{N}$ operator is ignored, equation (240) may be solved in the spatial frequency regime,

$$U(x, y, z + \Delta z) = \mathscr{F}^{-1}\left[e^{\mathscr{F}[\mathbf{L}]\Delta z} \mathscr{F}[U]\right]. \tag{242}$$

Combining both of the solutions together allows for a complete propagation of the envelope function, U,

$$U(x, y, z + \Delta z) = \mathscr{F}^{-1}\left[e^{\mathscr{F}[\mathbf{L}]\Delta z} \mathscr{F}\left[e^{\mathbf{N}\Delta z} U(x, y, z)\right]\right]. \tag{243}$$

However, the entire solution written in equation (243) is not a completely accurate solution to equation (236). The inaccuracy of this solution is due to the nonequivalence between equation (239) and equation (240), namely,

$$e^{[\mathbf{L}+\mathbf{N}]} \neq e^{\mathbf{L}} e^{\mathbf{N}}\,. \tag{244}$$

The nonequivalence in equation (244) stems from the fact that the operators $\mathbf{L}$ and $\mathbf{N}$ do not commute. By the Baker-Hausdorff formula, the actual multiplication of the two exponential terms described in (240) are

$$e^{\mathbf{L}\Delta z}e^{\mathbf{N}\Delta z} = e^{\Delta z\mathbf{L}+\Delta z\mathbf{N}+\frac{1}{2}\Delta z^2[\mathbf{L},\mathbf{N}]+\frac{1}{12}[\mathbf{L}-\mathbf{N},[\mathbf{L},\mathbf{N}]]\Delta z^3+\ldots}, \tag{245}$$

where the commutation operation is defined as

$$[\mathbf{a},\mathbf{b}] = \mathbf{ab}-\mathbf{ba}\,. \tag{246}$$

Although the terms in the exponential are different, for small Δz, they are approximately the same. The error generated by the difference goes as the largest term in equation (245), $\frac{1}{2}[\mathbf{L},\mathbf{N}]\Delta z^2$. As has been previously indicated in the literature[22], modifying (243) to rewrite the exponentials as $e^{\frac{1}{2}\mathbf{N}\Delta z}e^{\mathbf{L}\Delta z}e^{\frac{1}{2}\mathbf{N}\Delta z}$ removes the $\frac{1}{2}[\mathbf{L},\mathbf{N}]\Delta z^2$ error term. Therefore, this research used

$$U(x,y,z+\Delta z) = e^{\frac{\mathbf{N}}{2}\Delta z}\mathscr{F}^{-1}\left[e^{\mathscr{F}[\mathbf{L}]\Delta z}\mathscr{F}\left[e^{\frac{\mathbf{N}}{2}\Delta z}U(x,y,z)\right]\right]. \tag{247}$$

instead of equation (243) to minimize the step error in the method to $\mathcal{O}(\Delta z^3)$. When writing out the operators associated with the propagation, the $\mathbf{L}$ term is recognized as the propagator from the ASM

$$e^{\mathscr{F}[\mathbf{L}]\Delta z} = e^{i\frac{\Delta z}{2k}\left[k_x^2+k_y^2\right]}. \tag{248}$$

Equation (247) and the definitions in equations (237) and (238) allow for the propagation in a gain medium across a step size of Δz to be modeled with

$$\mathscr{P}_{\mathrm{G}}[U] = e^{\frac{1}{2}ik_0(n_{\mathrm{ind}}-1)\Delta z} e^{\frac{1}{4}n_{\mathrm{ind}}g_{ij}\Delta z} \mathscr{F}^{-1}\left[e^{i\frac{\Delta z}{2k_0}\left[k_x^2+k_y^2\right]} \mathscr{F}\left[e^{\frac{1}{2}ik_0(n_{\mathrm{ind}}-1)\Delta z} e^{\frac{1}{4}n_{\mathrm{ind}}g_{ij}\Delta z} U\right]\right]. \tag{249}$$

Equation (249) defines the Fourier Split-Step Method that was used for research involving the propagation through a gain medium. It is important to note that if the gain term is zero, the amplitude of U will not be modified during transit. If in addition to the gain being zero, the index of refraction is one, then equation (249) reduces to ASM. Unless performed for multiple different frequencies, FSSM only propagates a monochromatic beam. Due to the computational difficulty associated with multiple propagations, the laser in this research was assumed to be monochromatic. Due to the higher error terms in the propagation through the gain, many successive steps were taken through the gain medium, as shown in figure 39. The oneway propagation in each direction involved propagating the field from the mirror to the gain cell followed by multiple steps within the gain medium and then a propagation from the gain cell to the mirror. For all simulations within this research, the gain cell propagation involved 200 steps within the gain medium. Therefore, the full propagation in a single direction within the laser cavity was a combination of no gain and gain propagations

$$\mathscr{P}[U] = \mathscr{P}_{\mathrm{NG}} \mathscr{P}_{\mathrm{G}}^{N_{\mathrm{Steps}}} \mathscr{P}_{\mathrm{NG}}[U]. \tag{250}$$

The single pass for the wave-optic propagation is the same as in equation (59), with the propagation term now made up of gain propagation terms for propagation in the laser medium and non-gain propagation terms for propagation from the medium to the mirrors.

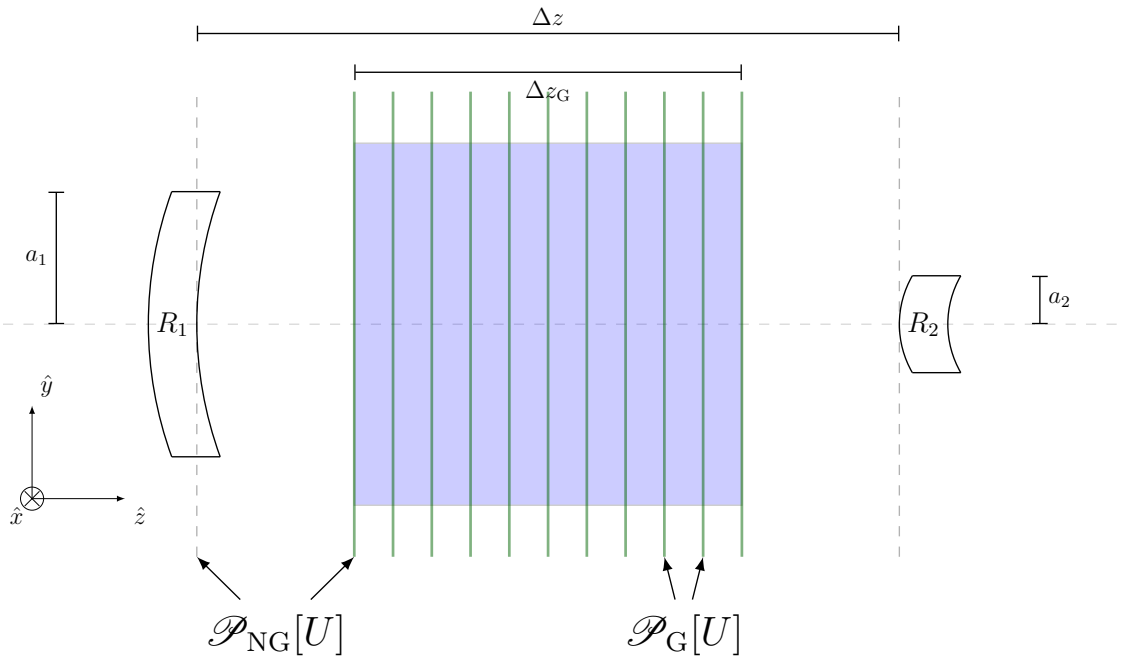

Figure 39. The steps taken in the propagation of the envelope function throughout the cavity, notice that inside the gain, the field was propagated with FSSM. Outside the gain the field was propagated with ASM.

Scaling for Simplified Propagation.

Dependent on the cavity layout and beam parameters, characterizing causes of loss and mode shape within the gain medium can become overly complex. In order to simplify the simulation and properly attribute cavity behavior to the effects of the unstable resonator mode, the pump was not propagated using the wave-optics methods defined above. Instead the assumption of a uniform scaled pump was used for the system. The propagation within the gain medium for pump was then modified to be

$$\mathscr{P}_{\mathrm{G}}[U(x,y)] = e^{ik_0(n_{\mathrm{ind}}-1)\Delta z} e^{\frac{1}{2}n_{\mathrm{ind}}g_{ij}\Delta z}[U(x,y)]\,. \tag{251}$$

Such an approximation is valid if

$$\frac{1}{2k_0}\left|\nabla_T^2 U\right| \ll \sqrt{(n_{\mathrm{ind}}-1)^2 + \frac{1}{4}g_{ij}^2}\,|U|\,. \tag{252}$$

The approximation is valid for the uniform pump configuration used for the studies presented in this research. For future work involving more complex pump variations, the pump wave-optics may need to be included in simulation.

Determining the Gain.

The goal of the research was to understand the workings of an unstable laser resonator in the presence of a high gain medium. As discussed in chapter I, DPAL is an interesting high gain system that is of great interest to the Department of Defense (DoD). Therefore, the gain medium that will be used within the simulations within this research will be an optically pumped alkali material. Based upon previous work performed by Hager[10, 11], the alkali material investigated was rubidium with helium used as a buffer gas. Figure 40 is the Grotian diagram for rubidium, showing the energy levels that will be used for pumping and lasing within the simulation. For the simulations performed in this research, the only energy levels used for the kinetics will be the levels related to the pump and lasing transitions.

The Three-Level Kinetics of the Systems.

The three-level model for the rubidium-helium mixture is illustrated in figure 41 where the three levels are defined by the $5^2P_{3/2}$, $5^2P_{1/2}$, and $5^2S_{1/2}$. The primary lasing series occurs with rubidium optically absorbing radiation on the pump line exciting atoms from the $5^2S_{1/2} \rightarrow 5^2P_{3/2}$ state, followed by a collision with the helium buffer gas de-exciting rubidium atoms from the $5^2P_{3/2} \rightarrow 5^2P_{1/2}$ state, and lasing dexciting rubidium atomr from the $5^2P_{1/2} \rightarrow 5^2S_{1/2}$ state. From this relationship and the natural relaxation of the two excited modes, the following system of rate equations

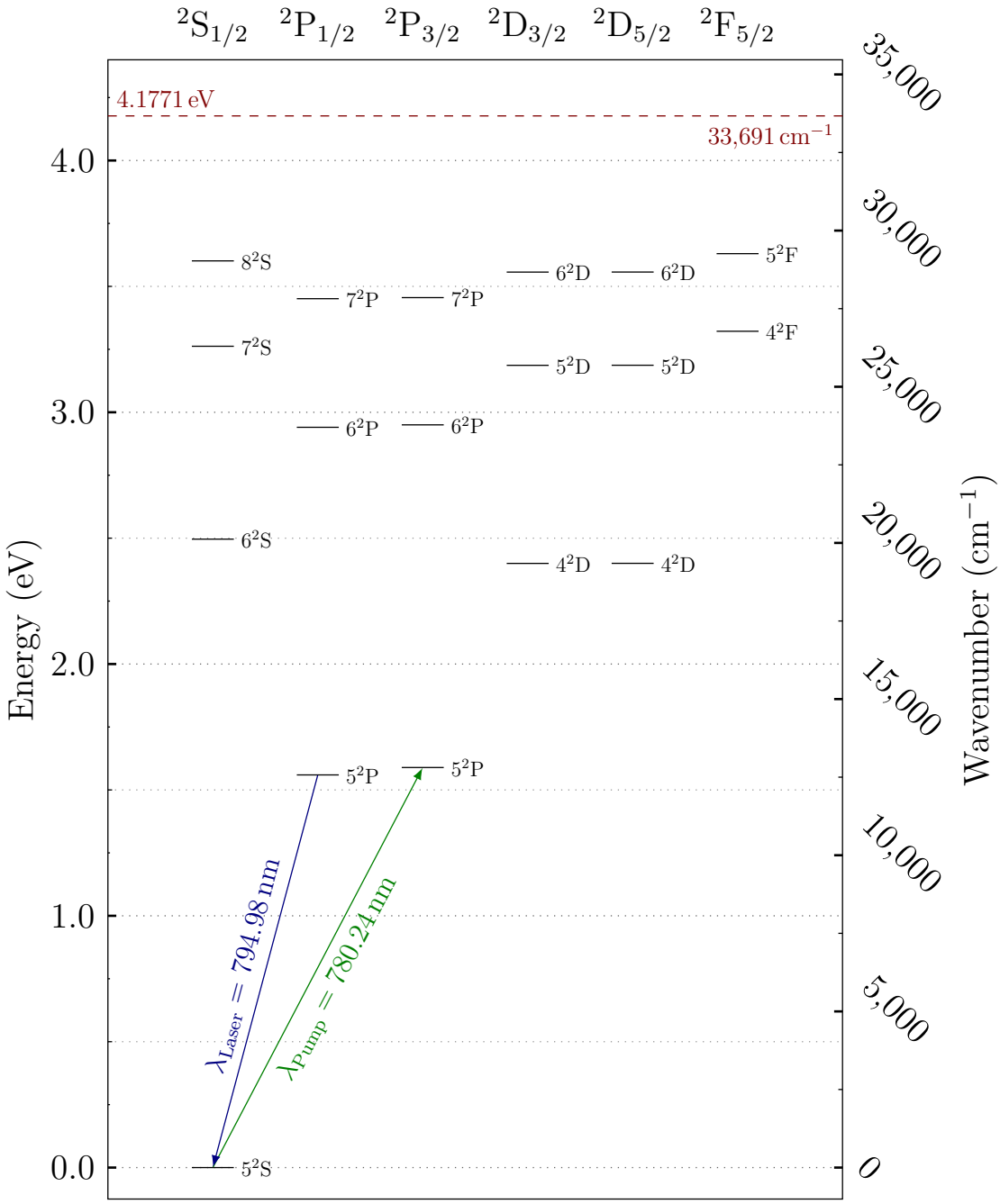

Figure 40. The Grotian diagram for rubidium created using data from the National Institute of Standards and Technology (NIST) Atomic Spectra Database[43]. The pump transition, $5^2S_{1/2} \rightarrow 5^2P_{3/2}$, of the DPAL is shown in green. The lasing transition, $5^2P_{1/2} \rightarrow 5^2S_{1/2}$, is shown in blue.

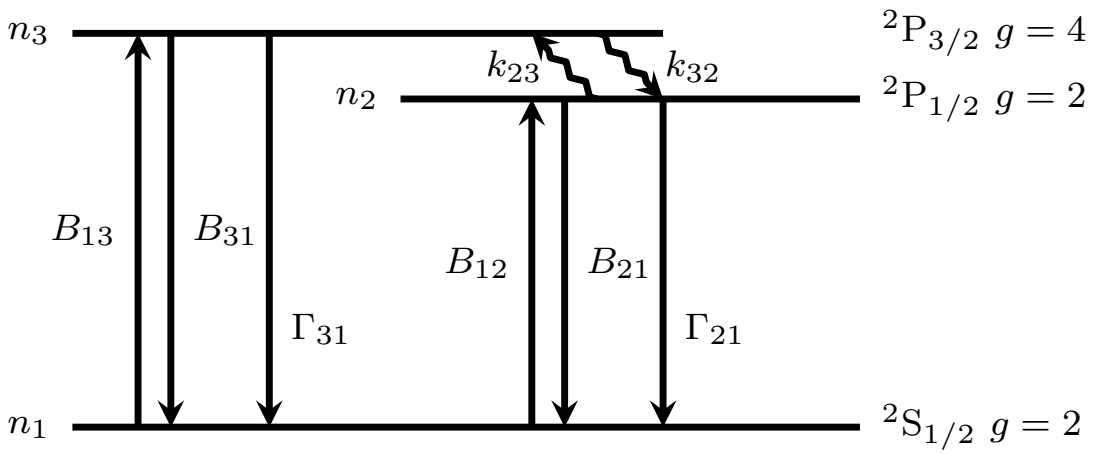

Figure 41. Three-level kinetic model of the rubidium gain medium.

may be defined as

$$\frac{\mathrm{d}n_1}{\mathrm{d}t} = B_{31}n_3 - B_{13}n_1 + B_{21}n_2 - B_{12}n_1 + \Gamma_{31}n_3 + \Gamma_{21}n_2\,, \tag{253}$$

$$\frac{\mathrm{d}n_2}{\mathrm{d}t} = -B_{21}n_2 + B_{12}n_1 - \Gamma_{21}n_2 + k_{32}n_{\mathrm{mix}}n_3 - k_{23}n_{\mathrm{mix}}n_2\,, \tag{254}$$

$$\frac{\mathrm{d}n_3}{\mathrm{d}t} = -B_{31}n_3 + B_{13}n_1 - \Gamma_{31}n_3 - k_{32}n_{\mathrm{mix}}n_3 + k_{23}n_{\mathrm{mix}}n_2\,. \tag{255}$$

where B_{ij} represents the optical transition rates from level $i \to j$, n_i is the number density for level i, k_{ij} are the collisional transfer rate between fine structure states from $i \to j$, n_{mix} is the number density of the buffer gas, and Γ_{ij} are the natural dexcitations to the ground state. Some of these parameters are recognized to be related to one another due to conservation of number density and photon energy at chemical equilibrium,

$$B_{13} = 2B_{31}\,, \tag{256}$$

$$k_{23} = 2e^{-\theta}k_{32}\,, \tag{257}$$

where θ is $\frac{\Delta E}{k_\mathrm{b} T}$, T is the temperature of the gain medium, k_b is Boltzmann's constant, and ΔE is the energy difference between the fine structure mixing levels. The B_{ij} rate is recognized to be a function of the photon density and the cross section of interaction of those photons the gain media, σ_{21} and σ_{31}, allowing for the definition of the optical transition rates as

$$B_{21} = \sigma_{21} \frac{\Psi}{h_\mathrm{p} \nu_\mathrm{l}} \,, \tag{258}$$

$$B_{31} = \sigma_{31} \frac{\Omega}{h_\mathrm{p} \nu_\mathrm{p}} \,. \tag{259}$$

where Ψ is the two-way intensity of the laser radiation, Ω is the two-way intensity of the pump radiation, σ_{ij} are the cross sections of the photon atom interaction, ν_l is the optical frequency of the laser, ν_p is the optical frequency of the pump, and h_p is Planck's Constant. k_{32} is recognized as the rate of reaction for the $n_3 \rightarrow n_1$ transition, and when combined with the helium density, n_He, becomes the fine structure mixing rate

$$\gamma_\mathrm{mix} = k_{32} n_\mathrm{He} \,. \tag{260}$$

The above definitions for the B_{ij} rates assume the laser and the pump are narrow-banded around the line center of the gain medium for both lasing and pump interactions. Using these definitions, equations (253), (254), and (255), may be rewritten as

$$\frac{\mathrm{d}n_1}{\mathrm{d}t} = \sigma_{31} \frac{\Omega}{h_\mathrm{p} \nu_\mathrm{p}} (n_3 - 2n_1) + \sigma_{21} \frac{\Psi}{h_\mathrm{p} \nu_\mathrm{l}} (n_2 - n_1) + \Gamma_{31} n_3 + \Gamma_{21} n_2 \,, \tag{261}$$

$$\frac{\mathrm{d}n_2}{\mathrm{d}t} = -\sigma_{21} \frac{\Psi}{h_\mathrm{p} \nu_\mathrm{l}} (n_2 - n_1) - \Gamma_{21} n_2 + \gamma_\mathrm{mix} \left(n_3 - 2e^{-\theta} n_2 \right) , \tag{262}$$

$$\frac{\mathrm{d}n_3}{\mathrm{d}t} = -\sigma_{31} \frac{\Omega}{h_\mathrm{p} \nu_\mathrm{p}} (n_3 - 2n_1) - \Gamma_{31} n_3 - \gamma_\mathrm{mix} \left(n_3 - 2e^{-\theta} n_2 \right) . \tag{263}$$

Many of the terms in equations (261), (262), and (263), need to be further defined in order for use in the simulation. For example, Γ_{21} and Γ_{31} are the dexcitation rates for the energy levels and are driven by spontaneous emission of photons and collisional dexcitation with an energy levels to the ground state. Therefore, the dexcitation rates are defined by

$$\Gamma_{21} = \frac{1}{\tau_{21}} + k_{21} n_{\mathrm{He}} \,, \tag{264}$$

$$\Gamma_{31} = \frac{1}{\tau_{31}} + k_{31} n_{\mathrm{He}} \,, \tag{265}$$

where τ_{ij} is the optical relaxation time for the transition of $i \rightarrow j$. The second term is the rate of collisional dexcitation to the ground state. Typically the rate of collisional dexcitation for these energy levels is very small compared to the relaxation time meaning the collisional dexcitation may be ignored for steady state DPAL operation[10].

The optical cross section, previously defined in equation (225) in terms of the a Lorentzian lineshape requiring the center-line frequency and the bandwidth of the line absorption. The centerline frequency is defined by

$$\nu_{ij} = \frac{\Delta E_{ij}}{h_{\mathrm{p}}} \,, \tag{266}$$

for which ΔE_{ij} is the difference in energy between both of the transition states which may be determined from figure 40. The absorption bandwidth, $\Delta\nu_{ij}$, is related to the relaxation time and the pressure broadening experienced in the material

$$\Delta\nu_{ij} = \frac{1}{2\pi\tau_{ij}} + \Gamma_{ij,T} P \,, \tag{267}$$

where P is the pressure of the system and $\Gamma_{ij,T}$ is the temperature dependent optical transfer rate, defined by

$$\Gamma_{ij,T} = \Gamma_{ij,T_{\rm ref}} \left(\frac{T}{T_{\rm ref}} \right)^{\xi_{ij}-\frac{1}{2}} , \tag{268}$$

where the $T_{\rm ref}$ is the reference temperature and ξ_{ij} is a fit of the temperature to temperature, T. $\Gamma_{ij,T_{\rm ref}}$ is defined by a measured cross section, measured at $T_{\rm ref}$

$$\Gamma_{ij,T_{\rm ref}} = \sigma_{ij,T_{\rm ref}} \sqrt{\frac{8}{\pi \mu k_{\rm b} T_{\rm ref}}} , \tag{269}$$

where μ is the reduced mass of collisions in the system, which for the mixture of rubidium and helium, is determined from the atomic mass of helium, $m_{\rm He}$, and rubidium, $m_{\rm Rb}$,

$$\mu = \frac{m_{\rm Rb} m_{\rm He}}{m_{\rm Rb} + m_{\rm He}} . \tag{270}$$

Another important rate to define is the collisional dexcitation rate, k_{32}, determined empirically by Gallagher in his 1968 paper[44]. The relationship for the rubidium mixture is defined as

$$k_{32} = v_{\rm rel} \left[k_{32,1} \Gamma(5) \left(\frac{2 k_{\rm B} T}{\mu v_{\rm ref}^2} \right)^3 + k_{32,2} \Gamma\left(\frac{5}{2} \right) \left(\frac{2 k_{\rm B} T}{\mu v_{\rm ref}^2} \right)^{1/2} \right] , \tag{271}$$

where $v_{\rm rel}$ is the relative speed given by

$$v_{\rm rel} = \sqrt{\frac{8 k_{\rm b} T}{\pi \mu}} . \tag{272}$$

An important modification to $\gamma_{\rm mix}$ was found by Sell[45], who discovered the importance of a constant 3-body collision term, k_{3b}, modifying $\gamma_{\rm mix}$ to be

$$\gamma_{\rm mix} = k_{32} n_{\rm mix} + k_{3b} n_{\rm mix}^2 . \tag{273}$$

Solving the Rate Equations.

The complete simulation, as indicated in figure 38, is ran until the cavity reaches a steady-state. The assumption of a steady-state solution to the gain wave-optics and the relatively high fine-structure mixing rates, $\gamma_{\text{mix}} \approx 0.1 - 2.0\,\text{ns}$, allow for equations (261), (262), and (263) to be solved by treating the system of differential equations as steady state,

$$\frac{\mathrm{d}n_1}{\mathrm{d}t} = \frac{\mathrm{d}n_2}{\mathrm{d}t} = \frac{\mathrm{d}n_3}{\mathrm{d}t} = 0\,. \tag{274}$$

The steady-state condition allows equations (261), (262) and (263) to be written as a linear system of equations,

$$0 = \sigma_{31}\frac{\Omega}{h_{\text{p}}\nu_{\text{p}}}(n_3 - 2n_1) + \sigma_{21}\frac{\Psi}{h_{\text{p}}\nu_{\text{l}}}(n_2 - n_1) + \Gamma_{31}n_3 + \Gamma_{21}n_2\,, \tag{275}$$

$$0 = -\sigma_{21}\frac{\Psi}{h_{\text{p}}\nu_{\text{l}}}(n_2 - n_1) - \Gamma_{21}n_2 + \gamma_{\text{mix}}\left(n_3 - 2e^{-\theta}n_2\right)\,, \tag{276}$$

$$0 = -\sigma_{31}\frac{\Omega}{h_{\text{p}}\nu_{\text{p}}}(n_3 - 2n_1) - \Gamma_{31}n_3 - \gamma_{\text{mix}}\left(n_3 - 2e^{-\theta}n_2\right)\,. \tag{277}$$

which when combined with a requirement that the density of all states must add up to the density of rubidium, n_{Rb},

$$n_{\text{Rb}} = n_1 + n_2 + n_3\,, \tag{278}$$

allowed for the calculation of n_1, n_2, and n_3 for the steady-state condition. The densities of atoms occupying each energy state may then be used to calculate the gain in the $2 \to 1$ and $3 \to 1$ transition lines,

$$g_{21} = \sigma_{21}(\nu_{21})(n_2 - n_1)\,, \tag{279}$$

$$g_{31} = \sigma_{31}(\nu_{31})(n_3 - 2n_1)\,. \tag{280}$$

These gains may then be used in the wave-optics calculation. The evaluation of the cross sections at line center indicates that the simulations conducted in this research were all performed at the narrowband limit.

The index of refraction used for the gain medium was calculated using the Gladstone-Dale coefficient for helium and the helium number density

$$n = 1 + \xi_{\mathrm{He}} m_{\mathrm{He}} n_{\mathrm{He}} \,, \tag{281}$$

where $\xi_{\mathrm{He}} = 3.49 \times 10^{-5} \frac{\mathrm{m}^3}{\mathrm{kg}}$ is the Gladstone-Dale coefficient[46] for helium and n_{He} is the helium number density, calculated from the system pressure and temperature using the ideal gas law,

$$n_{\mathrm{He}} = \frac{P_{\mathrm{He}}}{k_{\mathrm{b}} T} \,. \tag{282}$$

Baseline Case Simulation

When analyzing the mode of an unstable resonator in relation to a cavity there are many different parameters which may be varied. To facilitate the research concerning the gain medium, analysis will involve having a defined baseline case and modifying parameters singly away from the baseline case. Figure 42 and figure 43 define the parameters associated with the baseline case. There are a few differences between the baseline case for the cavity with gain, and the calculations in chapter III, primarily the inclusion of a gain medium that drives other considerations with the laser design. The lasing and pumping wavelength are much shorter for lasing in an alkali medium, whereas, the bare cavity simulations involved a lasing wavelength corresponding to a CO_2 laser, 10.6 μm in order to better compare to work previously performed. As observed from equation (151), decreasing the wavelength increases the Fresnel number

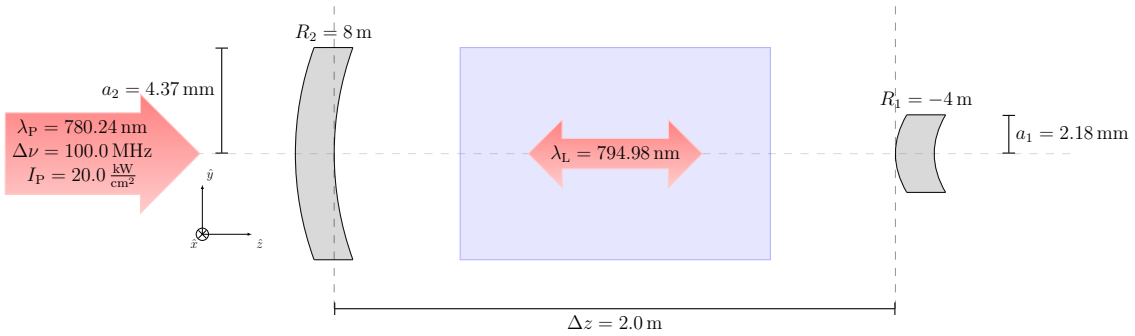

Figure 42. Diagram of the laser, pump, and lasing cavity parameters for the baseline case simulation.

associated with the cavity, also increasing the computational effort required to simulate the cavity. For this reason, the square cavity mirrors in figure 43 were chosen in order to enable the simulation of the higher Fresnel number cavity. The baseline case cavity dimensions were chosen to simulate a cavity with a geometric magnification of two and a Fresnel number of three. The mirrors were chosen to have an aspect ratio of $\frac{9}{10}$ to differentiate between the different modes in the transverse direction. The blue region in figure 42 and figure 43 represents the pumped gain region. Even though the pumped gain was chosen to only extend partially in the transverse directions, the gain grid was chosen to extend transversely over the complete optical grid.

The gain cell parameters and the pump intensity were chosen to ensure good laser operation and be a reasonable facsimile for a real system. However, the simulations do not include heating of the gain medium or fluid effects within the cavity. Pressure and temperature are defined quantities used to model the fine structure mixing and the pressure broadening associated with the rubidium alkali material and were not allowed to vary during the simulation. The simulations also did not include the effects of Amplified Spontaneous Emission (ASE) in the gain wave-optics simulation, which may impact the gain available for lasing in a real system.

The optical grid in the baseline case had a sampling of $N_x, N_y = 512, 512$, with a total grid size of $\Delta x_\mathrm{Grid}, \Delta y_\mathrm{Grid} = 5.09\,\mathrm{cm}, 5.09\,\mathrm{cm}$. The gain medium had a sampling

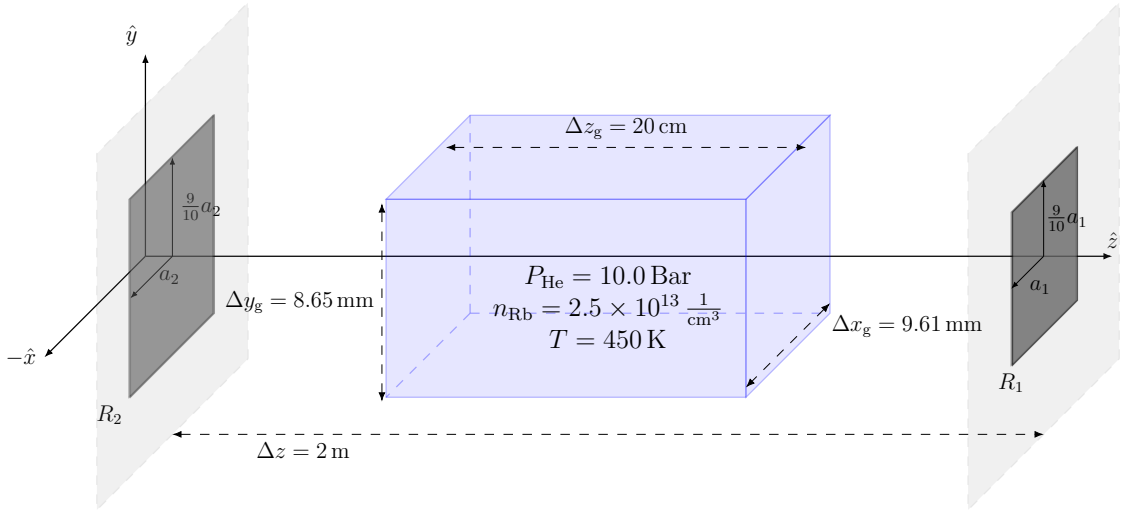

Figure 43. Diagram of the lasing medium parameters in the square mirror lasing cavity for the baseline case simulation.

of $N_z = 200$, with two more planes included for the optical grid to represent the mirror planes. Prior to the simulation with the gain medium, Fox and Li iteration was used to calculate the bare cavity mode of the laser resonator. The bare cavity output mode's phase and intensity are shown in figure 44. One may immediately recognize that an intuitive feel for the mode is almost nonexistent, which will remain consistent throughout the cavity analysis. The gain cavity simulation following all three of the cycles indicated in figure 38 was ran until simulation convergence occurs.

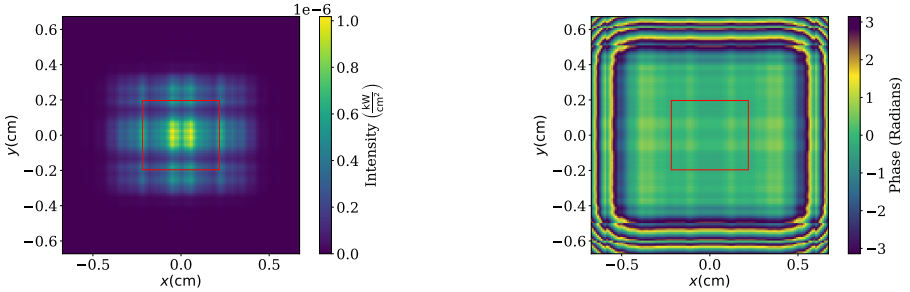

(a) Normalized Output Mode Intensity **(b) Output Mode Phase**

Figure 44. Contour plots of the output normalized intensity and phase for the baseline configuration located at the smaller outcoupling mirror. The red line indicates the edge of the outcoupling mirror, the transverse field in the red circle is not transmitted out of the cavity.

Convergence is defined as the point where enough simulation iterations have occurred for the residual for the laser, pump, gain populations, and pump have ceased changing. Residuals are the normalized difference in the sum of a field value between each step defined mathematically for a general parameter, u,

$$\Delta u^n = \frac{\sum_{i,j,k} \left| \left| u^n_{i,j,k} \right| - \left| u^{n-1}_{i,j,k} \right| \right|}{\sum_{i,j,k} \left| u^{n-1}_{i,j,k} \right|} , \tag{283}$$

where i, j, and k are the indices corresponding to the spatial grid and n is the simulation step, with each step corresponding to a simulated pass in the cavity. Figure 45 displays the residuals of the variables defined in table 1 as a function of simulation step. Throughout the simulation, n_1, n_2, and n_3 are calculated within figure 38, from these values the gain applied to the field,

$$\gamma = e^{\frac{1}{2} g_{21} \delta z + i(n_{\text{ind}} - 1)\delta z} , \tag{284}$$

where δz is the $\hat{z}$ resolution, defined by

$$\delta z = \frac{\Delta z_{\text{G}}}{N_z - 1} . \tag{285}$$

Residual of Cavity	**Variable of Residual (u)**
Population in the n_1 State	Δn_1
Population in the n_2 State	Δn_2
Population in the n_3 State	Δn_3
The attenuation of the pump	$\Delta \gamma_{\text{Pump}}$
The attenuation of the laser	$\Delta \gamma_{\text{Laser}}$
The pump field	ΔU_{Pump}
The laser field	ΔU_{Laser}

Table 1. The definition of the residuals calculated in a simulation and shown in figure 45.

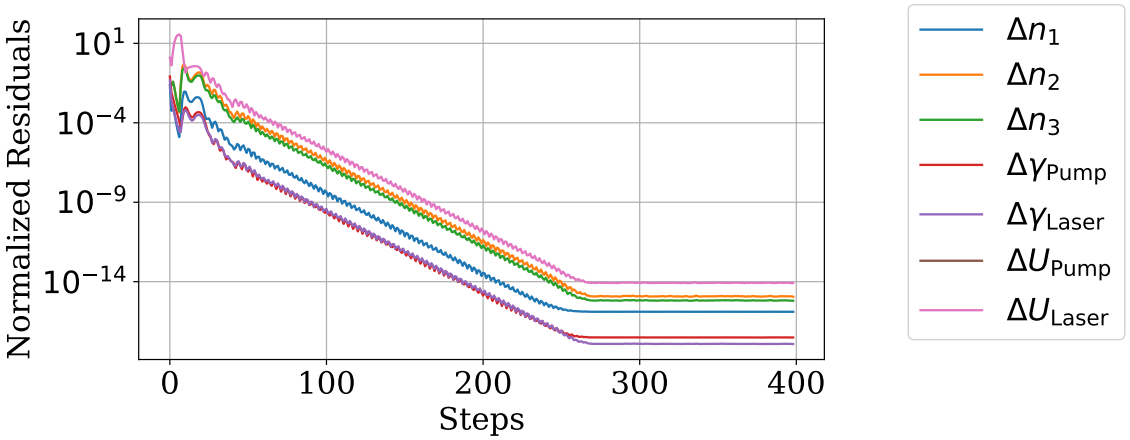

Figure 45. The normalized residuals as a function of simulation cycle through the cavity with each step corresponding to a full operation of simulation events pictured in figure 38.

Figure 46 indicates $|\gamma|$ is close to one indicating that the laser experiences a gain that is close to the gain threshold of the cavity system. The predicted gain threshold or the gain required to overcome cavity losses is geometric analysis is $g_{\text{th}} = 3.4657$ and the measured threshold of the cavity is $g_{\text{th}} = 3.6919$ indicating that there is more loss from the diffractive mode being propagated through the medium versus the the expected loss of the geometric mode. Another interesting feature of the gain medium is the presence of features outside the pumped laser medium, indicating that diffraction from the mirrors is actually moving laser energy outside of the pumped area. Outside of the pumped area, the gain is highly absorptive acting as a window for the laser beam. The field intensity in both directions were also calculated the side profile of the laser traveling in the $-\hat{z}$ and $+\hat{z}$ directions are shown in figure 47 and figure 48 respectively. Figure 47 shows the field spreading during travel across the gain, even though the length of the gain cell is shorter than travel across the entire cavity. Surprisingly, the mode in figure 48 also shows a slight growth to the laser mode, even though the beam is collimated in the geometric limit. Another feature in the laser comparing $-\hat{z}$ to $+\hat{z}$ travel is recognizing that the intensity in the $-\hat{z}$ direction reaches a larger

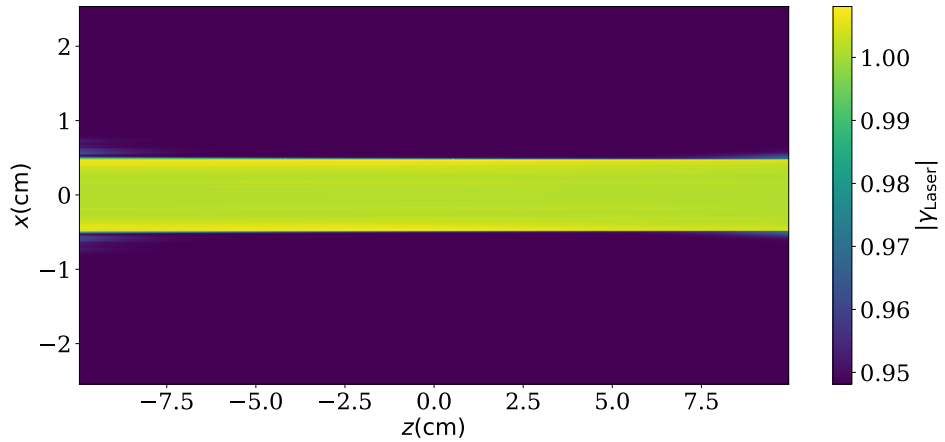

Figure 46. A xz slice along $y = 0$ of the amplitude of the gain profile for the baseline configuration, taking only within the gain cell.

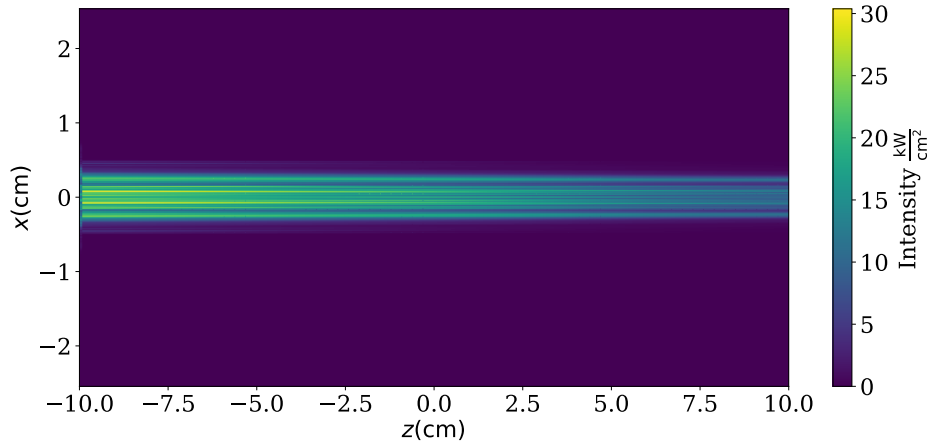

Figure 47. A xz slice along $y = 0$ of the laser intensity traveling in the $-\hat{z}$ direction for the baseline configuration, taking only within the gain cell.

intensity than the $+\hat{z}$ direction. Such differences in the intensity distribution may be explained by the intensity density in the transverse direction on average being less in the $-\hat{z}$ direction than in the $+\hat{z}$ direction. The difference in intensity distribution may be explained by understanding that the expanding $-\hat{z}$ beam is smaller than the $+\hat{z}$ in the transverse direction, consistent with the geometric picture of the positive branch confocal unstable resonator. A transverse xy slice of the $+\hat{z}$ field intensity and phase located at the outcoupling mirror is shown in figure 49. Immediately, one may recognize that the pictured intensity with the inclusion of gain in figure 49a does not match the normalized intensity calculated for the bare cavity mode in figure 44a. The differences are due to the presence of the gain medium, which has the effect of increasing the distribution of the mode intensity away from the axis of propagation. Such an effect may be attributed to the cavity interaction between the gain medium and laser field. Interestingly, the difference does not seem to be present in the phases pictured in figure 49b and figure 44b. Both show a similar distribution across the aperture exit and retain a relatively flat phase front indicating a collimated output from the cavity.

From the intensity at the outcoupling mirror, shown in figure 49, the farfield beam may be calculated by propagating the apodized outcoupled beam from the laser a distance of Δz to the farfield. By assuming a farfield distance,

$$\Delta z \gg \frac{k}{2}\left(x'^2 + y'^2\right), \tag{286}$$

the beam may be propagated through Fraunhofer diffraction[47], which is a modification of the Fresnel integral mentioned in equation (53) to

$$U(x, y, z + \Delta z) = \frac{ik}{2\pi z} e^{\frac{ik\left[x^2+y^2\right]}{2\Delta z}} \iint_{-\infty}^{\infty} e^{\frac{-ik[xx'+yy']}{\Delta z}} U(x', y', 0)\, \mathrm{d}x'\, \mathrm{d}y' \ . \tag{287}$$

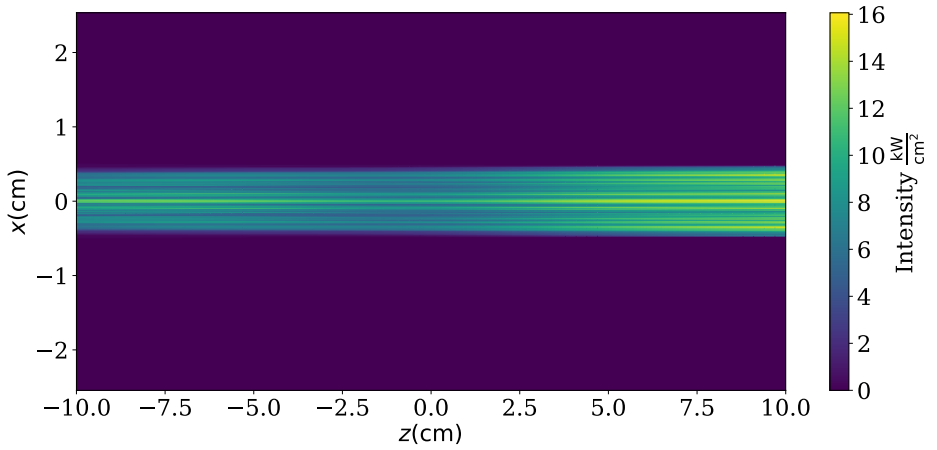

Figure 48. A xz slice along $y = 0$ of the laser intensity traveling in the $+\hat{z}$ direction for the baseline configuration, taking only within the gain cell.

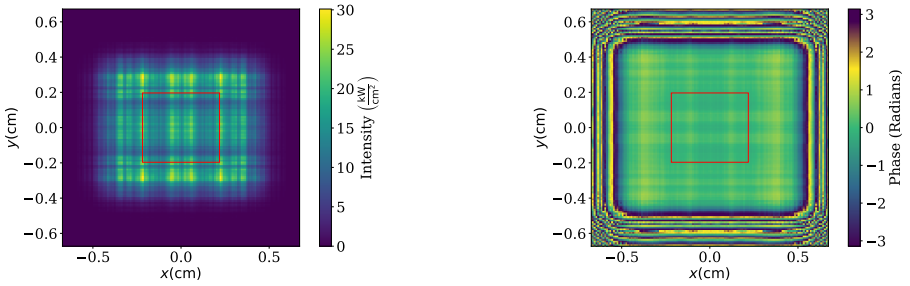

(a) Output Mode Intensity **(b) Output Mode Phase**

Figure 49. Contour plots of the output intensity and phase for the baseline configuration located at the smaller outcoupling mirror. The red line indicates the edge of the outcoupling mirror, the transverse field in the red circle is not transmitted out of the cavity.

Equation (287) be rewritten as a single Fourier transform from the spatial coordinates at x' and y' to "frequency space" coordinates which correspond to a transverse coordinates in the farfield defined by

$$k_x = \frac{kx}{\delta z}\,, \tag{288}$$

$$k_y = \frac{ky}{\delta z}\,. \tag{289}$$

The farfield beam located at a distance of $\Delta z = 10000\,\mathrm{m}$ is displayed in figure 50.

An immediate observation from the farfield is that the intensity striations shown in figure 49 have disappeared as the field has moved into the Fraunhoffer regime. A good question at this point is, "How much power is contained within a radius within the farfield?" In order to answer this question requires the definition of another quantity, the Vertical Power in the Bucket (VPIB).

Vertical Power in the Bucket (VPIB).

The VPIB is a comparison between the lowest-order Hermite Gaussian Mode based upon the laser aperture output[48] and the actual laser output in the farfield. The lowest order mode, based upon equation (153), at the location of the beam waist

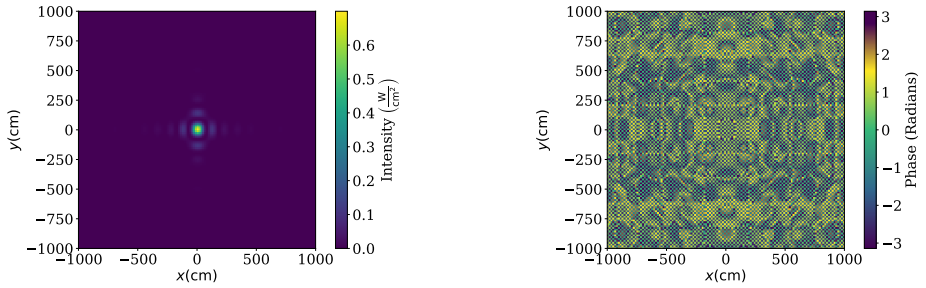

(a) Farfield Intensity **(b) Farfield Phase**

Figure 50. Contour plots of the intensity and phase for the baseline configuration located in a farfield location approximately $10000\,\mathrm{m}$ **from the laser cavity exit.**

is

$$U_{0,0}(x,y) = \left(\frac{2}{\pi}\right)^{1/2} \left(\frac{1}{w_{x,0}w_{y,0}}\right)^{1/2} e^{-\left(\frac{x}{w_{x,0}}\right)^2 - \left(\frac{y}{w_{y,0}}\right)^2} . \tag{290}$$

For the comparisons made concerning the research presented in this document, the reference beam was given the initial beam waist

$$\begin{aligned} w_{x,0} &= \frac{a_{2,x}}{3} , \\ w_{y,0} &= \frac{a_{2,y}}{3} , \end{aligned} \tag{291}$$

where $a_{2,x}$ and $a_{2,y}$ are the radii of the large mirror of the cavity. These beam waists were chosen in accordance with Siegman's principle in choosing[49] the aperture to contain at least 99.99% power in the output of the ideal laser. The ideal beam is then simulated as a reference beam. Both the reference beam and the actual cavity power output are propagated the same distance, $\Delta z = 10000\,\mathrm{m}$ into the farfield using equation (287). The intensity of the farfield reference beam and the laser resonator cavity output are then solved as a function of radial intensity. The power contained within the radius for both the reference beam and propagated beam are both calculated. Figure 51 indicates that a radius is calculated for the reference beam corresponding to the power contained within the first radial beam waist of an ideal Gaussian beam, which corresponds to 86.4% of the power in the ideal beam. The VPIB is then the fraction of output power of the system's actual farfield intensity, contained within the first radial beam waist of an ideal Gaussian beam. In other words, the VPIB is the ratio of a Gaussian power in the bucket measurement over the total power output from the system, or

$$\mathrm{VPIB} = \frac{\mathrm{PIB}_{\mathrm{Gauss}}}{P_{\mathrm{Tot}}} . \tag{292}$$

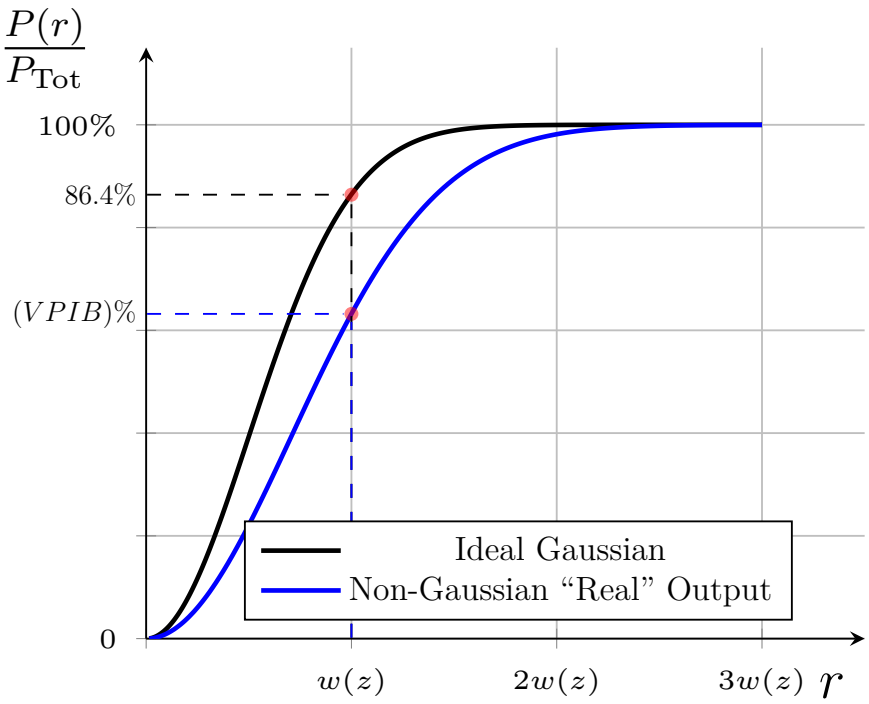

Figure 51. Total power contained within a radius r for an idealized gaussian mode and the total power contained within a radius r for an example cavity output. The VPIB is defined as the ratio of the power in the bucket of the ideal gaussian over the total power output of the cavity $\frac{\text{PIB}_{\text{Gauss}}}{P_{\text{Tot}}}$

For the results displayed in figure 50, the VPIB is a fraction of 78.86% of the cavity output. Considering the central obscuration associated with the cavity geometry, the baseline case has a fair amount of power delivered compared to a resonator with a similar Gaussian beam with a beam waist a third of the large mirror radii. For the baseline case, the VPIB calculation is a simplified number compared to the contour plot displayed in figure 50. However, when large studies are pursued in the following sections the simplified VPIB allows for broad analysis within each study.

A Study Modifying Fresnel Number

The first study associated with this analysis of the cavity with gain is similar to the study bare cavity eigenvalue study in chapter III. The laser cavity baseline given in the prior section had the smaller outcoupling mirror extent varied to analyze many different cavity Fresnel numbers. The larger back mirror and pump extent were also scaled the same as the outcoupling mirror in order to prevent diffractive losses. The Fresnel number associated with the x dimension of the small mirror was varied from $1 \rightarrow 10$ with sampling done for every eighth of a Fresnel number.

Figure 52 displays the overall change in efficiency as the Fresnel number is varied. Efficiency was calculated as the percentage ratio of the laser power output from the outcoupling mirror to the total pump power added to the cavity,

$$\eta_{\text{Eff}} = \frac{P_{\text{Laser,Out}}}{P_{\text{Pump,In}}} \, . \tag{293}$$

As the Fresnel number increases the efficiency of the the system approaches an asymptotic value of 51% corresponding to the efficiency that one would expect to occur for the geometric mode of the laser resonator. The efficiency curve is not smooth due to

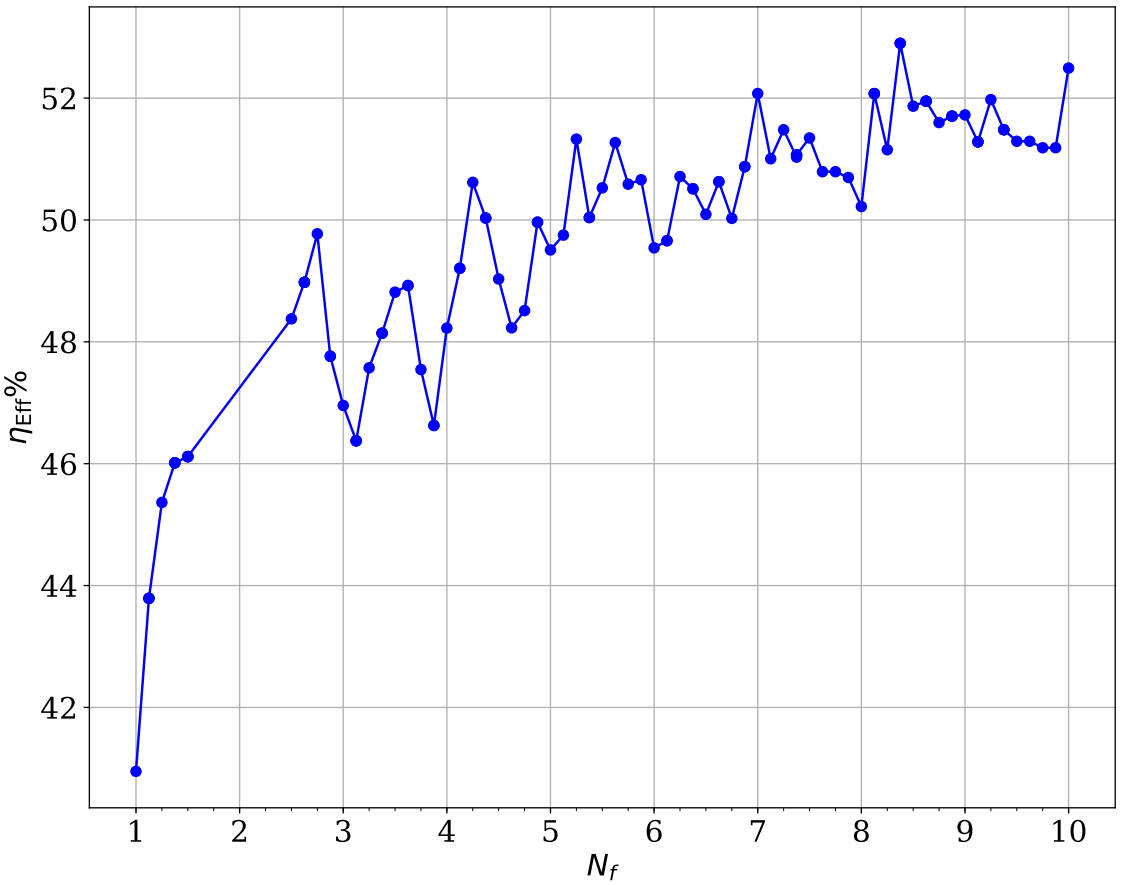

Figure 52. The efficiency as a function of the cavity Fresnel number. The variation in Fresnel number was achieved by scaling the transverse extents of the front and back mirrors while keeping all other parameters chosen for the baseline case constant.

the mode's volumetric shape changing as the Fresnel number of the unstable resonator was modified.

The VPIB variation as Fresnel number is increased is shown in figure 53, showing an inverse relationship between VPIB and Fresnel number. Such a relationship is due to a higher structure associated with the cavity mode as the Fresnel number is increased. Much as in the stable resonator the higher the cavity mode, the lower the VPIB measured.

A conclusion drawn from these results is that beam quality and efficiency of the laser system tend to act antagonistically against each other for the positive branch confocal unstable resonator. Applications involving the farfield propagation of an unstable resonator output field for a high gain system need to be tailored to maximize the total power output on target. The total power on target is a scaled value of both efficiency and VPIB for ideal propagation from the laser to the target. Therefore, both efficiency and VPIB have equal weighting for system design purposes where the goal is to have power on the target located in the farfield of the laser.

Analyzing the Effect of Mode-Gain Coupling

The results presented in the study varying Fresnel number indicate that the efficiency increase proportionally to the cavity Fresnel number. The reason for this general growth is related to change in the transverse intensity distribution coupling with the distribution of gain within the laser cavity. For cavity modes which have an intensity transversely distributed close to the axis of propagation, there is decreased efficiency compared to cavity modes more uniformly distributed across the gain medium. In order to quantify the relationship of the intensity distribution within the gain medium, two different parameters are defined in the next few subsections. The first is the Volumetric-Fill Coefficient, which is defined using the laser intensity

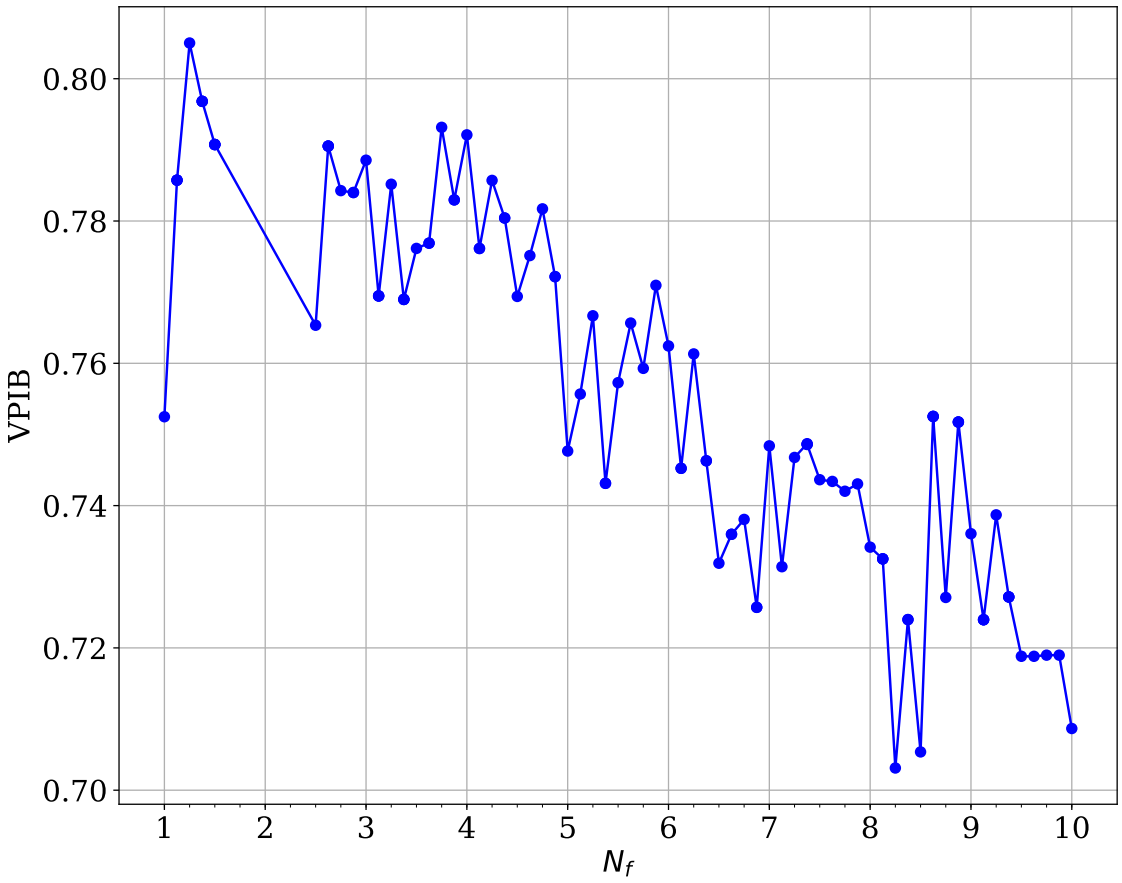

Figure 53. The VPIB as a function of the cavity Fresnel number. The variation in Fresnel number was achieved by scaling the transverse extents of the front and back mirrors while keeping all other parameters chosen for the baseline case constant.

propagation through a gain medium. The next parameter is the Mode-Fill Coefficient, which is a parameter which translates the Volumetric-Fill Coefficient to scale Hager's[10, 11] simplified laser model.

Determining the Volumetric-Fill Coefficient.

The Volumetric-Fill Coefficient comes from the idea that laser resonator modes will not equally fill the gain medium, and therefore will not couple with the gain medium in the same way as if the mode filled the cavity in its entirety. In the case where the laser intensity is allowed to fill the gain region transversely for the entire length of the gain medium, the Volumetric-Fill Coefficient should have a value of one. In cases where this is not true, the Volumetric-Fill Coefficient, Γ, is defined as

$$\Gamma = \text{Volume of mode normalized intensity coupled with the gain}\,. \tag{294}$$

The scale change of intensity as a function of propagation distance, may be written as an ODE,

$$\frac{\mathrm{d}I(x,y,z)}{\mathrm{d}z} = g_{ij}(x,y,z)I(x,y,z)\,, \tag{295}$$

where g_{ij} is the distribution of gain in the medium for the $i \to j$ optical transition, Integrating the transverse area gives

$$\iint \frac{\mathrm{d}I(x,y,z)}{\mathrm{d}z}\,\mathrm{d}x\,\mathrm{d}y = \iint g_{ij}(x,y,z)I(x,y,z)\,\mathrm{d}x\,\mathrm{d}y\ . \tag{296}$$

The integral on the left hand side of equation (296), may be rewritten as

$$P_{\text{Sheet}} = \iint I(x,y,z)\,\mathrm{d}x\,\mathrm{d}y\ , \tag{297}$$

which then may be used to rewrite equation (296) to

$$\frac{1}{P_{\text{Sheet}}}\frac{\mathrm{d}P_{\text{Sheet}}(z)}{\mathrm{d}z} = \frac{\iint g_{ij}(x,y,z)I(x,y,z)\,\mathrm{d}x\,\mathrm{d}y}{\iint I(x,y,z)\,\mathrm{d}x\,\mathrm{d}y}\,, \tag{298}$$

which has a general solution

$$P_{\text{Sheet}}(z+\Delta z) = P_{\text{Sheet}}(z)e^{\int_z^{z+\Delta z}\frac{\iint g_{ij}(x,y,z)I(x,y,z)\mathrm{d}x\mathrm{d}y}{\iint I(x,y,z)\mathrm{d}x\mathrm{d}y}\mathrm{d}z}\,. \tag{299}$$

The exponential in equation (299) may then be rewritten as a function of the average gain over the length traveled multiplied by an unidentified coefficient,

$$P_{\text{Sheet}}(z+\Delta z) = P_{\text{Sheet}}(z)e^{g_{ij,\text{avg}}\Gamma\Delta z}\,, \tag{300}$$

where

$$\Gamma = \frac{1}{\Delta z_{\text{G}}}\int_z^{z+\Delta z_{\text{G}}}\frac{\iint g_{ij}(x,y,z)I(x,y,z)\,\mathrm{d}x\,\mathrm{d}y}{g_{ij,\text{avg}}\iint I(x,y,z)\,\mathrm{d}x\,\mathrm{d}y}\,\mathrm{d}z\,. \tag{301}$$

Γ may also be approximated with a volumetric average,

$$\Gamma = \frac{\iiint_{\text{G}} g_{ij}(x,y,z)I(x,y,z)\,\mathrm{d}x\,\mathrm{d}y\,\mathrm{d}z}{\frac{1}{V_{\text{G}}}\iiint_{\text{G}} g_{ij}(x,y,z)\,\mathrm{d}x\,\mathrm{d}y\,\mathrm{d}z\iiint_{\text{G}} I(x,y,z)\,\mathrm{d}x\,\mathrm{d}y\,\mathrm{d}z}\,. \tag{302}$$

Γ is recognized as the Volumetric-Fill Coefficient and is able to be calculated from equation (302). The gain may be calculated from the γ reported by the gain wave-optic simulations by

$$g_{21} = \frac{2}{\delta z}\ln(|\gamma|) \tag{303}$$

where δz is the z resolution of the gain medium, and the intensity of the cavity calculated from

$$I = \frac{\varepsilon_0 c_0}{2}|U|^2\,. \tag{304}$$

The Volumetric-Fill Coefficient indicated in equation (302) only highlights optical propagation in one direction through the medium. Therefore, the baseline case requires the definition of two Volumetric-Fill Coefficients, one indicating the field propagation from $+\hat{z} \rightarrow -\hat{z}$, Γ^{-}, and the other indicating field propagation from $-\hat{z} \rightarrow +\hat{z}$, Γ^{+}. Both Volumetric-Fill Coefficients are then defined as

$$\Gamma^{-} = \frac{\iiint_{\mathrm{G}} g_{ij}(x,y,z) I^{-}(x,y,z)\,\mathrm{d}x\,\mathrm{d}y\,\mathrm{d}z}{\frac{1}{V_{\mathrm{G}}} \iiint_{\mathrm{G}} g_{ij}(x,y,z)\,\mathrm{d}x\,\mathrm{d}y\,\mathrm{d}z \iiint_{\mathrm{G}} I^{-}(x,y,z)\,\mathrm{d}x\,\mathrm{d}y\,\mathrm{d}z}\,, \tag{305}$$

$$\Gamma^{+} = \frac{\iiint_{\mathrm{G}} g_{ij}(x,y,z) I^{+}(x,y,z)\,\mathrm{d}x\,\mathrm{d}y\,\mathrm{d}z}{\frac{1}{V_{\mathrm{G}}} \iiint_{\mathrm{G}} g_{ij}(x,y,z)\,\mathrm{d}x\,\mathrm{d}y\,\mathrm{d}z \iiint_{\mathrm{G}} I^{+}(x,y,z)\,\mathrm{d}x\,\mathrm{d}y\,\mathrm{d}z}\,. \tag{306}$$

where $I^{-}(x,y,z)$ and $I^{+}(x,y,z)$ are the intensities of the backward and forward traveling fields respectively.

Measuring the Volumetric-Fill Coefficients for the cases covered in the Fresnel number study allows for one to see the relationship between the Volumetric-Fill Coefficient and the Fresnel number associated with the positive branch confocal unstable resonator cavity. Figure 54 is a plot of the Volumetric-Fill Coefficient as a function of Fresnel number. An initial positive trend is observed for Γ^{-} and Γ^{+} as Fresnel number increases with the growth of the Volumetric-Fill Coefficients ceasing after $N_{\mathrm{F}} = 7$. The positive trend also roughly follows the trend of the increasing efficiencies shown in figure 52 for both Γ^{-} and Γ^{+}. Although Γ^{-} and Γ^{+} both tend to follow the same trend, there are differences between both Volumetric-Fill Coefficients. This difference begs the question, "How do the Volumetric-Fill Coefficients actually relate to the output efficiency of the cavity?"

Comparing to Hager.

The question may be answered by modifying a simplified laser model, developed by Hager[10, 11], to include the effects of the Volumetric-Fill Coefficients. In order

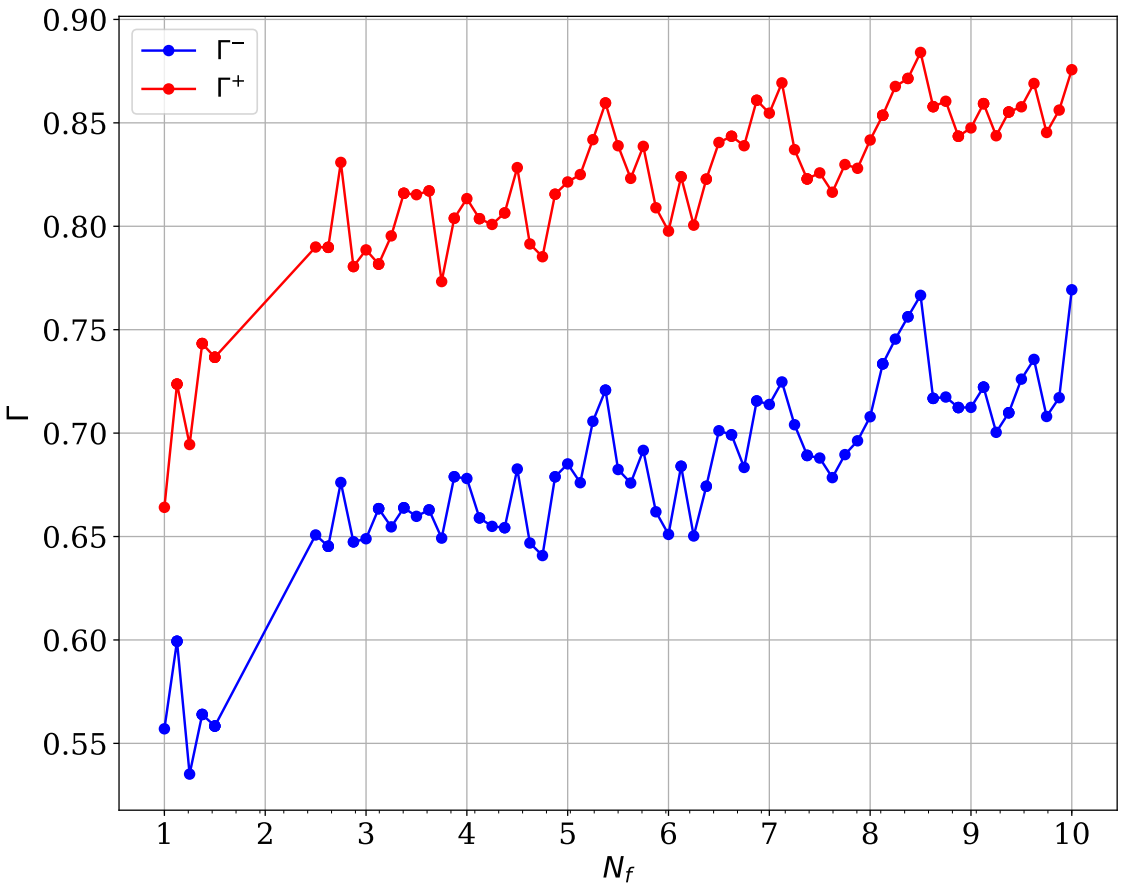

Figure 54. The Volumetric-Fill Coefficients for the forward, Γ^+, and backward, Γ^-, traveling fields as functions of varying the Fresnel number of the baseline case.

to accomplish the modification of Hager's Model, this subsection will be devoted to developing Hager's original model, modifying the model with a scaled Mode-Fill Coefficient, η_{Mode}, based upon the Volumetric-Fill Coefficients, and then determining the Mode-Fill Coefficient for the Volumetric-Fill Coefficients in figure 54.

In his work, Hager calculates the intracavity laser intensity based upon the laser intensity output. He does this by assuming the cavity geometry in figure 55. Within the picture, Hager assumed all of the intensities filled the cavity uniformally, which is not consistent with the unstable resonator intracavity mode.

Hager's intracavity intensity is recognized as a function of the intensities entering the gain cell I_2^- and I_2^+ averaged for the propagation of the intensity through the gain cell

$$\begin{aligned}\psi &= \frac{1}{\Delta z_{\text{G}}} I_2^- \int_0^{\Delta z_{\text{G}}} e^{g_{21} z}\,\mathrm{d}z + \frac{1}{\Delta z_{\text{G}}} I_2^+ \int_0^{\Delta z_{\text{G}}} e^{g_{21}(\Delta z_{\text{G}} - z)}\,\mathrm{d}z\ , \\ &= \left(\frac{e^{g_{21}(\Delta z_{\text{G}})} - 1}{g_{21}\Delta z_{\text{G}}}\right)\left(I_2^+ + I_2^-\right).\end{aligned} \tag{307}$$

The intensities entering the gain cell are also recognized to be functions of the output laser intensity

$$I_2^- = \frac{tr}{1-r} I_{\text{Laser}}\ , \tag{308}$$

$$I_2^+ = \frac{I_{\text{Laser}}}{t(1-r)e^{g_{21}\Delta z_{\text{G}}}}\ , \tag{309}$$

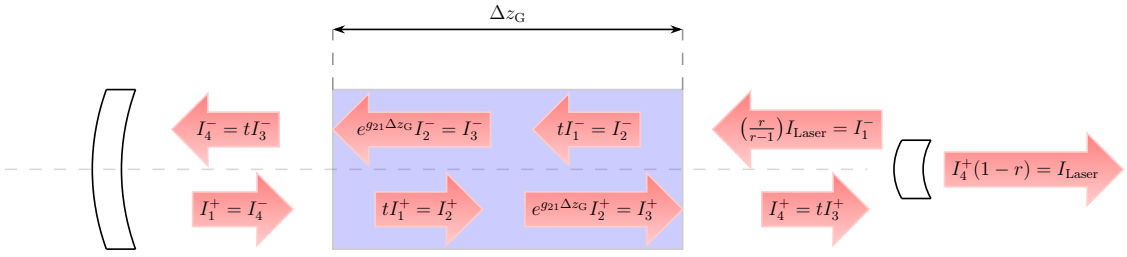

Figure 55. The original relationship for cavity position given by Hager[10] in his paper.

meaning equation (307) may be rewritten as a function of the output laser intensity

$$\psi = \left(\frac{e^{g_{21}\Delta z_{\mathrm{G}}} - 1}{g_{21}\Delta z_{\mathrm{G}}}\right)\frac{t^2 r e^{g_{21}\Delta z_{\mathrm{G}}} + 1}{t(1-r)e^{g_{21}\Delta z_{\mathrm{G}}}} I_{\mathrm{Laser}}\,. \tag{310}$$

Hager[11] recognized ψ is related to the total lasing rate, L through the relationship

$$L = g_{21}\frac{\psi}{h_{\mathrm{p}}\nu_L}\,. \tag{311}$$

For steady-state operation, the gain in the cavity has to increases the field enough to match the losses of the field for an entire pass through the cavity. The value for this gain is known as the gain threshold. For the scenario in figure 55 is defined by

$$g_{\mathrm{th}} = \frac{1}{\Delta z_{\mathrm{G}}}\ln\left(\frac{1}{\sqrt{r}t^2}\right)\,. \tag{312}$$

Steady-state operation of the cavity also requires that the energy density contained within the cavity stays steady. A consequence is the energy density added by the pump must be the same as the energy density removed by the laser. Therefore, the rate of pumping in the cavity,

$$P = \frac{I_{\mathrm{p}}}{h\nu_{\mathrm{p}}\Delta z_{\mathrm{G}}}\left[1 - \int_{-\infty}^{\infty} f_{\mathrm{p}}(\nu)e^{\sigma_{31}(\nu)(n_3(\Omega)-2n_1(\Omega))\Delta z_{\mathrm{G}}}\right] - \Gamma_{31}n_3 - \Gamma_{21}n_2\,, \tag{313}$$

must be equal to the rate of lasing. Using equation (310) for the intracavity intensity and combining equations (311) and (313) with the assumption $L = P$ allows for the calculation of the output laser intensity from the input pump parameters

$$I_{\mathrm{Laser}} = I_{\mathrm{p}}\frac{\nu_{\mathrm{L}}}{\nu_{\mathrm{p}}}\left[1 - \int_{-\infty}^{\infty} f_{\mathrm{p}}(\nu)e^{\sigma_{31}(\nu)(n_3(\Omega)-2n_1(\Omega))\Delta z_{\mathrm{G}}}\,\mathrm{d}\nu\right]T_{\mathrm{C,Orig}} - (\Gamma_{31}n_3 - \Gamma_{21}n_2)h_{\mathrm{p}}\nu_L\Delta z_{\mathrm{G}}T_{\mathrm{C,Orig}}\,. \tag{314}$$

where

$$T_{\mathrm{C,Orig}} = \frac{t(1-r)e^{g_{\mathrm{th}}\Delta z_{\mathrm{G}}}}{(t^2 r e^{g_{\mathrm{th}}\Delta z_{\mathrm{G}}}+1)(e^{g_{\mathrm{th}}\Delta z_{\mathrm{G}}}-1)}\,. \tag{315}$$

For implementation equation (314) was simplified in the paper [11] to be

$$I_{\mathrm{Laser}} = I_{\mathrm{p}}\eta_{qe}\beta T_{\mathrm{C,Orig}} - I_{\mathrm{th}}\,, \tag{316}$$

where the threshold pump intensity is defined as

$$I_{\mathrm{th}} = I_{\mathrm{S}}\eta_{qe}\left[\sigma_{31}\Delta z_{\mathrm{G}}\left(n_3 + n_2\frac{\Gamma_{21}}{\Gamma_{31}}\right)\right]T_{\mathrm{C,Orig}}\,, \tag{317}$$

the saturation intensity, defined at line center of the alkali medium, is

$$I_{\mathrm{S}} = \frac{h_{\mathrm{p}}\nu_{\mathrm{p}}}{\sigma_{31}}\Gamma_{31}\,, \tag{318}$$

the quantum efficiency is

$$\eta_{qe} = \frac{\nu_{\mathrm{L}}}{\nu_{\mathrm{P}}}\,, \tag{319}$$

and the coupling of the pump intensity to the cavity is

$$\beta = \left[1 - \int_{-\infty}^{\infty} f_{\mathrm{p}}(\nu)e^{\sigma_{31}(\nu)(n_3(\Omega)-2n_1(\Omega))\Delta z_{\mathrm{G}}}\,\mathrm{d}\nu\right]. \tag{320}$$

A volumetric fill coefficient was added as a fit factor by Hager[10] in his original paper on the method,

$$I_{\mathrm{Laser}} = \eta_{\mathrm{Mode}}I_{\mathrm{p}}\eta_{qe}\beta T_{\mathrm{C,Orig}} - \eta_{\mathrm{Mode}}I_{\mathrm{th}}\,. \tag{321}$$

In order to calculate η_{Mode}, the illustration in figure 55 is modified to the one pictured in figure 56. Using the previous definition of the intracavity intensity and the

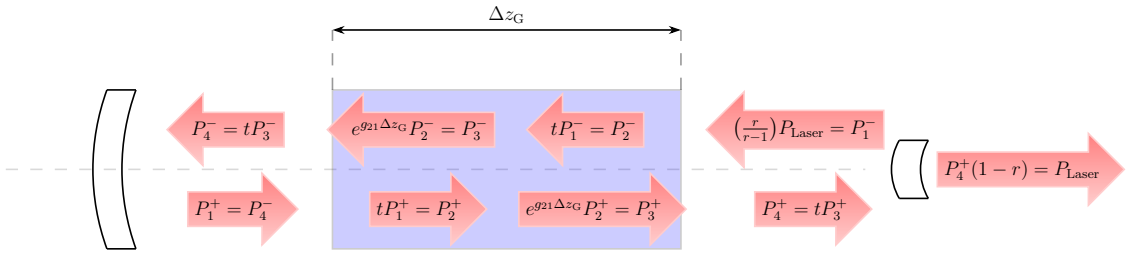

Figure 56. Location of various power sheets for cavity position, modified from figure 55.

Volumetric-Fill Coefficient in equation (299) allows for the intracavity intensity to be rewritten as

$$\begin{aligned}\psi &= \frac{1}{\Delta z_{\mathrm{G}}\Gamma^- A_{\mathrm{G}}}P_2^- \int_0^{\Delta z_{\mathrm{G}}} e^{g_{\mathrm{th}}z}\,\mathrm{d}z + \frac{1}{\Delta z_{\mathrm{G}}\Gamma^+ A_{\mathrm{G}}}P_2^+ \int_0^{\Delta z_{\mathrm{G}}} e^{g_{\mathrm{th}}(\Delta z_{\mathrm{G}}-z)}\,\mathrm{d}z\ , \\ &= \left(\frac{e^{g_{\mathrm{th}}(\Delta z_{\mathrm{G}})}-1}{g_{\mathrm{th}}\Delta z_{\mathrm{G}}}\right)\left(\frac{P_2^+}{\Gamma^+}+\frac{P_2^-}{\Gamma^-}\right),\end{aligned} \tag{322}$$

where the gain has been assumed to be the steady state threshold value and that the power in a sheet is spread equally over the gain medium. By following through the same calculation as performed above with the recognition that

$$I_{\mathrm{Laser}} = \frac{P_{\mathrm{Laser}}}{A_{\mathrm{G}}}\,, \tag{323}$$

a new final equation for the laser output intensity is

$$I_{\mathrm{Laser}} = I_{\mathrm{p}}\eta_{qe}\beta T_{\mathrm{C}} - I_{\mathrm{th}}\frac{T_{\mathrm{C}}}{T_{\mathrm{C,Orig}}}\,, \tag{324}$$

where coupling coefficient has been modified to be

$$T_{\mathrm{C}} = \frac{t(1-r)e^{g_{\mathrm{th}}\Delta z_{\mathrm{G}}}}{\left(t^2 r\Gamma^{--1}e^{g_{\mathrm{th}}\Delta z_{\mathrm{G}}}+\Gamma^{+-1}\right)\left(e^{g_{\mathrm{th}}\Delta z_{\mathrm{G}}}-1\right)}\,. \tag{325}$$

From equation (324), η_{Mode} is the ratio of the modified coupling coefficient with the original coupling coefficient

$$\begin{aligned}\eta_{\text{Mode}} &= \frac{T_{\text{C}}}{T_{\text{C,Orig}}}\,, \\ &= \frac{t^2 r e^{g_{\text{th}}\Delta z_{\text{G}}} + 1}{t^2 r \Gamma^{--1} e^{g_{\text{th}}\Delta z_{\text{G}}} + \Gamma^{+-1}}\,,\end{aligned} \tag{326}$$

and by using the definition given in equation (312) along with the assumption that $t = 1$ for window transmission, allows η_{Mode} to be written as

$$\eta_{\text{Mode}} = \frac{\sqrt{r} + 1}{\sqrt{r}\Gamma^{--1} + \Gamma^{+-1}}\,. \tag{327}$$

Applying equation (327) to the Volumetric-Fill Coefficients calculated in figure 54 allows for η_{Mode} to be plotted as a function of laser cavity Fresnel number shown in figure 57. Immediately, one sees the positive trend found in figure 52 is duplicated in the Mode-Fill Coefficient. There are also some small variations between the trends in efficiency and η_{Mode}. These are due to the change in real outcoupling of the laser mode of the system to the outside of the cavity, which modify both the efficiency predicted from the simplified Hager model in addition to modifying η_{Mode}.

Equation (327) represents not only a method of directly comparing simulation results to Hager calculations, but also represents a method for predictively calculating the effects of various internal cavity modes on the Hager calculations. A special case worth exploration is the geometric mode associated with the positive branch confocal unstable resonator.

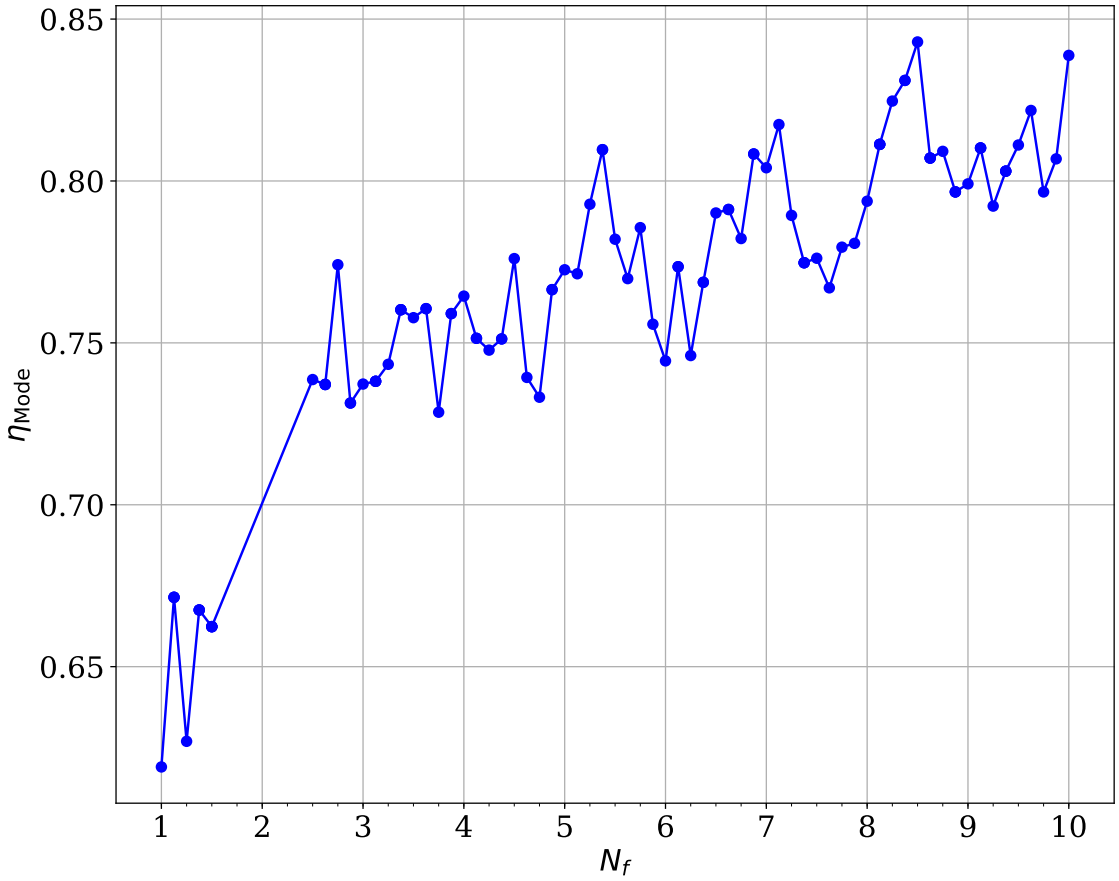

Figure 57. The Mode-Fill Coefficient, η_{Mode}, as a function of varying the Fresnel number of the baseline case.

The Geometric Mode.

If g_{21} is uniform and larger than or equal to uniform I which only partially fills the cavity, equations (305) and (306) become

$$\Gamma^{-} = \frac{V_{I^{-}}}{V_{\mathrm{G}}}\,, \tag{328}$$

$$\Gamma^{+} = \frac{V_{I^{+}}}{V_{\mathrm{G}}}\,. \tag{329}$$

where $V_{I^{-}}$ is the geometric volume of the intensity of the field traveling from the outcoupling mirror to the back mirror, $V_{I^{+}}$ is the geometric volume of the intensity of the field traveling from the back mirror to the front mirror, and V_{G} is the volume of the gain available for lasing. Using figure 58, which lays out the geometric mode path in the cavity, identifies

$$V_{I^{-}} = V_{\mathrm{Trapz}}\,, \tag{330}$$

$$V_{I^{+}} = V_{\mathrm{G}}\,, \tag{331}$$

where V_{Trapz} is the volume displayed in figure 59. The shape in figure 59 has a volume of

$$V_{\mathrm{Trapz}} = a_x a_y h + \frac{1}{2}(b_x - a_x)a_y h + \frac{1}{2}(b_y - a_y)a_x h + \frac{1}{3}(b_x - a_x)(b_y - a_y)h\,, \tag{332}$$

where the dimensions correspond to those within the figure 59. Using the definitions in figure 58 allows for the following relationships to be identified with the dimensions

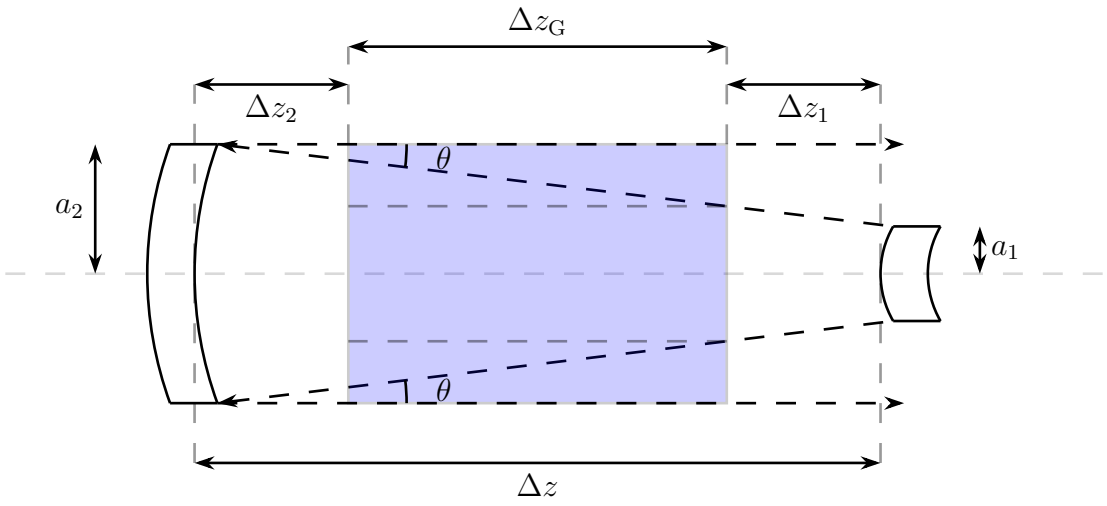

Figure 58. The propagation path of the geometric mode within the positive branch confocal resonator

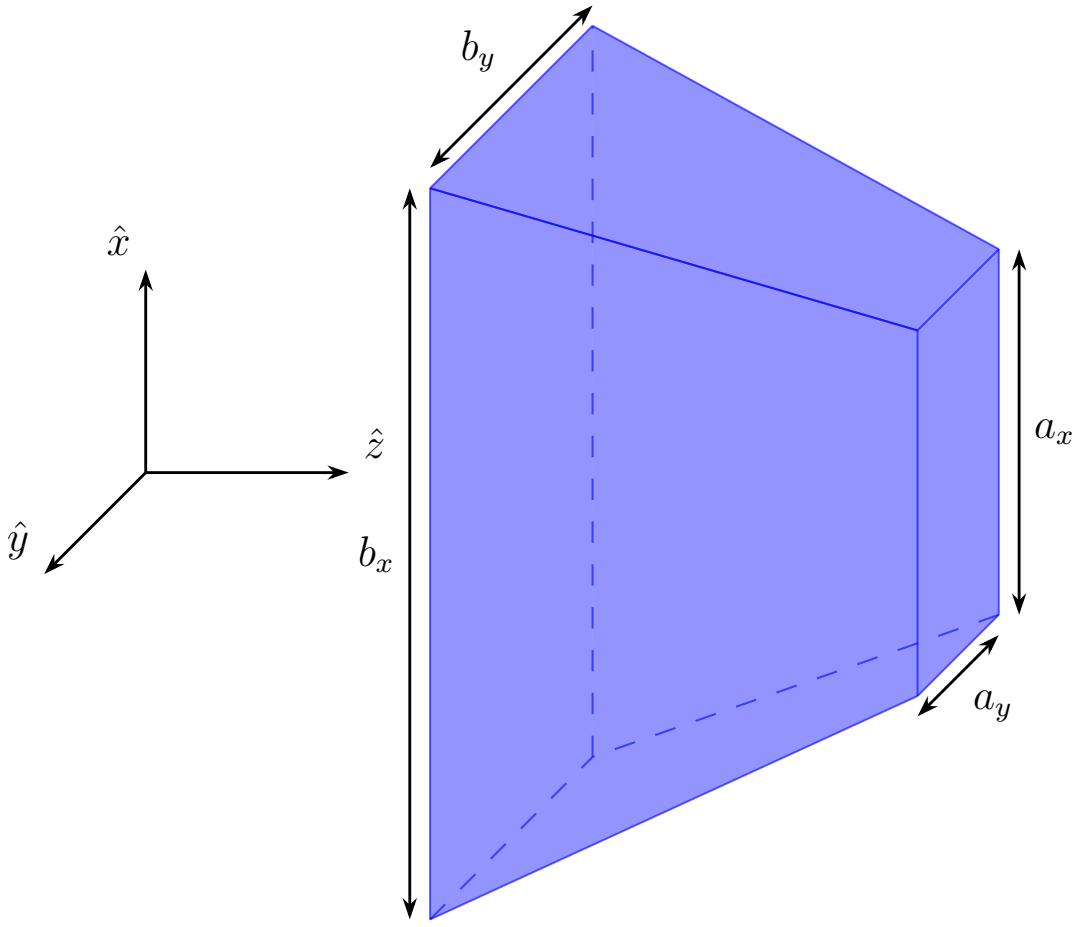

Figure 59. The trapezoidal prism represented the geometric laser mode traveling in the $-\hat{z}$ direction.

in figure 59

$$a_x = 2(a_{1,x} + \Delta z_1 \tan(\theta_x)) \,, \tag{333}$$

$$a_y = 2(a_{1,y} + \Delta z_1 \tan(\theta_y)) \,, \tag{334}$$

$$b_x - a_x = 2\Delta z_{\mathrm{G}} \tan(\theta_x) \,, \tag{335}$$

$$b_y - a_y = 2\Delta z_{\mathrm{G}} \tan(\theta_y) \,, \tag{336}$$

$$\theta_x = \operatorname{atan}\left(\frac{a_{2,x} - a_{1,x}}{\Delta z}\right) , \tag{337}$$

$$\theta_y = \operatorname{atan}\left(\frac{a_{2,y} - a_{1,y}}{\Delta z}\right) , \tag{338}$$

$$h = \Delta z_{\mathrm{G}} \,, \tag{339}$$

which means the volume is now

$$\begin{aligned} V_{\mathrm{Trapz}} = 4 &\left[a_{1,x} + \frac{\Delta z_1}{\Delta z}(a_{2,x} - a_{1,x})\right]\left[a_{1,y} + \frac{\Delta z_1}{\Delta z}(a_{2,y} - a_{1,y})\right]\Delta z_{\mathrm{G}} \\ &+ \left[\frac{\Delta z_{\mathrm{G}}}{\Delta z}(a_{2,x} - a_{1,x})\right]\left[a_{1,y} + \frac{\Delta z_1}{\Delta z}(a_{2,y} - a_{1,y})\right]\Delta z_{\mathrm{G}} \\ &+ \left[\frac{\Delta z_{\mathrm{G}}}{\Delta z}(a_{2,y} - a_{1,y})\right]\left[a_{1,x} + \frac{\Delta z_1}{\Delta z}(a_{2,x} - a_{1,x})\right]\Delta z_{\mathrm{G}} \\ &+ \frac{4}{3}\left[\frac{\Delta z_{\mathrm{G}}}{\Delta z}(a_{2,x} - a_{1,x})\right]\left[\frac{\Delta z_{\mathrm{G}}}{\Delta z}(a_{2,y} - a_{1,y})\right]\Delta z_{\mathrm{G}} \,. \end{aligned} \tag{340}$$

All of the mirror size dimensions in (340) may be rewritten as a function of the back mirror spot size, $a_{2,x}$ and $a_{2,y}$, using the definition of geometric magnification, M, to

be

$$V_{\text{Trapz}} = \left[\frac{1}{M} + \frac{\Delta z_1}{\Delta z}\left(1 - \frac{1}{M}\right)\right]^2 4a_{2,x}a_{2,y}\Delta z_{\text{G}} + \left[\frac{1}{M} + \frac{\Delta z_1}{\Delta z}\left(1 - \frac{1}{M}\right)\right] 4a_{2,x}a_{2,y}\Delta z_{\text{G}} + \frac{1}{3}\left[\frac{\Delta z_{\text{G}}}{\Delta z}\left(1 - \frac{1}{M}\right)\right]^2 4a_{2,x}a_{2,y}\Delta z_{\text{G}}\,. \quad (341)$$

Knowing that the volume of the gain region is

$$V_{\text{Gain}} = 4a_{2,x}a_{2,y}\Delta z_{\text{G}}\,, \quad (342)$$

allows for the calculation of the ratio of the trapezoidal volume over the gain region as

$$\frac{V_{Trapz}}{V_{\text{Gain}}} = \left[\frac{1}{M} + \frac{\Delta z_1}{\Delta z}\left(1 - \frac{1}{M}\right)\right]^2 + \left[\frac{\Delta z_{\text{G}}}{\Delta z}\left(1 - \frac{1}{M}\right)\right]\left[\frac{1}{M} + \frac{\Delta z_1}{\Delta z}\left(1 - \frac{1}{M}\right)\right] + \frac{1}{3}\left[\frac{\Delta z_{\text{G}}}{\Delta z}\left(1 - \frac{1}{M}\right)\right]^2 \quad (343)$$

Therefore, the Volumetric-Fill Coefficients for the geometric mode of the positive branch confocal unstable resonator are

$$\Gamma^{-} = \left[\frac{1}{M} + \frac{\Delta z_1}{\Delta z}\left(1 - \frac{1}{M}\right)\right]^2 + \left[\frac{\Delta z_{\text{G}}}{\Delta z}\left(1 - \frac{1}{M}\right)\right]\left[\frac{1}{M} + \frac{\Delta z_1}{\Delta z}\left(1 - \frac{1}{M}\right)\right] + \frac{1}{3}\left[\frac{\Delta z_{\text{G}}}{\Delta z}\left(1 - \frac{1}{M}\right)\right]^2, \quad (344)$$

and

$$\Gamma^{+} = 1\,. \tag{345}$$

The Mode-Fill Coefficient in equation (327), may be simplified geometrically by recognizing the reflectivity of the cavity outcoupler is

$$r = \frac{1}{M^2}\,. \tag{346}$$

The Mode-Fill Coefficient for the geometric mode is then defined as

$$\eta_{\text{Mode}} = \frac{\frac{1}{M} + 1}{\frac{1}{M}\Gamma^{-^{-1}} + \Gamma^{+^{-1}}}\,. \tag{347}$$

Equation (347) is the scaling constant which modifies Hager's method to account for the geometric mode as a very simple calculation. For the baseline case where the gain cell is defined to be centered between both cavity mirrors is shown in figure 60, the minimum η_{Mode} occurs when $\frac{1}{M} \approx \frac{2}{5}$ and a gain cell to cavity ratio of zero. The maximum η_{Mode} is maximized for the case where $\frac{1}{M} = 1$ which would indicate no magnification of the system. Counterintuitively, η_{Mode} seems to reach a maximum for scenarios of $\frac{1}{M} \to 0$. This counterintuitive effect on η_{Mode} is due to the fact that η_{Mode} is not the Volumetric-Fill Coefficient, but is the way that the Volumetric-Fill Coefficient couples into the outcoupling. The larger the outcoupling from the cavity, the smaller the effects of the Volumetric-Fill Coefficient for the $-\hat{z} \to +\hat{z}$ propagation, Γ^{-}. If Γ^{+} is not zero, then η_{Mode} will have a maximum at $\frac{1}{M} = 0$. As seen in figure 61, moving the gain cell to the large mirror in the baseline case greatly increases η_{Mode} for all values of $\frac{1}{M}$ as well as moving the minimum for η_{Mode} to cases where the size of $\frac{\Delta z_{\text{G}}}{\Delta z}$ is large. The reasoning behind this may be seen from figure 58 where the mode has a larger area overall next to the large mirror, so the volumetric fill ratio is large for I^{-} near the back mirror and can only shrink as the gain cell is increased in

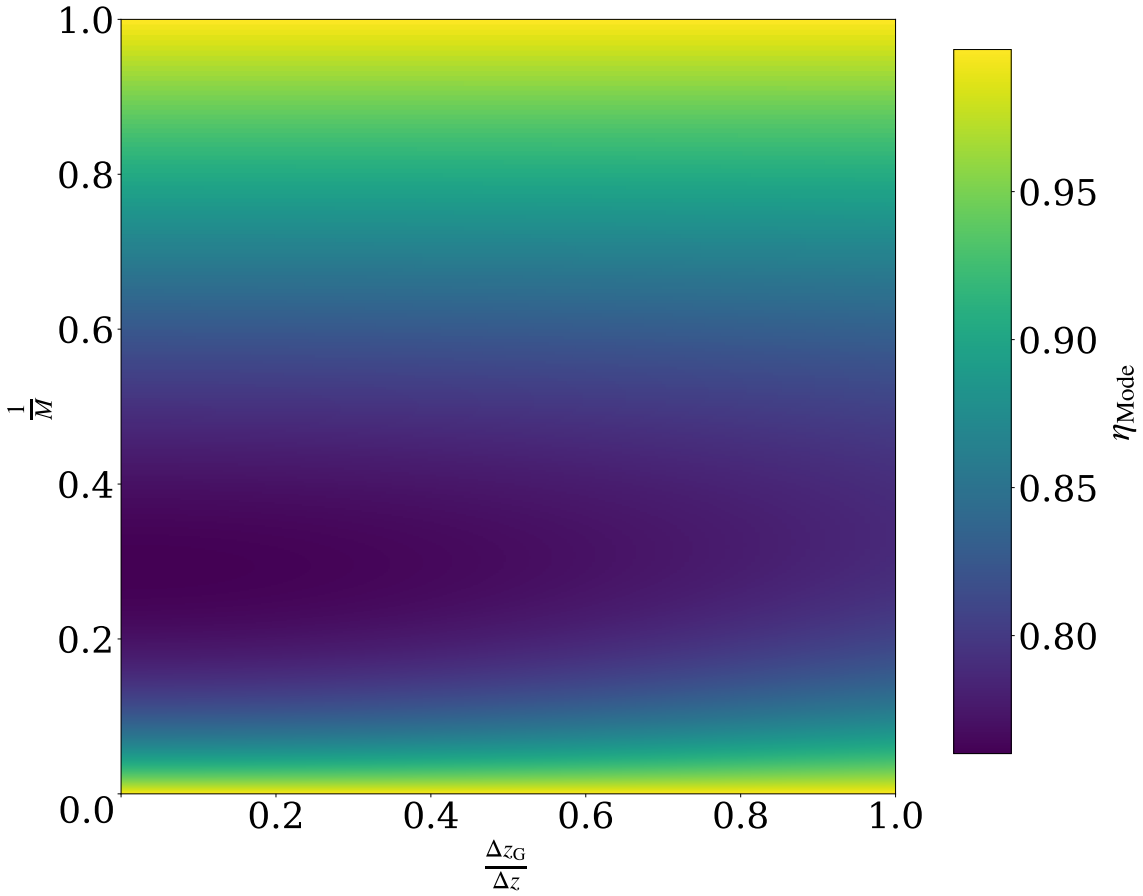

Figure 60. The Mode-Fill Coefficient, given by equation (347), as a function of gain and inverse geometric magnification. The gain cell is centered between both mirrors.

length. For the case where the gain cell is located near the small mirror, there η_{Mode} is much smaller. Again from the picture in figure 58, the size of I^- is small meaning that the mode tends to be small for most values of $\frac{1}{M}$. One should notice that as $\frac{\Delta z_G}{\Delta z} \to 1$, all the mirror positions approach the same value because at $\frac{\Delta z_G}{\Delta z} = 1$ all of the cavity positions are equivalent laser resonator geometries. Before moving onto the next section, it is important to note that the baseline case defined earlier in the chapter has a $\eta_{\text{Mode}} = 0.794$. The baseline case Mode-Fill Coefficient will be helpful when analyzing the modes for studies varying gain parameters, gain cell position, and gain cell length.

Adding the predicted geometric mode to figure 54, pictured in figure 63, allows one to see the predicted geometric Volumetric-Fill Coefficients greatly overestimate the forward traveling Volumetric-Fill Coefficient, Γ^+ and greatly underestimates the backward traveling Volumetric-Fill Coefficient, Γ^-. However, as shown in figure 64, the geometric mode prediction seems to be the asymptote of the Mode-Fill Coefficient indicating that effect of the predicted Volumetric Mode Coefficient must be used with the definition of the Mode-Fill Coefficient given in equation (347) to scale Hager's Model to include the effects of the cavity mode.

A Study Varying the Gain Medium Parameters

This study involved singly varying the gain medium operation parameters around those defined in the baseline case. Input pump intensity, gas pressure, gas temperature, rubidium density within the gas, and laser resonator magnification were all modified individually from the baseline case. All parameter scans were also completed for for five different cavity Fresnel numbers, with the cavity Fresnel number adjusted by modifying only the mirror extents presented in the baseline case. The results were compared to the unscaled Hager Model and the Hager model scaled by

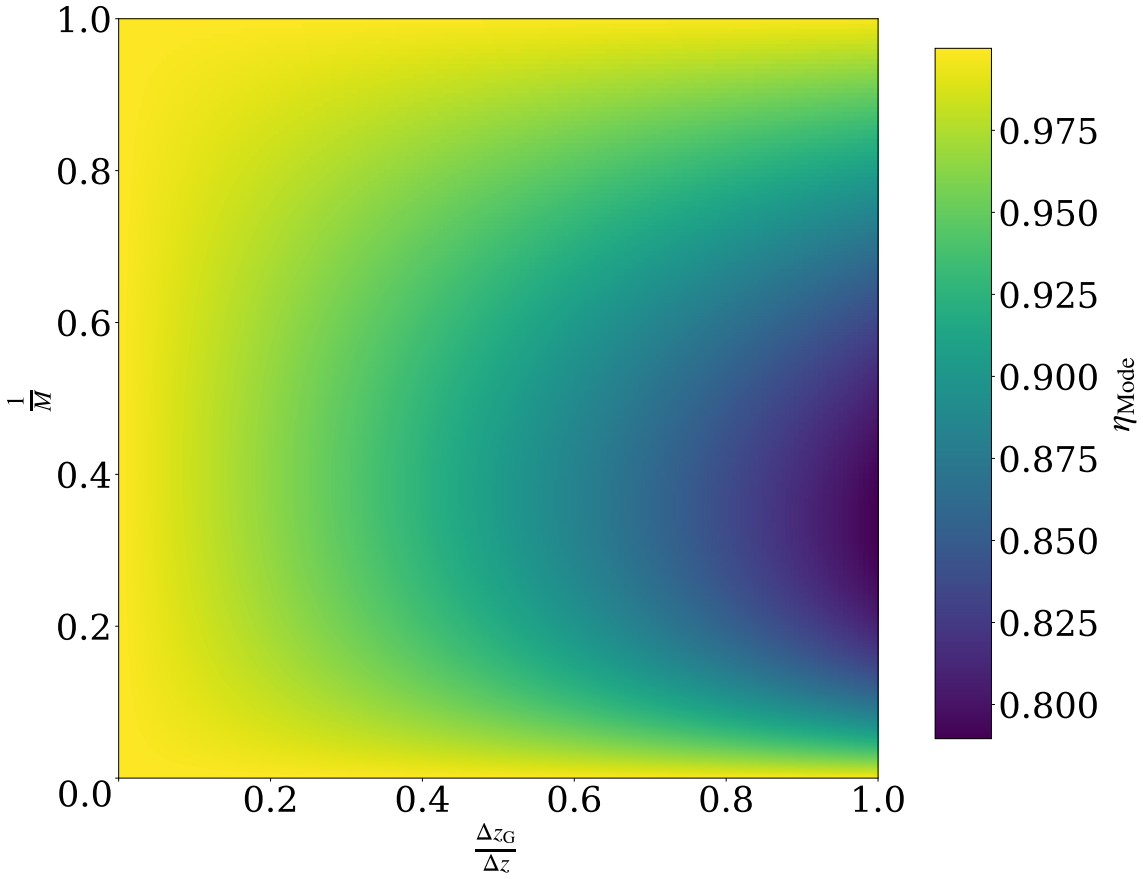

Figure 61. The Mode-Fill Coefficient, given by equation (347), as a function of gain and inverse geometric magnification. The gain cell is located at the back mirror.

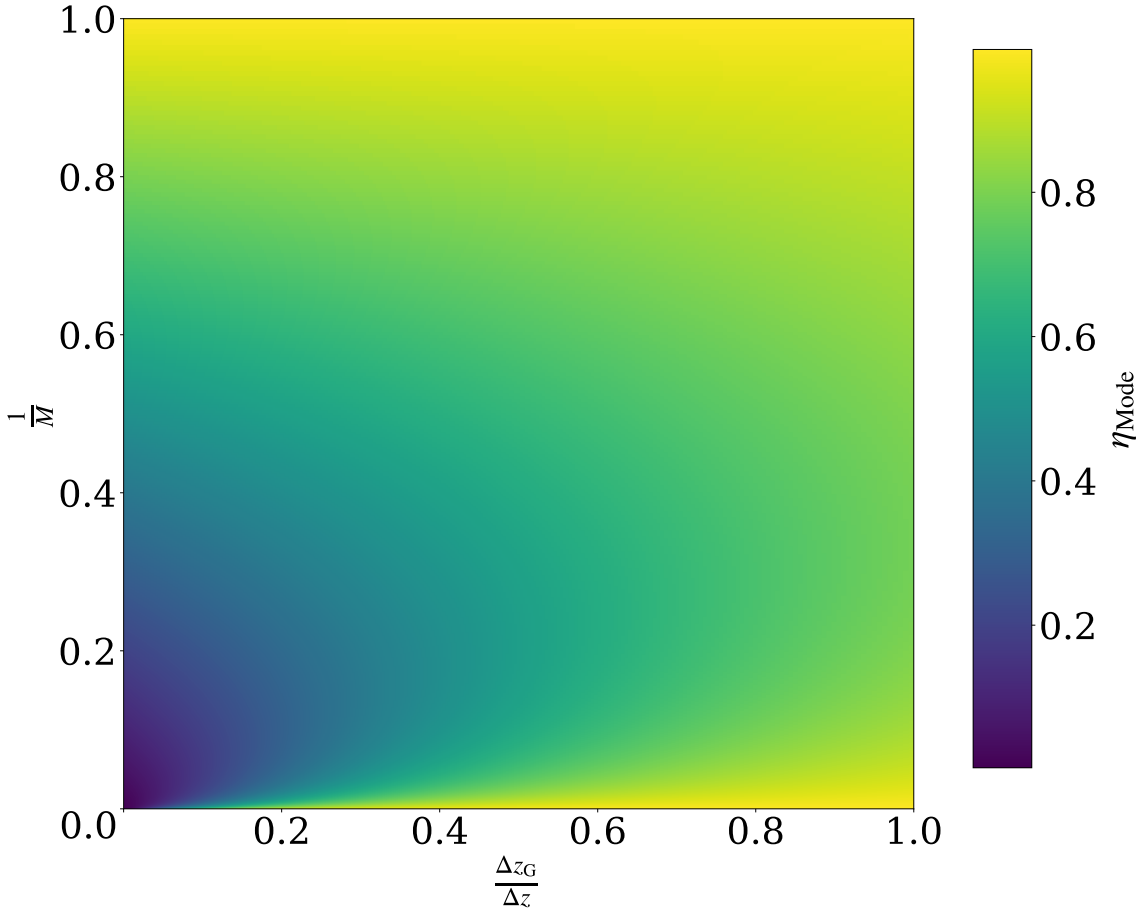

Figure 62. The Mode-Fill Coefficient, given by equation (347), as a function of gain and inverse geometric magnification. The gain cell is located at the front mirror.

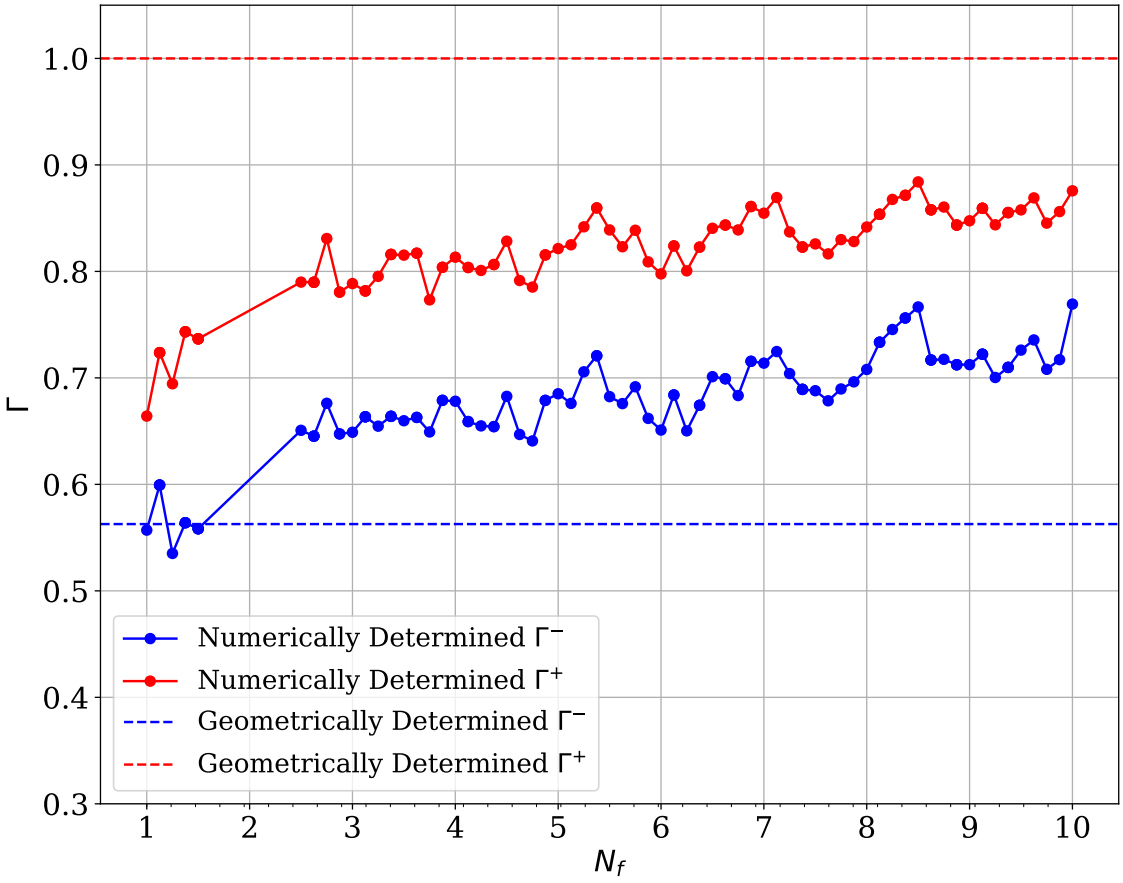

Figure 63. The Volumetric-Fill Coefficients for the forward, Γ^+, and backward, Γ^-, traveling fields as functions of varying the Fresnel number of the baseline case. Also pictured are the predicted Volumetric-Fill Coefficients for the geometric mode associated with the positive branch confocal unstable resonator.

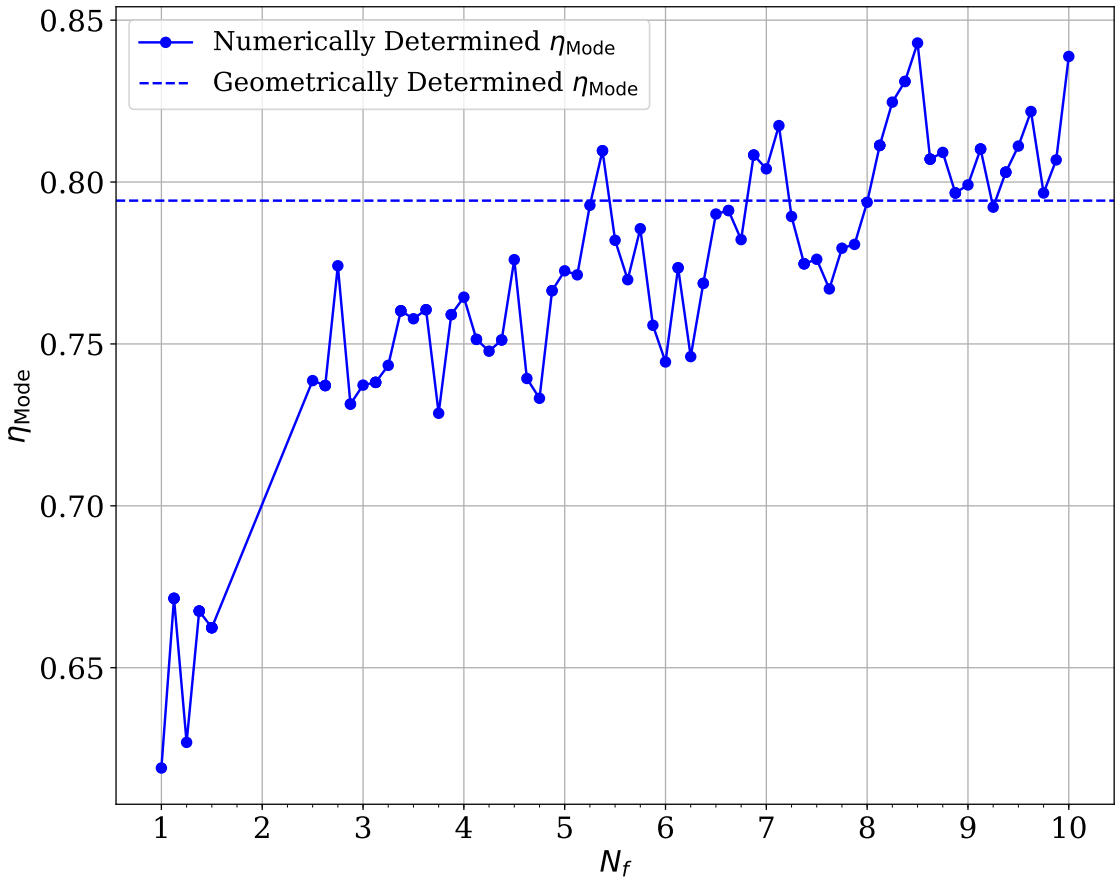

Figure 64. The Mode-Fill Coefficient, η_{Mode}, as a function of varying the Fresnel number of the baseline case.Also pictured is the predicted Mode-Fill Coefficients for the geometric mode associated with the positive branch confocal unstable resonator.

the predicted geometric mode fill. Also compared were the Hager model results scaled by the Mode-Coefficient actually calculated by the gain wave-optic simulation.

The study began with looking efficiency varying the input pump intensity. The results of the study are shown in figure 65. The trends between the Hager model predictions and the gain wave-optic simulations both seem to agree with one another. Applying the Mode-Fill Coefficient seems to scale Hager to the values calculated from the wave-optic gain simulation. The minor differences may be attributed to diffraction being present in the wave-optic simulation versus the scaled Hager simulation. The overall trend in figure 65 may be explained that as the input pump intensity is increased, eventually the gain medium will not respond to additional pump due to the optical processes overwhelming the fine structure mixing of the cavity. If the fine structure mixing of the three-level process is overwhelmed, the lasing rate may no longer be increased with the addition of pump intensity, meaning that the efficiency decreases as pump intensity increases.

The next part of the study involved varying the efficiency of the cavity as a function of temperature shown in figure 66. As mentioned for figure 65, the use of the scaled mode gives good agreement between the high Fresnel number wave-optic gain simulations and Hager's model. Increasing the temperature causes an overall, decrease within the system. The trend is due to the decrease in density of the helium buffer gas due associated with the increase in temperature of the system.

An analysis of the efficiency as a function of pressure is shown in figure 67. As in the prior cases, the use of the scaled mode gives good agreement between the high Fresnel number wave-optic gain simulations and Hager's model. The overall trend of the laser stems from two competing effects. Higher pressure leads to larger fine-structure mixing, thereby a greater transition from $5^2P_{3/2}$ to $5^2P_{1/2}$ granting a larger laser population for the gain medium. However, increased pressure also broadens the

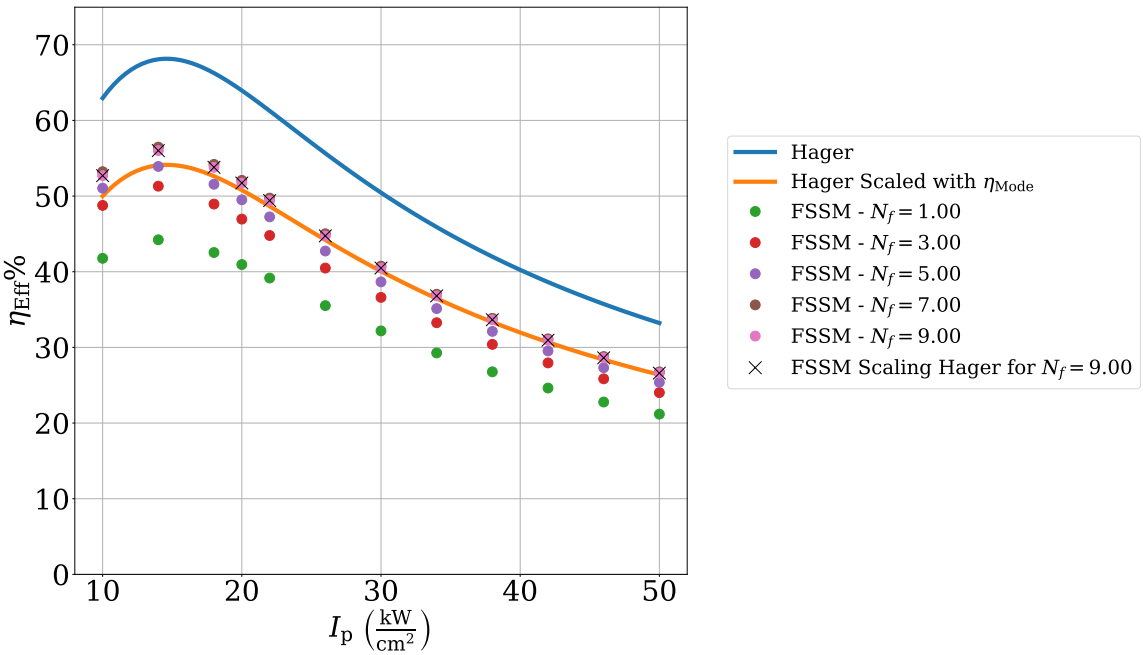

Figure 65. The efficiency of the laser resonator as a function of modifying the input pump intensity. Many different Fresnel numbers were calculated using the wave-optic gain simulation, as well as the unscaled Hager, and the scaled Hager using the predictive η_{Mode} for the geometric mode within the cavity.

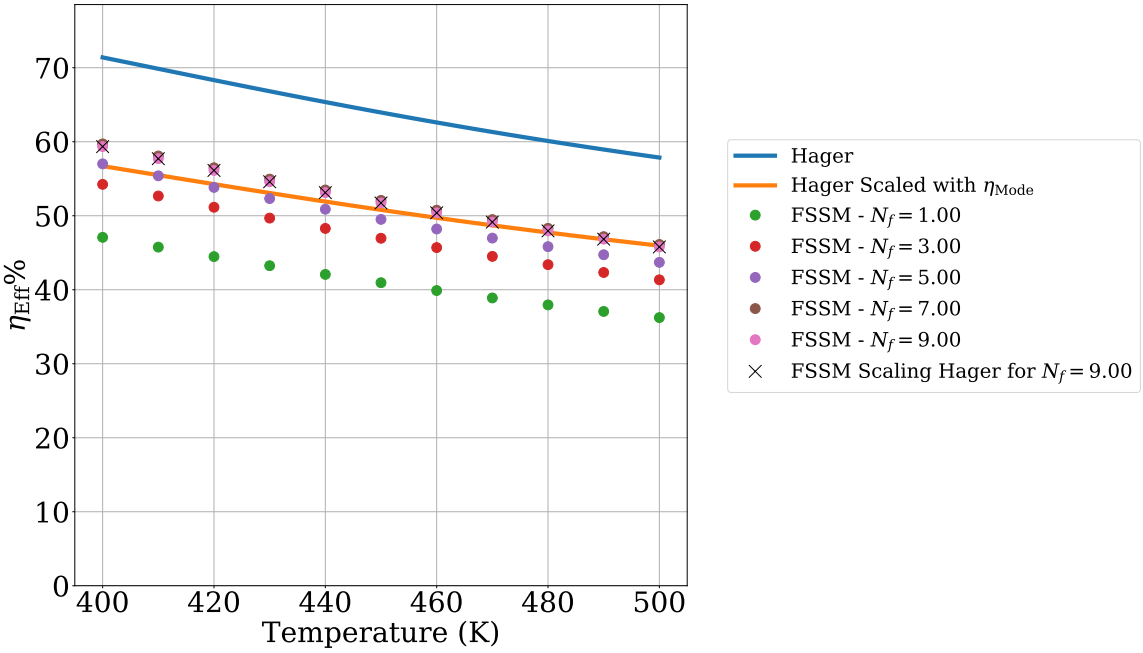

Figure 66. The efficiency of the laser resonator as a function of modifying the temperature of the cavity. Many different Fresnel numbers were calculated using the wave-optic gain simulation, as well as the unscaled Hager, and the scaled Hager using the predictive η_{Mode} for the geometric mode within the cavity.

natural linewidth absorption of the pump. Such a broadening leads to a smaller pump absorptive cross-section, meaning that less pump is able to be absorbed by the cavity. These two trends lead to the combined increase of efficiency as the helium pressure of the cavity is increased followed by a decrease of the cavity absorption beyond a certain point.

The next variation of the study involved modifying efficiency by varying the rubidium density of the cavity, which is shown in figure 68. Unfortunately for many of the lower Fresnel number runs, convergence of the simulation was not able to be achieved, these were left off of the plot. The lack of convergence could not be verified to correspond to a physical effect, but may have been due to multi-mode operation of the system or to the laser "flickering." Laser "flickering," is due to the gain medium initially supporting lasing due to the bleaching of the pump, followed by a pass in which the laser intensity decreases the gain of the medium along the laser intensity line, making the gain medium opaque, followed by a pass where the lack of laser intensity allows the gain to be bleached by the pump once again. This pattern consistently repeats itself preventing the simulation from converging for these high values of rubidium density. Another interesting facet of this part of the study was that unlike the previous segments of the study, the Hager prediction scaled by the geometric Mode-Fill Coefficient did not match the convergent wave-optic gain simulations after the maximum efficiency was observed. The effects of which are believed to be caused by a departure of the mode from a geometric layout within the cavity. Such a departure indicates that the gain in the cavity is very large, leading to a more "filled" cavity in terms of intracavity intensity. The overall trend may be explained by additional rubidium allowing for a higher lasing rate by increasing n_2 and n_1 in g_{21}. However, too much rubidium prevents the optical bleaching of the cavity by the

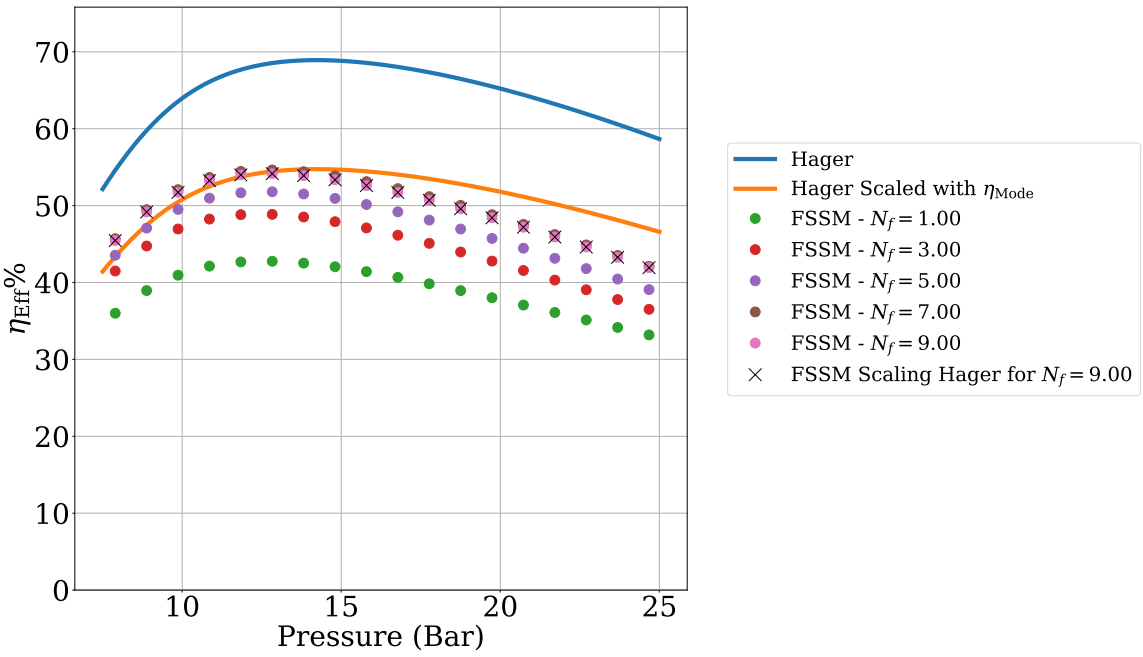

Figure 67. The efficiency of the laser resonator as a function of modifying the helium pressure of the cavity. Many different Fresnel numbers were calculated using the wave-optic gain simulation, as well as the unscaled Hager, and the scaled Hager using the predictive η_{Mode} for the geometric mode within the cavity.

pump, leading to the creation of an absorption region within the gain medium. The absorption region degrades laser output intensity leading to less system efficiency.

The final segment of the study focused on modifying the efficiency by varying the cavity configuration of the mirrors within the resonator. Figure 69 shows results of the gain wave-optic simulations compared against the Hager and scaled Hager predictions. The agreement seen in the prior aspects only occurs for higher values of geometric magnification. The difference in trends between the gain wave-optic simulations and the results predicted by Hager and the scaled Hager code may be due to cavity mode not being indicative of the geometric mode. The overall trend in the magnification is explained by the decreased Volumetric-Fill Coefficient for the magnifications displayed and the increased laser outcoupling for increasing magnification. Also worth mentioning in figures 65 to 69 are the results of scaling Hager by the individual Mode-Fill Coefficients directly calculated from the gain wave-optics simulations using the

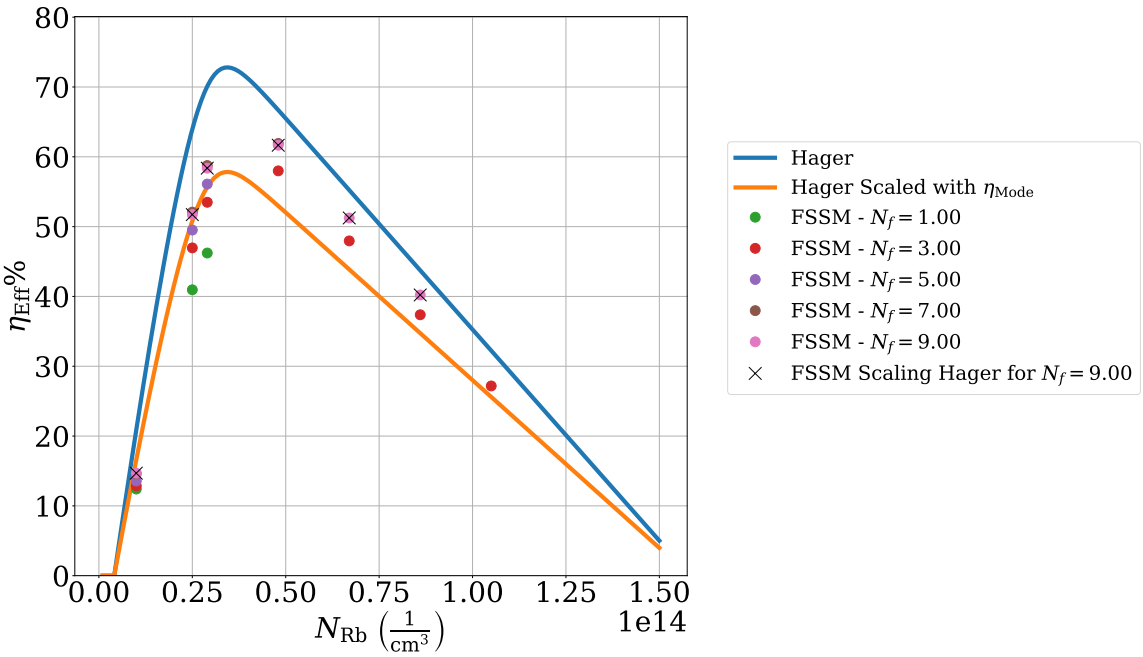

Figure 68. The efficiency of the laser resonator as a function of modifying the rubidium density of gain medium. Many different Fresnel numbers were calculated using the wave-optic gain simulation, as well as the unscaled Hager, and the scaled Hager using the predictive η_{Mode} for the geometric mode within the cavity.

highest Fresnel number runs in each study. These scaled Hager results based upon the gain wave-optics simulation, identify that the differences between the simplified model proposed by Hager and the gain wave-optics are primarily due to the limited fill of the cavity mode. The results also indicate that if a Mode-Fill Coefficient is known ahead of time and used in conjunction with Hager, the system efficiency including wave optics may be accurately predicted. The Mode-Fill Coefficient could be estimated with the bare cavity mode calculations mentioned in chapter III and then combined with Hager to quickly calculate the actual cavity modes in the presence of gain. These results also add assurance that as the Fresnel number increases the predicted Mode-Fill Coefficient in equation (347) should eventually be the Mode-Fill Coefficient of the cavity.

The gain parameter variation study lead to the development of of the Mode-Fill Coefficient used to modify the Hager Model to take into account the distribution

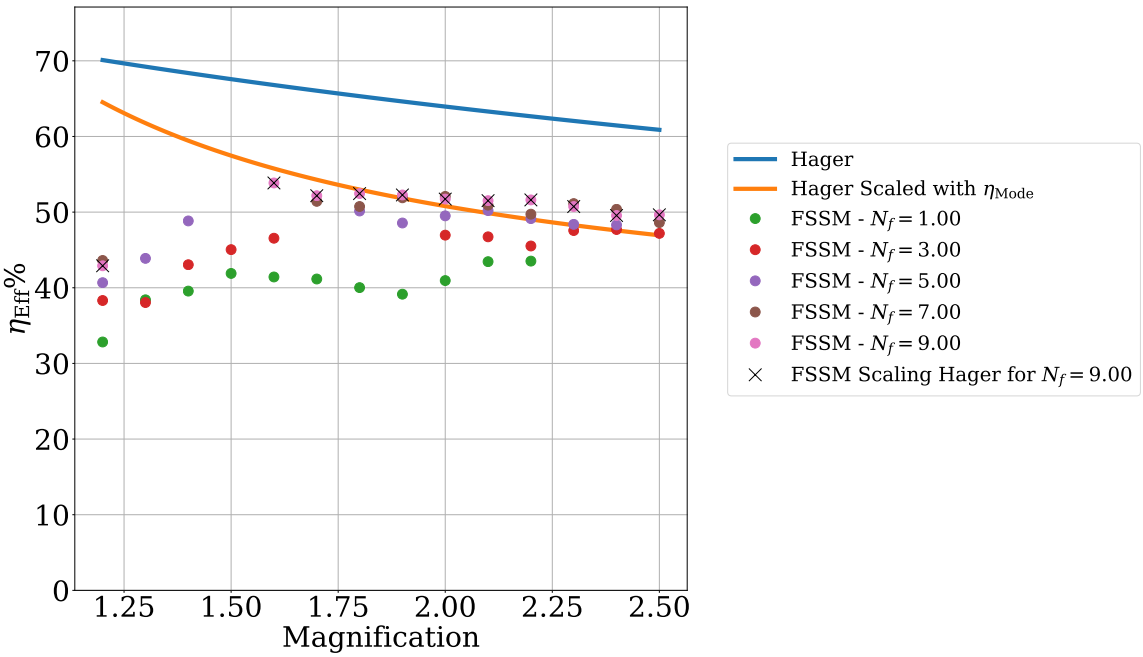

Figure 69. The efficiency of the laser resonator as a function of modifying the the geometric magnification of the unstable resonator. Many different Fresnel Numbers were calculated using the wave-optic gain simulation, as well as the unscaled Hager, and the scaled Hager using the predictive η_{Mode} for the geometric mode within the cavity.

of mode intensity throughout the gain cell. By assuming a geometric mode, the Mode-Fill Coefficient may be used to scale the original Hager model to appropriately handle the intracavity mode intensity coupling with the gain medium for an unstable resonator. Further predictions of the geometric Mode-Fill coefficient will be analyzed in the next two studies focusing on modifying the gain cell position within the cavity and in adjusting the length of the gain cell.

A Study Varying the Gain Cell Position

From the predictions given in section concerning the geometric mode in the cavity, the gain cell position should have a large effect in the cavity output. In order to test this hypothesis, a study analyzing gain cell position was conducted. The position of the gain cell was varied from the baseline case gain cell position while keeping the length of the gain cell constant for many different small mirror sizes corresponding to different Fresnel numbers. The large mirror and pump regions were scaled compared to the small mirror by a geometric magnification of $M = 2$.

The resulting efficiencies as functions of gain cell position for the various Fresnel numbers are shown in figure 70. The general trend seems to indicate that the efficiency of the cavity increases as the gain cell is moved closer to the back larger mirror of the cavity. The positive trend, in general, matches the positive trend associated with the geometric scaling coefficient, η_{mode}. However, the prediction of the scaling coefficient greatly overestimates the difference in efficiency change versus the prediction from the gain wave-optics calculation. Such a difference may be due to differences in the mode calculated with the gain wave-optics code and the geometric mode. The trend in efficiency as the position of the gain cell is moved is also more stair-stepped than the predictions give by the geometric mode scaling. The reason for such stair stepping may be attributed to the mode hopping as different laser cavity modes

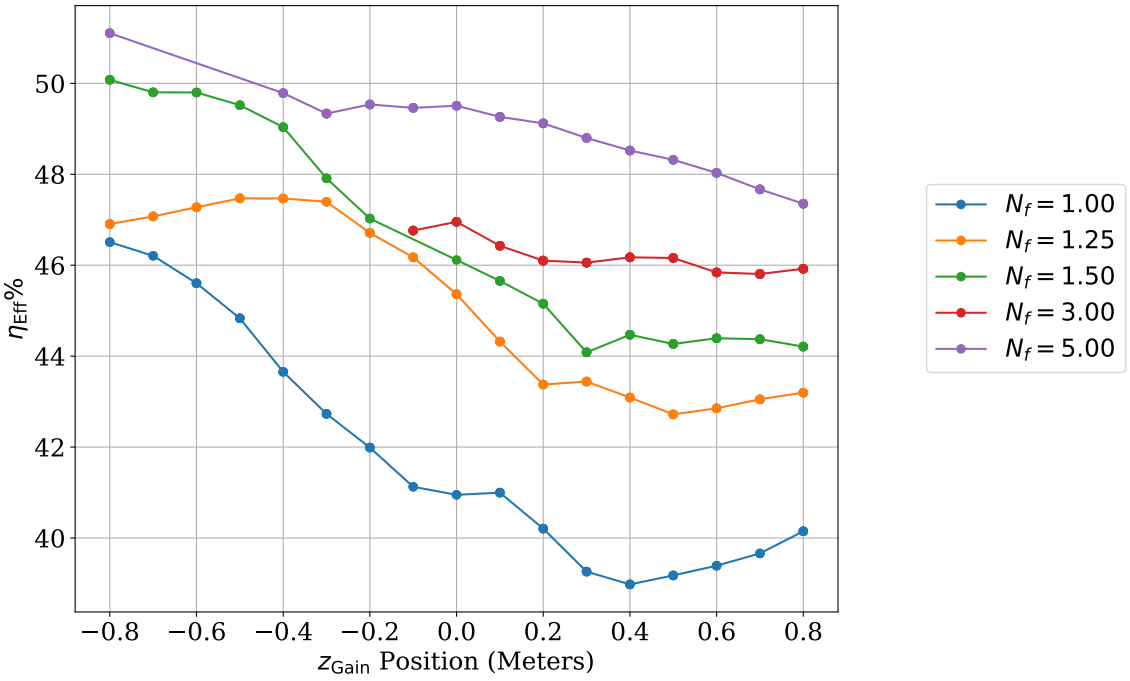

Figure 70. The efficiency of the laser resonator as a function of modifying the gain cell location for multiple cavity Fresnel numbers.

become dominant with the changing position of the gain cell in the resonator. As shown in figure 71, the VPIB of the laser cavity experiences an opposite trend than the efficiency change shown in figure 70. Both trends move in opposite directions and are consistent with the antagonistic relationship between beam quality and cavity efficiency originally presented in the Fresnel number study. The reasoning for the inverse trend is the same as in the Fresnel number study, as the gain cell cavity is moved toward the front mirror, a mode with better beam quality becomes dominant within the cavity. One should note that VPIB varies on the order of 10% as the gain cell's position moves from the front mirror to the back mirror, whereas, the efficiency varies approximately 6%. Dependent on the intended application of a high gain driven laser, a lower efficiency may be desired for better beam quality leading to an overall greater amount of power reaching a target in the farfield of the laser.

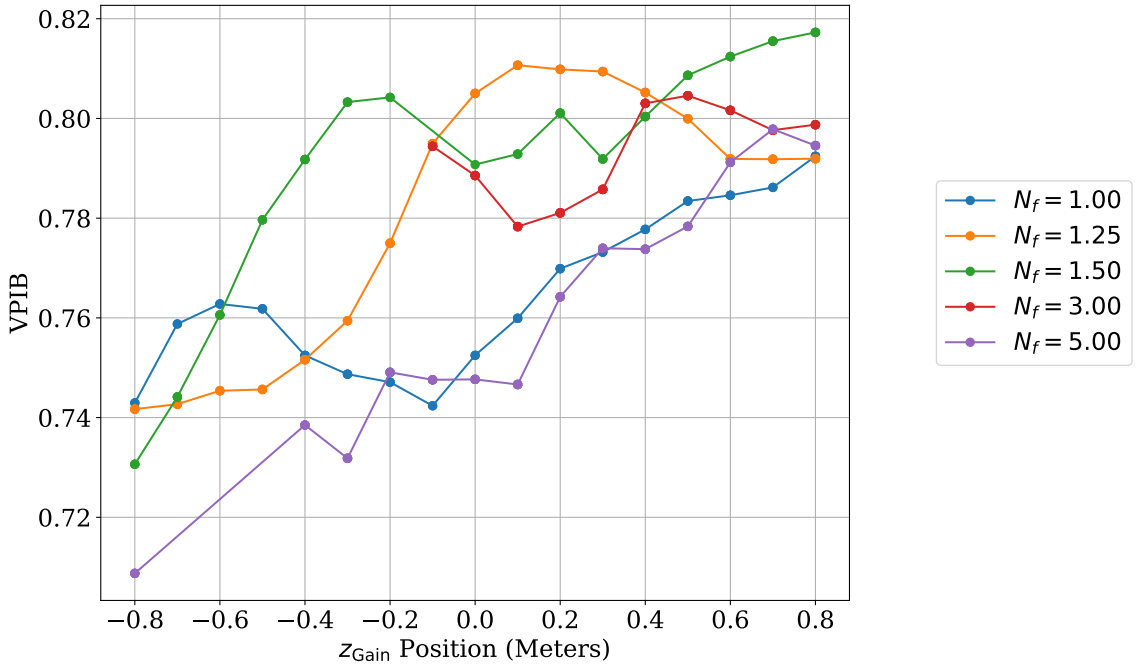

Figure 71. The VPIB of the laser resonator as a function of modifying the gain cell location for multiple cavity Fresnel numbers.

A Study Varying the Gain Cell Length

The predictions concerning the geometric mode in the cavity indicate that length of the gain cell length in the cavity will have a small effect in the cavity efficiency. In order to test these effects, a study looking at gain cell length was conducted. The gain cell had its length, Δz_{G}, and rubidium density varied. The rubidium density was varied to keep $n_{\text{Rb}}\Delta z_{\text{G}}$ constant for all the simulations. The total rubidium in the cavity was kept constant so that the total gain of the laser cavity would remain the same no matter how the gain cell length was changed. Different small mirror sizes were simulated corresponding to different Fresnel numbers as in previous study modifying gain cell position. The transverse scaling applied to the outcoupling mirror to modify Fresnel numbers was also applied to the large mirror and pump regions of the resonator.

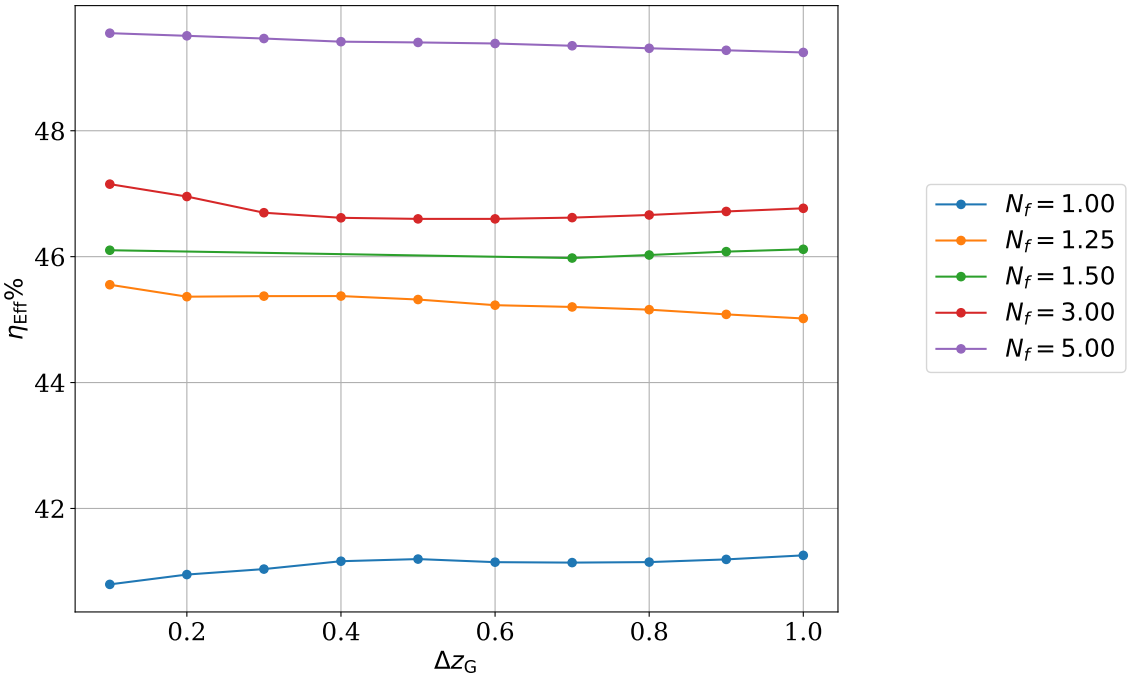

Figure 72. The efficiency of the laser resonator as a function of modifying the gain cell length for multiple cavity Fresnel numbers. The center of the gain cell was centered between the mirrors of the laser resonator.

The results measured for efficiency when the gain cell length was modified are shown in figure 72. The general trend seems to indicate that the efficiency of the cavity remains roughly flat as a function of length. The flat trend seems to match predictions of the the geometric scaling coefficient, η_{mode}, for the mirror position remaining in the middle of the cavity. The predictions shown in figure 60 show little change in the mode as $\frac{\Delta z_{\text{G}}}{\Delta z}$ is modified from 0.05 to 0.5, corresponding to the change in the gain cavity length investigated by the study.

The VPIB shown in figure 73, indicates growth of roughly 3-4% as the gain cell length is increased within the laser cavity. The growth of VPIB seems to indicate that as the gain cell is increased in length better beam quality tend to results. However, the trend in VPIB seems to be approaching a limit as the gain cell is increased in length throughout the cavity. The VPIB, as indicated in figure 53 also does not necessarily scale linearly with Fresnel number, but instead tends to hop around. The

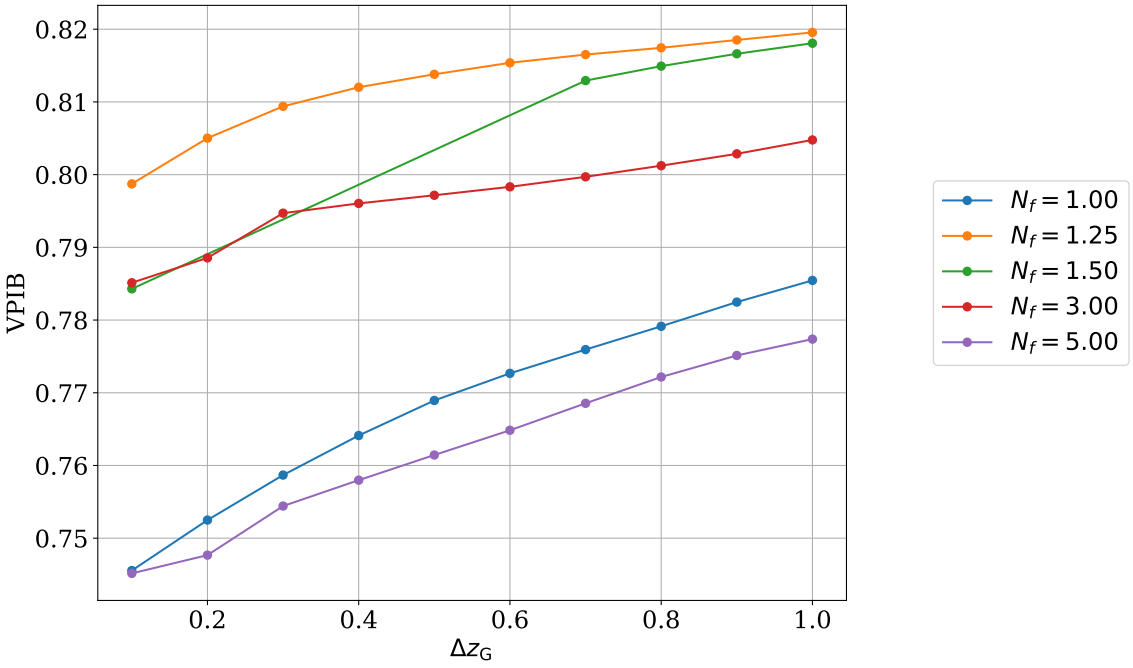

Figure 73. The VPIB of the laser resonator as a function of modifying the gain cell length for multiple cavity Fresnel numbers. The center of the gain cell was centered between the mirrors of the laser resonator.

smooth nature of figure 73 suggests that very little "mode hopping" is occurring in the laser resonator, and may represent a general strengthening of the mode associated the baseline case parameters for different Fresnel numbers.

The above calculations were repeated for different cavity positions within the system. A reference to a position in the back of the cell indicates that the back of the gain cell is located at the back mirror, no matter the cell length. Likewise, a reference to a position at the front of the cavity indicates that the gain cell is located at the front mirror, no matter the length of the gain cell. Figure 74 shows the efficiency as a function of gain cell length when the gain cell is located at the back mirror of the cavity. As predicted in figure 61, there is a noticeable decrease in efficiency of the system. However, the predicted decrease in figure 61 is less than the gain wave-optic simulation results in figure 74. The difference in trends may be due to figure 61

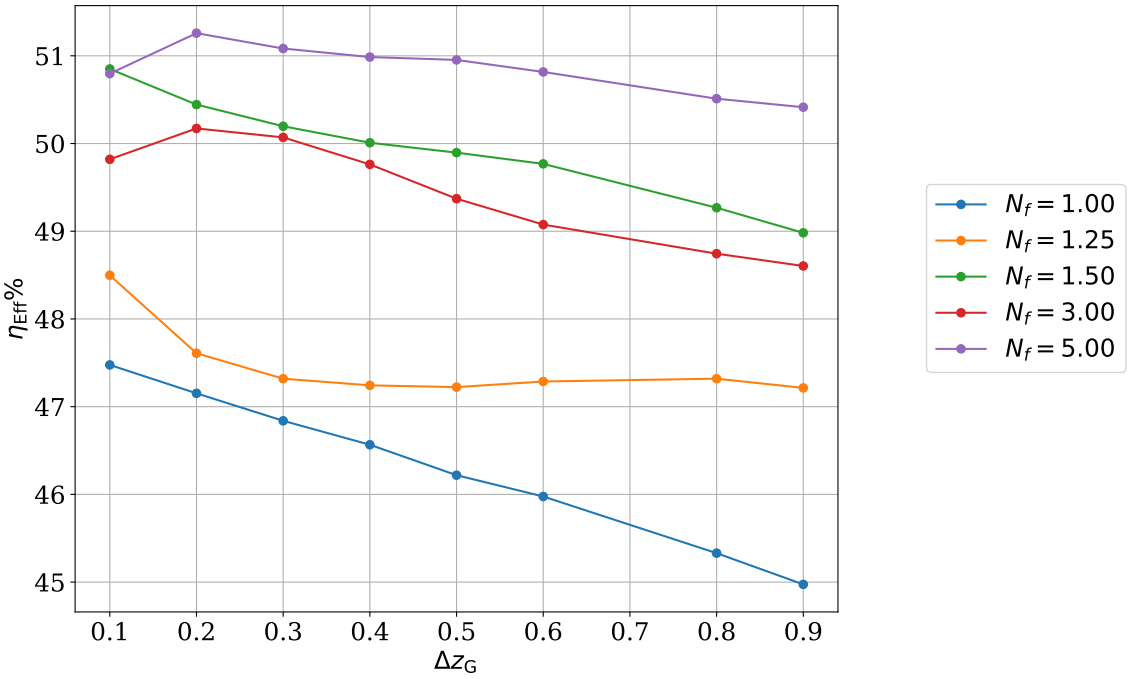

Figure 74. The efficiency of the laser resonator as a function of modifying the gain cell length for multiple cavity Fresnel numbers. The center of the gain cell was placed so that the back of the cell was located at the back mirror of the cavity.

describing the geometric mode of the cavity, while the simulations in figure 74 include diffraction in their calculation.

Figure 75 displays the same positive trend in figure 73. However, the positive trend is larger than observed for the gain cell length variation in the case where the gain cell is present in the middle of the cavity. The increase in VPIB is counter to the decrease in efficiency from figure 74 and represents a trade-space that must occur between beam quality and system efficiency.

The final scenario of the cavity is the gain cell positioned at the front of the cell. Converse to the results shown in figure 74, figure 76 indicates that when the gain cell is positioned at the front of the cavity, the efficiency increases as a function of cell length. The increase in efficiency for $N_f = 5$ also agrees with the general trend predicted in figure 62. However, figure 62 greatly overestimates the increase in efficiency found in the gain wave-optics calculation. The positive trend in efficiency also does not hold

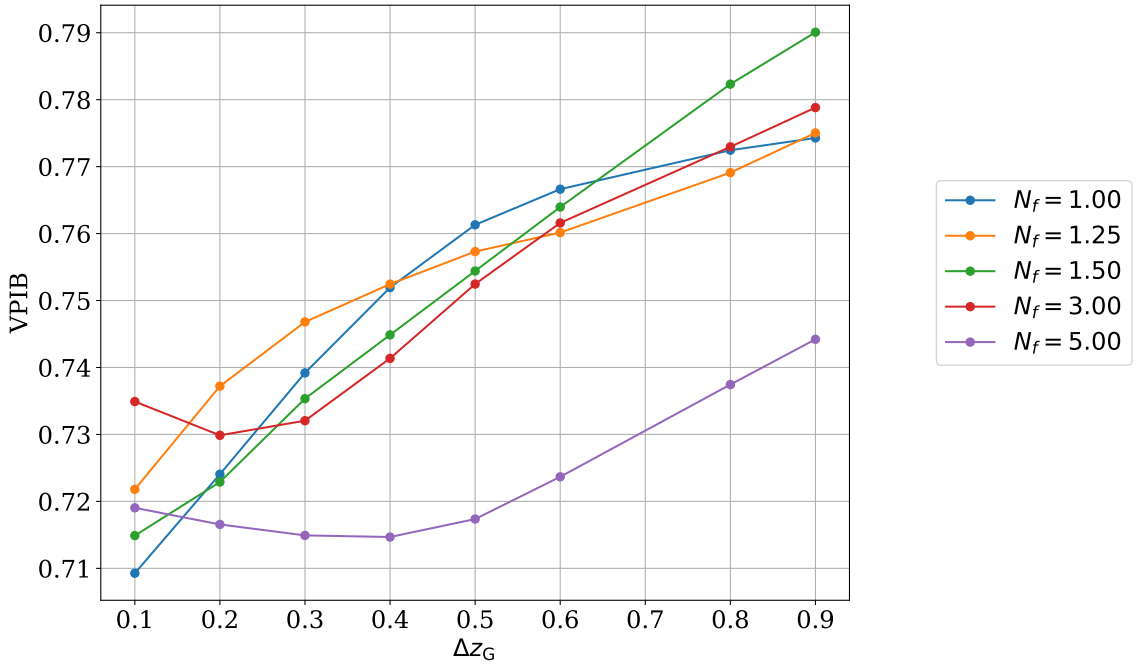

Figure 75. The VPIB of the laser resonator as a function of modifying the gain cell length for multiple cavity Fresnel numbers. The center of the gain cell was placed so that the back of the cell was located at the back mirror of the cavity.

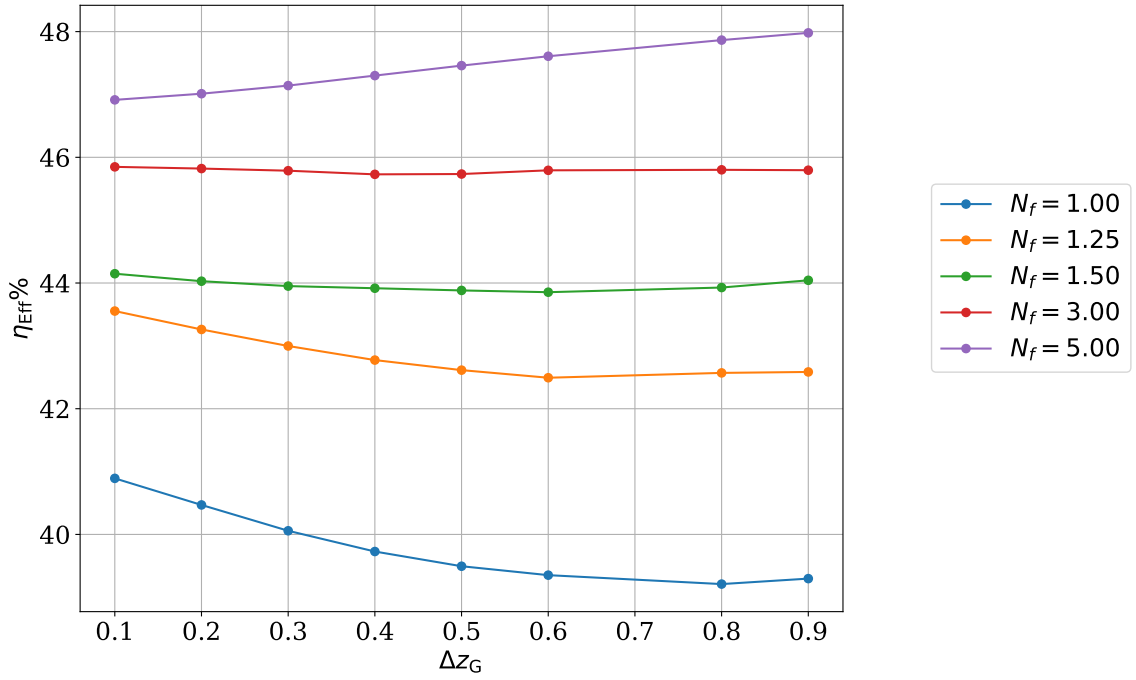

Figure 76. The efficiency of the laser resonator as a function of modifying the gain cell length for multiple cavity Fresnel numbers. The center of the gain cell was placed so that the back of the cell was located at the front mirror of the cavity.

for the lower Fresnel numbers. There is an observed cross-over occurring for $N_f = 3$ which has a relatively flat efficiency as a function of cavity length with lower Fresnel numbers having decrease in efficiency as gain cell length is increased.

Figure 77 agrees with the previous trends observed in figures 73 and 75. Increasing the length of the gain cell seems generally have a positive effect on the cell beam quality. However, the $N_f = 5$ does observe a growing beam quality followed by a decrease in beam quality for increasing gain cell length. The decrease in beam quality for this Fresnel number indicates that beam quality is inversely dependent on the efficiency of the cavity, however further study is required to verify such a relationship.

The length study indicated that the cell length of the cavity had minor impact on cavity efficiency roughly mirroring the trends predicted by the geometric Mode-Fill Coefficient. A decrease in efficiency was noted for increasing the gain cell length when the cell was positioned next to the back mirror. No change in efficiency as a function of cell length was observed when the gain cell was positioned at the center of the cavity. Finally, a slight increase was observed for the higher Fresnel number simulations when the gain cell was positioned at the outcoupler. Although gain cell efficiency wasn't heavily modified for any of the cases of modifying gain cell length, the beam quality had a positive correlation with an increase in gain cell length. This positive trend indicates that for system designs requiring good beam quality of a laser resonator, the gain cell needs to be as large as possible.

The four studies studies presented in the previous section give multiple trends for the cavity. By varying the Fresnel Number, efficiency was found to increase as a function of transverse cavity extent, while beam quality was observed to decrease with an increase in transverse laser cavity extent. The next study focused on varying gain parameters, such as intensity and rubidium density, and comparing the overall

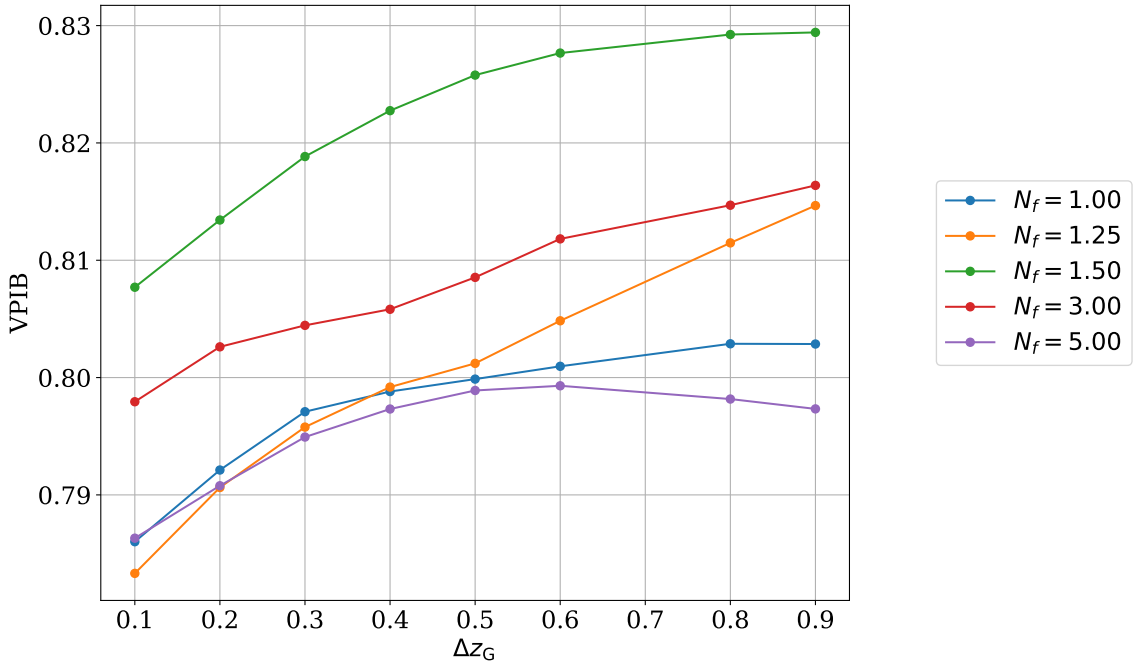

Figure 77. The VPIB of the laser resonator as a function of modifying the gain cell length. Many different Fresnel numbers were calculated using the wave-optic gain simulation. The center of the gain cell was placed so that the back of the cell was located at the front mirror of the cavity.

trends with the simplified Hager model. The agreement in trends was observed to be good, with the Mode-Fill Coefficient accounting for the differences between the efficiency predicted by the gain wave-optics calculation and the Hager model. The third study involved modifying the gain cell position within the laser resonator with the highest predicted efficiencies corresponding to a gain cell positioned near the back mirror of the cavity and the best beam quality corresponding to a gain cell positioned at the outcoupling mirror. Finally, the fourth study involved modifying the gain cell length, with a longer gain cell always having a positive effect on beam quality of the laser resonator. The response of the efficiency for high Fresnel numbers was roughly the same as the trends observed in figures 60 to 62.

V. Summary, Conclusions, and Future Work

The goal of the research was to provide better understanding of the interaction between high gain medium and the unstable laser resonator through numerical simulation. In order to accomplish the goal, numerous studies were conducted using a variety of numerical methods. This chapter focuses on the summarization of those results, followed by conclusions associated with those results, and ends with a discussion of future work that may follow on this research.

Summary of Work

Initially for the bare cavity all studies dealt with the comparison of three methods, two of them being different Fox and Li iteration propagation schemes and the third being DEM. The methods were used to calculate the least loss cavity modes for three different bare cavity configurations. The first configuration was the half symmetric stable configuration, chosen for its analytic solution. Agreement was established between all three methods and the mode calculated by all three methods matched the analytic solution with the addition of diffraction. The second cavity configuration involve recreating Yuanying's[28] predicted mode for his unstable resonator. The least loss mode predicted from all three methods matched each other, but did not match the results published in the Yuanying's original paper. Finally, the last cavity configuration simulated replicated the results from Siegman and Sziklas[31, 32] chosen positive branch confocal unstable resonator. Good agreement was achieved by all three numerical methods and also was achieved with the published results.

After the initial bare cavity mode comparisons, Fox and Li iteration using ASM and DEM were chosen to recalculate the eigenvalues previously calculated by Siegman[27]. Siegman's method for calculating the modes was implemented for the comparison.

The equivalent Fresnel number of the system was modified by scaling the radii of the front mirror in a positive branch confocal resonator. The back mirror radii was also modified by the same scaling with laser wavelength and the distance between mirrors held constant. Fox and Li iteration and DEM provided numerical predictions for the eigenvalues which compared well with each other but did not match the predictions of Siegman's method. However, by increasing the size of the back mirror to be 110% more then the predicted geometric magnification lead to good agreement between both methods and Siegman's method. After the eigenvalue analysis, Fox and Li iteration with ASM propagation was chosen to be the most promising candidate for calculating the mode of a resonator when gain is included.

ASM was re-derived as a FSSM to numerically simulate the propagation of the field within a gain medium. A rubidium optically pumped laser medium was used as the high gain laser medium with the rate equations determined from the kinetic processes associated with the $5^2S_{1/2}$, $5^2P_{1/2}$, and $5^2P_{3/2}$ levels. In the process of a calculation, a uniform pump would be scaled across the gain medium in a single direction. After the pump was "propagated", the steady-state population as a function of position within the gain cell was computed using corresponding laser and pump intensity through the cell. The laser was then propagated using FSSM, forward and backward in the cell. The entire simulation process was then iterated until the difference in laser intensity, gain, and pump intensity were negligible for each successive iteration.

Using the combined gain wave-optic simulation, four studies were performed to better understand the the relationship between the unstable resonator and high gain medium. All studies were based off of a single baseline case involving a positive branch confocal unstable resonator, with specific laser, pump, and gain criteria. Each of the studies involved modifying one of a few of the parameters from this baseline case.

The initial gain study focused on the change in efficiency, VPIB, as a function of Fresnel number. The study found that that efficiency generally increased as Fresnel number increased, but approached an asymptotic limit after a Fresnel number of 6. Conversely, VPIB decreased as Fresnel number increased, indicating that the cavity modes associated with lower Fresnel numbers have lower beam quality. The efficiency increase was assumed to be related to the laser cavity mode's coupling with the gain medium. Modifying Hager's simple model for steady-state DPAL operation with a Mode-Fill Coefficient. The assumed relationship between the intracavity intensity distribution and the gain medium was defined with the Mode-Fill Coefficient and was also measured for the study.

The second gain study focused on analyzing the efficiency of the system as a function of various gain parameters. The study involved using Hager's Model[10, 11] to compare against the gain wave-optics simulation. The trends predicted by Hager were also observed occurring for the gain wave-optics simulation, but had an obvious scaled difference. The scaled difference was attributed to the mode-fill coefficient discussed by Hager, η_{Mode}. The scaling between both methods of determining the laser cavity efficiency motivated an analytic determination of η_{Mode} for geometric modes. Good agreement was established between both the results of the gain wave-optic simulations and the scaled Hager Model was established.

The third gain study involved varying the position of the gain cell in the laser cavity and analyzing the effects on efficiency and VPIB. Efficiency was found to increase as the gain cell was moved to the back mirror in the unstable resonator and decrease as the cell was moved toward the output cell of the cavity. The trend of efficiency versus cell position was predicted by the η_{Mode} determination for geometric modes, but the predicted extent of the efficiency change was much larger than that observed in the gain wave-optic simulations. VPIB was observed to vary inversely

compared to efficiency with the best system beam quality observed with the gain cell positioned at the outcoupling mirror and the worst beam quality when the cell was placed next to the back mirror of the laser cavity.

The final gain study involved modifying the length of the gain cell and observing the effect on efficiency of the laser. The rubidium density was also modified so that the overall amount of rubidium contained within the gain cell would not change for different gain cell lengths. As predicted by the analytic geometric mode scaling, the efficiency calculated by the gain wave-optic simulation remained roughly constant no matter the length of the gain cell. However, the VPIB was observed to increase as the gain cell length was increased. The gain cell was then repositioned at the back of the laser resonator and the gain cell length variation was repeated, overall there was a decrease observed with the efficiency of the gain cell as the length was increased for a gain cell positioned at the back of the resonator. This trend was the similar to the trend predicted by the geometric η_{Mode}. As in study one, the beam quality acted inversely to the increase in efficiency with greater beam quality observed for longer gain cell lengths. Finally, the cell was positioned at the front of the laser resonator and the gain cell length was again varied. For large Fresnel numbers the efficiency of the system increased in a trend similar to that predicted by the geometric Mode-Fill Coefficient. However, the increase did not hold true for the smaller Fresnel number cases, with a decrease observed for Fresnel numbers less than $N_{f,x} = 3$. Beam quality, however, was observed to always increase, indicating that increasing cavity length will always have a positive effect on beam quality in the system.

Conclusions

Throughout all gain studies, the shape of the volumetric mode made a large difference in the field exiting the laser cavity. As indicated by the results of the

Fresnel number study in chapter IV, the overall efficiency of the cavity approaches the efficiency associated with the geometric mode as Fresnel number increases. However, as Fresnel number was increased there was a linear decrease in the beam quality of the output mode. For actual applications, these results suggest that when both power output and beam quality of the laser cavity are important the ideal Fresnel number for a laser cavity would be $N_{\mathrm{f},x} = 7$, representing the highest efficiency to be gained by increasing Fresnel number of the system, while also preventing the degradation of beam quality as Fresnel number increases. For situations in which beam quality is not a concern, the cavity Fresnel number should be at least $N_{\mathrm{f},x} = 7$ or larger to have maximum efficiency due to the volumetric modal distribution. For studies concerning gain medium parameters, the trends observed between gain wave-optic simulation and the ideal case[10, 11] where the intracavity laser intensity filled the gain medium equally were the same. This duplication of trends indicate that the volumetric shape of the mode acts as a scalar multiple to the ideal case.

Compared to an ideal case for which the mode was assumed to fill the cavity, the actual volumetric fill of the positive branch confocal unstable resonators mode could have either small or large degradations on cavity efficiency. The largest degradation occurred for laser cavity geometries with the gain cell positioned closest to the outcoupling mirror for the geometric mode. Likewise, the least amount of efficiency degradation was associated with the gain cell of a system located at the opposite mirror of the cavity. Conversely, beam quality tended to be best for a gain cell position located at the outcoupling mirror and worse for a gain cell positioned at the back mirror. Therefore, a suggestion from this study for future laser design is that if adaptive optics are present in a system decreasing the necessity of beam quality, the ideal location of the gain cell would be in front of the back mirror of the cavity to ensure the greatest laser resonator efficiency. However, if adaptive optics are not available,

the laser cavity needs to be evaluated with a gain wave-optics code to determine the best efficiency and beam quality trade-off for the system.

Although position of the gain cell had a large influence on the cavity efficiency, varying the gain cell length was found to have very little effect on the efficiency of the cavity for the case of a cavity position located in the middle of the laser resonator mirrors. However, increasing the gain cell length without changing the overall amount of rubidium within the gain cell did increase beam quality in the laser cavity resonator output. These results indicate that if beam quality is a concern for the laser system, the cavity length should be at least half the size of the laser resonator to ensure maximum quality in the output beam.

A simple model based on the definition of the mode-fill coefficient, η_{Mode}, found in equation (347) and illustrated in figures 61 and 62, was used to further explore laser efficiency as it depends on gain cell position and length. For cases where the gain cell was located at the back and front mirrors of the laser resonator, increasing the gain cell length reduced the efficiency for the gain cell at the back mirror and increased the efficiency for the gain cell at the front mirror. When beam quality is not a concern, the gain cell should be positioned at the back mirror with a gain cell length no more than 10% of the entire laser cavity length to ensure maximum system efficiency.

Every conclusion mentioned should be tempered with the two caveats mentioned in the introduction and in chapter IV. The first is that the gain wave-optics simulations were performed with a uniform pump which did not experience wave-optic effects in the medium. A real-world system would not have such an ideal pump configuration. The second caveat is that Amplified Spontaneous Emission (ASE) was also ignored within the wave-optic simulations. ASE may have a large impact on the conclusions mentioned above, specifically those indicating that limiting the length of the gain cell within the laser resonator increases system efficiency because the effects of ASE

will be strongest when the gain cell length is on the same order or smaller than the transverse dimensions of the gain cell.

Future Work

The research performed has some very natural follow-ons, the first being a further analysis of the shape of the gain region and beam quality and mode output. The gain region shape may be modified by the pump placed into the cavity. A survey of the laser cavities with a variety of pumped area sizes would be helpful in further understanding the laser intensity coupling with the gain medium. Other distributions of the uniform pump should also be considered, such as a pumped region that is circular in the cavity. Another important series of cases involve scenarios where the pump is no longer uniform, starting with a transverse pump intensity distribution which Gaussian in nature. Other pump configurations with transverse pump intensities distributed on the mirror edges should also be analyzed.

After the initial uniform pump configurations are completed, the simulations need to be performed with the pump treated with a full gain wave-optic simulation in order to have more realistic pump configuration. Following the inclusion of wave-optic treatment of the pump means that the initial pump intensity should be treated with a randomized phase. To better model a realistic system, the pump should be modeled with multiple Gaussians in the plane transverse to the direction of propagation. Multiple simulations should be performed with each of the Gaussians having a randomized tilt and defocus to establish a statistical surrogate pump that could represent a real optically pumped system.

Currently, the laser extent experiences a highly absorptive transverse boundary condition due to the limited transverse extent of the pump. However, other boundary

conditions should be attempted to include reflective boundary conditions to represent the edges of a duct.

Further studies involving cavity geometry should be completed. Specifically, looking at cavity efficiency and beam quality as a function of the back mirror size for many different front Fresnel numbers. Investigating configurations that are not on the positive branch confocal unstable resonator should also be attempted in order to better understand alternate cavity configurations which may have better efficiencies compared to the positive branch confocal unstable resonator.

Increasing the fidelity of the gain wave-optic simulation should also be attempted in future work. ASE should be added to the physics of the model to test whether the conclusions in this research remain true for more real-world simulations, specifically the increase in efficiency as the length of the gain cell is shrunk, which has the highest liklihood of being effected by ASE in a real-world high gain system. Heat flow from the pumping/lasing process should be used to update the gain medium calculations. Eventually, the heat flow should be modeled in a Navier-Stokes method to understand the turbulence generated by the pump/lasing cycle within the gas which makes up the gain fluid. Such a task would require the inclusion of Computational Fluid Dynamics (CFD) of the laser medium as an additional step in figure 38.

Appendix A. The Circular Mirror Studies

Originally, the gain wave-optic studies were intended to have circular mirrors similar to the bare cavity calculations performed in chapter III. However, the required computational grid used for FSSM was Cartesian. The rectangular grid structure imposed on the circular mirror did not make a large difference for the bare cavity simulations, but became problematic for simulations including gain. For low Fresnel numbers, $N_f < 2$ simulations were able to converge, however the modes for larger Fresnel numbers tended to not have simulation residuals converge. Therefore, after the completion of a few low Fresnel number studies for circular resonator mirrors, the baseline case was modified to use rectangular mirrors. The following contents of this appendix are the original low Fresnel number studies completed for the circular mirrors .

Circular Baseline Case Geometry

From figure 42 and figure 43, the circular baseline case was the same as the baseline case defined in chapter IV, except for the circular mirrors and lower Fresnel number, $N_f = 1$, associated with the cavity. The circular mirrors did not vary in the azimuthal direction, but did have a rectangular gain medium geometry. The gain medium and pump were limited to be the size of the back mirror in the transverse

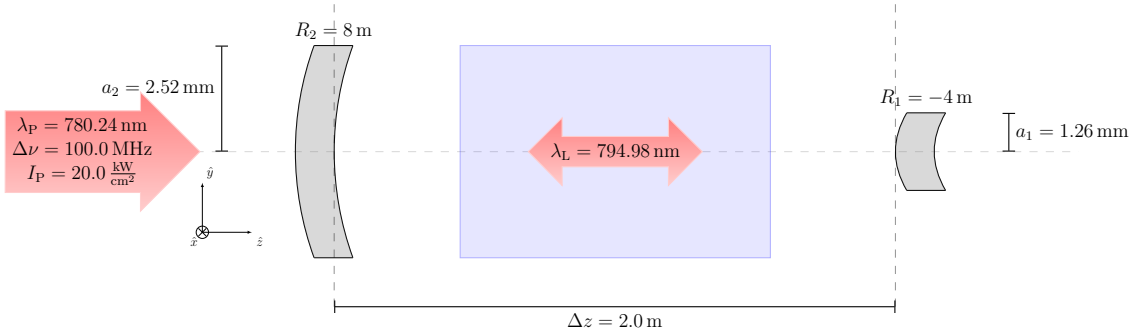

Figure 78. Diagram of the laser, pump, and lasing cavity parameters.

direction outside of which the cavity was treated as a vacuum. The optical grid in the baseline case had a sampling of $N_x, N_y = 256, 256$, with a total grid size of $\Delta x_{\text{Grid}}, \Delta y_{\text{Grid}} = 1.61\,\text{cm}, 1.61\,\text{cm}$. The gain medium had a sampling of $N_z = 200$, with two more planes included for the optical grid to represent the mirror planes. The gain region and optical grid had the same resolution of $\delta x, \delta y = 0.062\,\text{mm}, 0.062\,\text{mm}$. The bare cavity output mode's phase and intensity are shown in figure 80. Both the phase and intensity of the circular mode are more intuitive in mode shape versus the bare cavity case for the rectangular resonator. The mode is circular in nature with a lack of azimuthal dependence.

Including the gain lead to the transverse xy slice of the $+\hat{z}$ field intensity and phase located at the outcoupling mirror to be modified to the contour plots shown in figure 81. The output field now has a rectangular features caused by the cavity mode's propagation through a transversely rectangular gain medium.

The farfield intensity and phase calculated with are shown in figure 82. The rectangular nature displayed by the output mode of the field in figure 81 seems to completely disappear within the farfield of the cavity, indicating the rectangular intensity of the cavity was actually a near field feature added by the rectangular nature

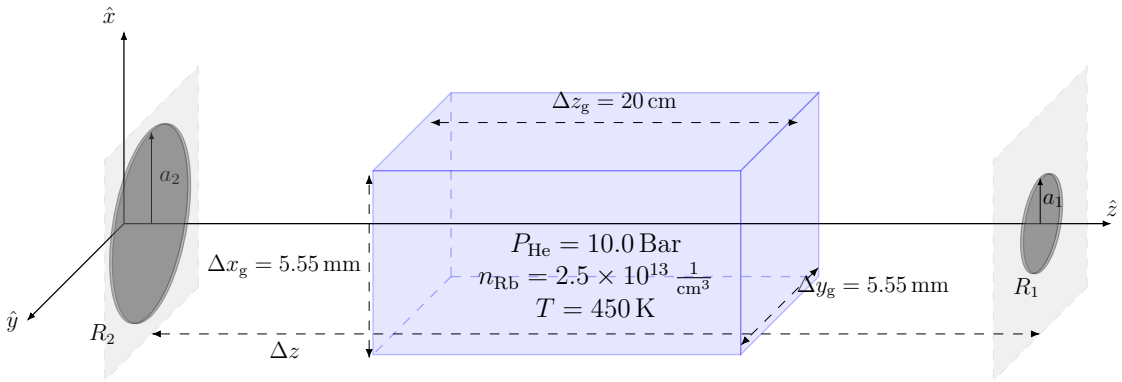

Figure 79. Diagram of the lasing medium parameters in the circular mirror lasing cavity.

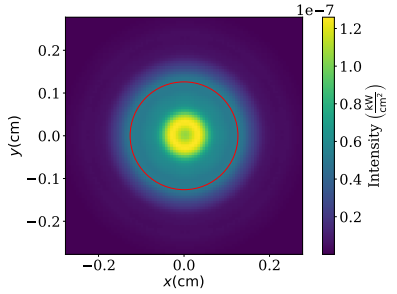

(a) Normalized Output Mode Intensity

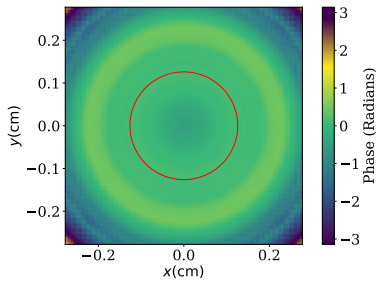

(b) Output Mode Phase

Figure 80. The normalized intensity and phase for the baseline configuration located at the smaller outcoupling mirror in the $+\hat{z}$ location for a bare cavity. The red line indicates the edge of the outcoupling mirror, the transverse field in the red circle is not transmitted out of the cavity.

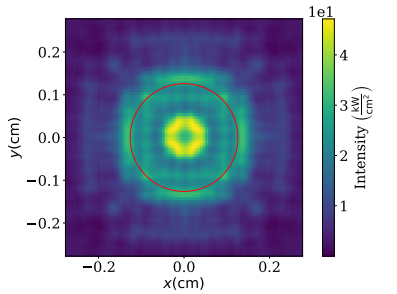

(a) Output Mode Intensity

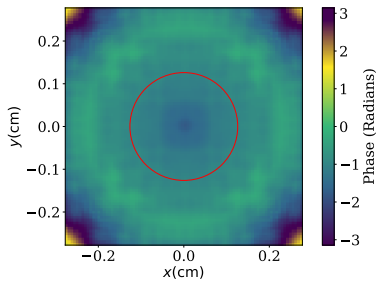

(b) Output Mode Phase

Figure 81. The intensity and phase for the baseline configuration located at the smaller outcoupling mirror in the $+\hat{z}$ location. The red line indicates the edge of the outcoupling mirror, the transverse field in the red circle is not transmitted out of the cavity.

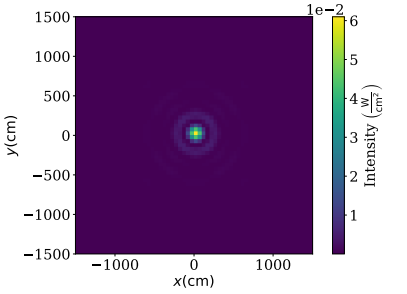

(a) Farfield Intensity

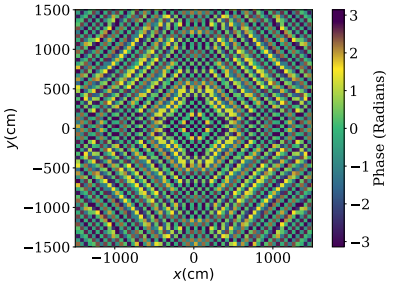

(b) Farfield Phase

Figure 82. The intensity and phase for the baseline configuration located at a farfield location approximately $10000\,\mathrm{m}$ from the laser cavity exit.

of the gain medium. Such a near field distribution will have large effects on the output efficiency of the cavity.

A Study Varying Gain Parameters

The study discussed in chapter IV concerning gain parameter variation for the rectangular mirror case was completed for low Fresnel numbers with the circular mirrors. Prior to looking at the results of the study, the Volumetric-Fill Coefficients must be recalculated using the geometric mode volume associated with circular mirrors in a rectangular gain medium.

The Circular Geometric Mode.

Based upon section , the Mode-Fill coefficient is still consistent with equation (347), however the Volumetric-Fill coefficient is modified because the geometry is now circular path in the cavity, helps identify the modes of the intensity of the cavity have volumes

$$V_{I^-} = \frac{\pi}{12}\left(\frac{\Delta z_{\mathrm{G}}}{\Delta z}\right)^2\left(1-\frac{1}{M}\right)^2 4a^2\Delta z_{\mathrm{G}} + \frac{\pi}{4}\left[\frac{1}{M}+\frac{\Delta z_1}{\Delta z})\left(1-\frac{1}{M}\right)\right]\left(\frac{\Delta z_{\mathrm{G}}}{\Delta z}\right)\left(1-\frac{1}{M}\right)4a^2\Delta z_{\mathrm{G}} + \frac{\pi}{4}\left(\frac{\Delta z_{\mathrm{G}}}{\Delta z}\right)^2\left(1-\frac{1}{M}\right)^2 4a^2\Delta z_{\mathrm{G}} \quad (348)$$

and

$$V_{I^+} = \frac{\pi}{4}4a^2\Delta z_{\mathrm{G}}\,. \quad (349)$$

Therefore, the Volumetric-Fill Coefficients are identified as

$$\Gamma^{+} = \frac{\pi}{12}\left(\frac{\Delta z_{\mathrm{G}}}{\Delta z}\right)^{2}\left(1-\frac{1}{M}\right)^{2} + \frac{\pi}{4}\left[\frac{1}{M}+\frac{\Delta z_{1}}{\Delta z})\left(1-\frac{1}{M}\right)\right]\left(\frac{\Delta z_{\mathrm{G}}}{\Delta z}\right)\left(1-\frac{1}{M}\right) + \frac{\pi}{4}\left(\frac{\Delta z_{\mathrm{G}}}{\Delta z}\right)^{2}\left(1-\frac{1}{M}\right)^{2}, \quad (350)$$

and

$$\Gamma^{+} = \frac{\pi}{4}. \quad (351)$$

Using the new cavity Volumetric-Fill Coefficients and (347), η_{Mode} may be recalculated for the new mode geometry.

As performed in gain parameter study completed for the rectangular mirror resonator, figure 83 represents the Mode-Fill Coefficient for the gain cell being an equal distance between each mirror, figure 84 represents the Mode-Fill Coefficient for the gain cell being positioned at the back mirror, and figure 85 represents the Mode-Fill Coefficient for the gain cell being positioned at the outcoupling mirror. All of the Mode-Fill Coefficients seem to have the same overall trend as those presented in the rectangular gain parameter study. However, the maximum Mode-Fill Coefficient is no longer equal to one. The difference is due to the size of the back mirror not matching the transverse area of the the pump of the cavity.

Much as the gain study for rectangular mirrors, this study measured system efficiency as a function of input pump intensity, temperature, pressure, and rubidium density. The results are shown in figure 86, figure 87, figure 88, and figure 89 respectively. All the trends observed in these results were previously observed and documented for the rectangular cavity. However, the overall efficiencies of these scans are lower representing due to the smaller Mode-Fill Coefficients versus the results pre-

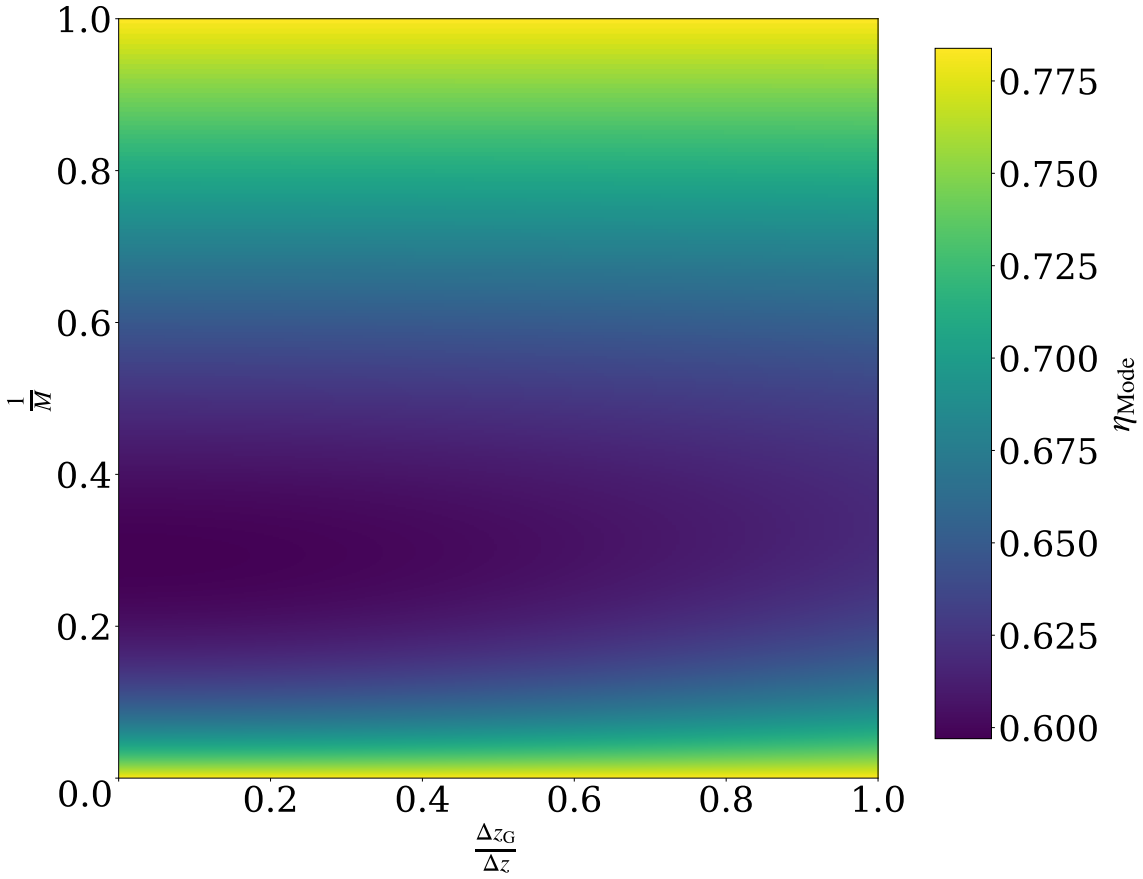

Figure 83. The Mode-Fill Coefficient, given by equation (347), as a function of gain and inverse geometric magnification. The gain cell is centered between both mirrors.

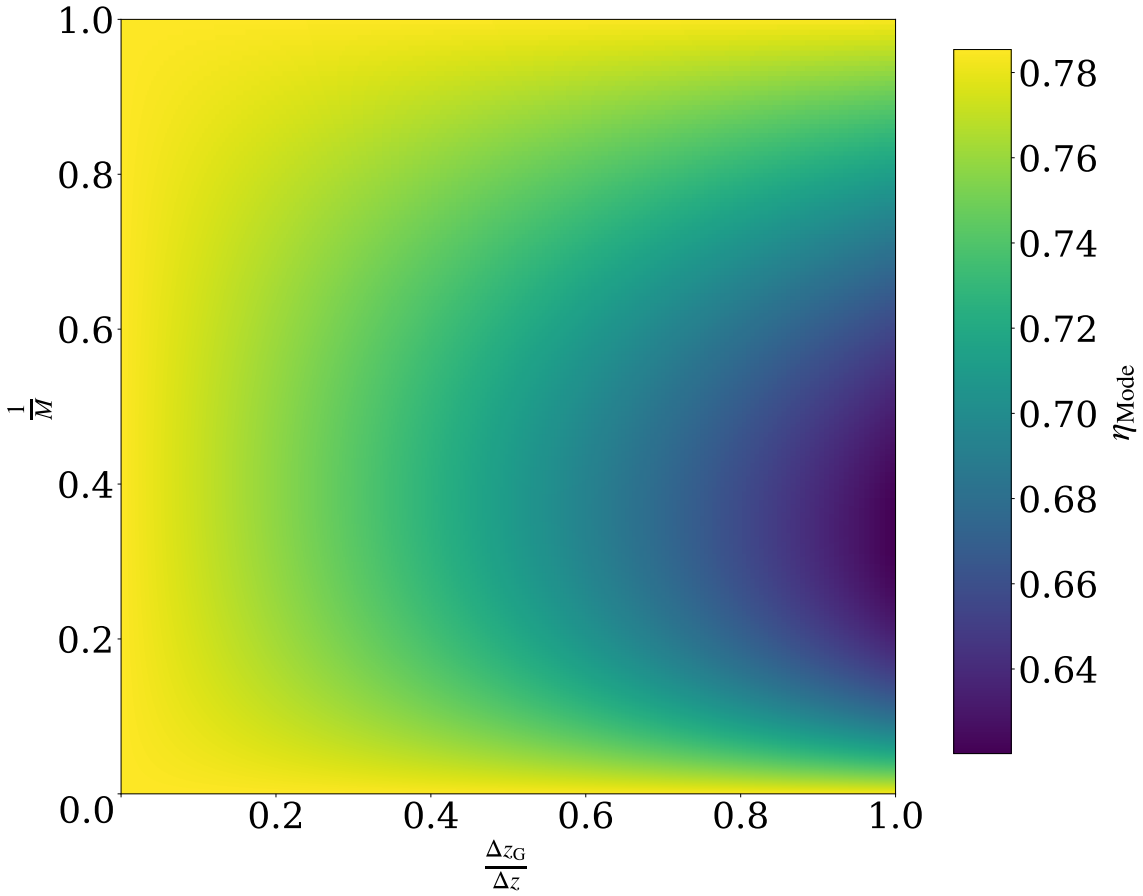

Figure 84. The Mode-Fill Coefficient, given by equation (347), as a function of gain and inverse geometric magnification. The gain cell is located at the back mirror.

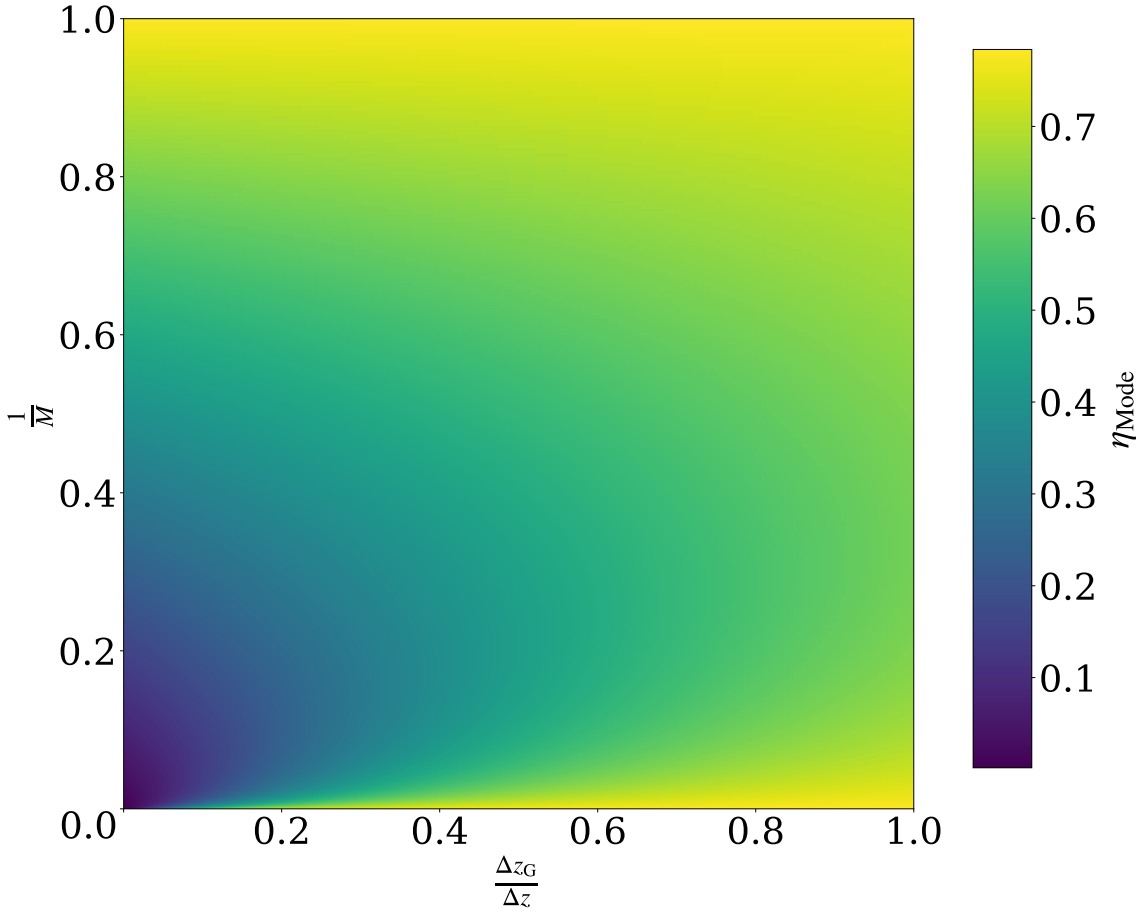

Figure 85. The Mode-Fill Coefficient, given by equation (347), as a function of gain and inverse geometric magnification. The gain cell is located at the front mirror.

sented in the rectangular gain parameter study. The agreement between the scaled Hager model and the gain wave-optic simulations seems to be less complete. The difference may be explained by looking at figure 81a. The transverse mode is not the circular geometric mode expected from a positive branch confocal unstable resonator, the actual mode is much larger indicating that the geometric mode's Volumetric-Fill Coefficients are smaller then the Volumetric-Fill Coefficients associated with the real cavity mode.

As previously observed in the rectangular gain parameter study, there is also excellent agreement between the Hager efficiency scaled by the measured mode coefficient and the gain wave-optics calculated efficiency of the resonator. This agreement further supports the use of the calculated geometric Mode-Fill coefficient in determining the system efficiency as Fresnel number increases.

A Study Varying the Gain Cell Position

Much as in the rectangular gain cell position study, a study of efficiency and VPIB in relation to gain cell position was accomplished for low Fresnel numbers with circular mirrors. The results measured for efficiency when the gain cell position was modified are shown in figure 90 and the VPIB when the gain cell position was modified are shown in figure 91. The same trends were observed as were observed as in the rectangular position study with the largest efficiency and lowest VPIB occurring when the gain cell is positioned next to the back mirror. The opposite being true when the gain cell is positioned next to the outcoupling mirror. The variance of the VPIB and efficiency for the circular mirror layout versus the rectangular cavity layout are due to the circular mirror study being limited to lower Fresnel numbers due to convergence.

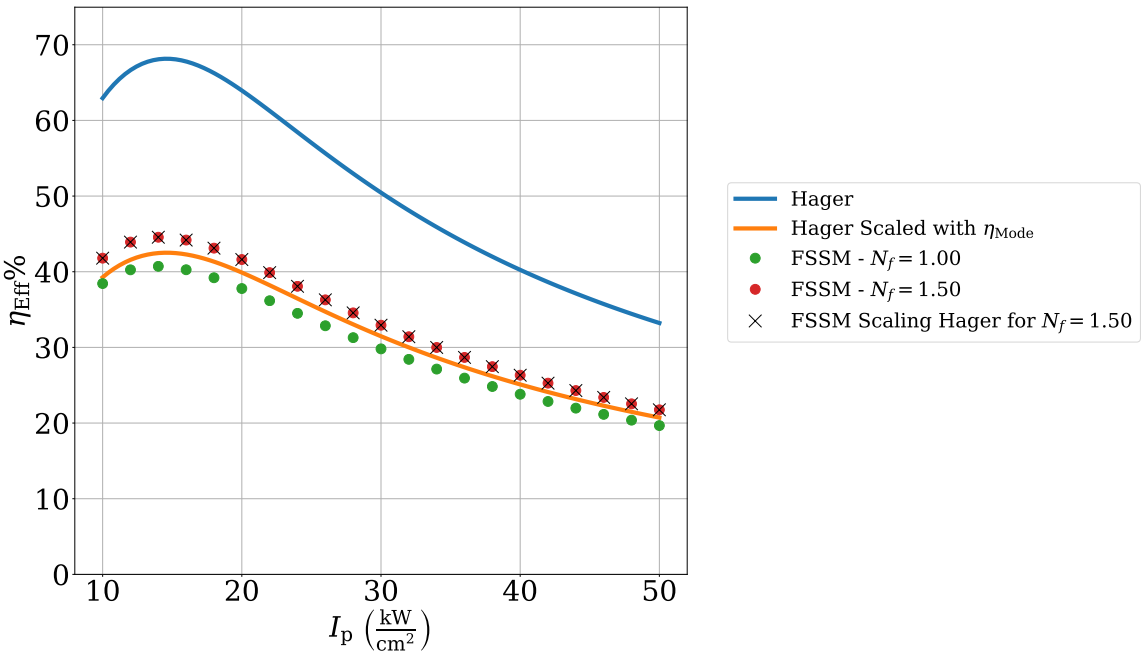

Figure 86. The efficiency of the laser resonator as a function of modifying the input pump intensity. Many different Fresnel numbers were calculated using the wave-optic gain simulation, as well as the unscaled Hager, and the scaled Hager using the predictive η_{Mode} for the geometric mode within the cavity.

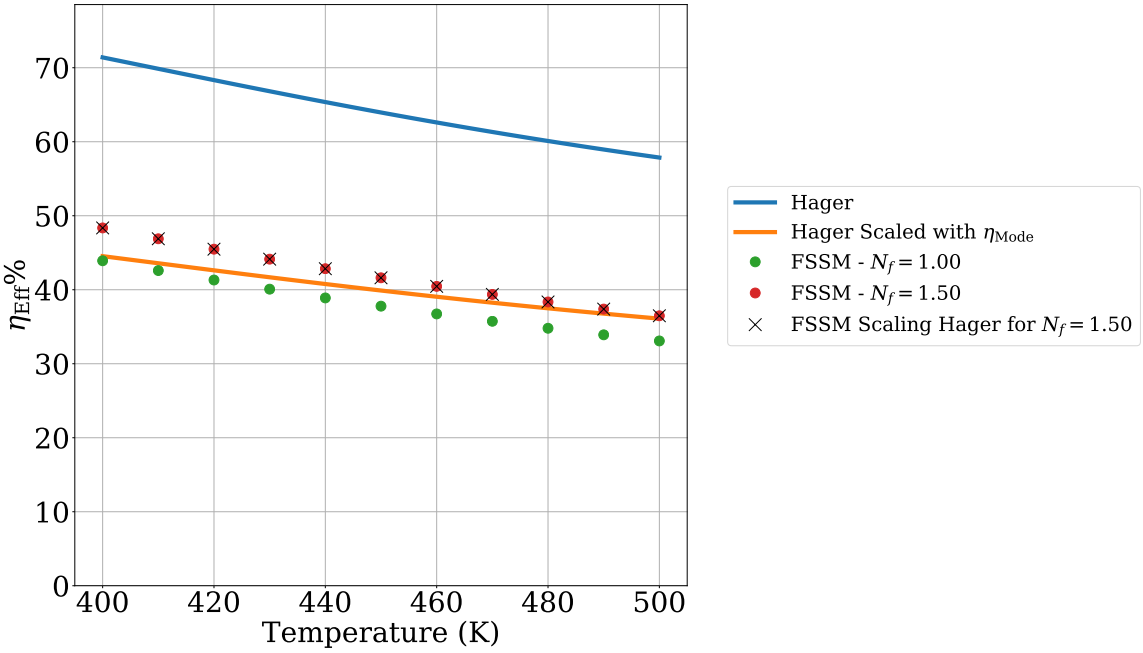

Figure 87. The efficiency of the laser resonator as a function of modifying the temperature of the cavity. Many different Fresnel numbers were calculated using the wave-optic gain simulation, as well as the unscaled Hager, and the scaled Hager using the predictive η_{Mode} for the geometric mode within the cavity.

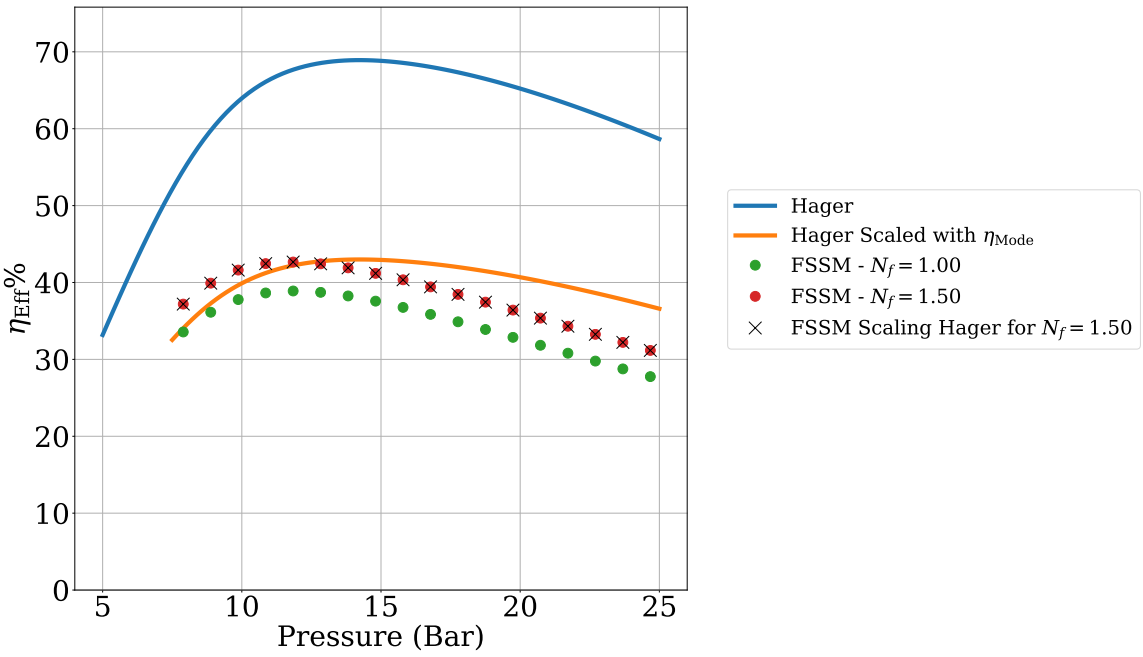

Figure 88. The efficiency of the laser resonator as a function of modifying the helium pressure of the cavity. Many different Fresnel numbers were calculated using the wave-optic gain simulation, as well as the unscaled Hager, and the scaled Hager using the predictive η_{Mode} for the geometric mode within the cavity.

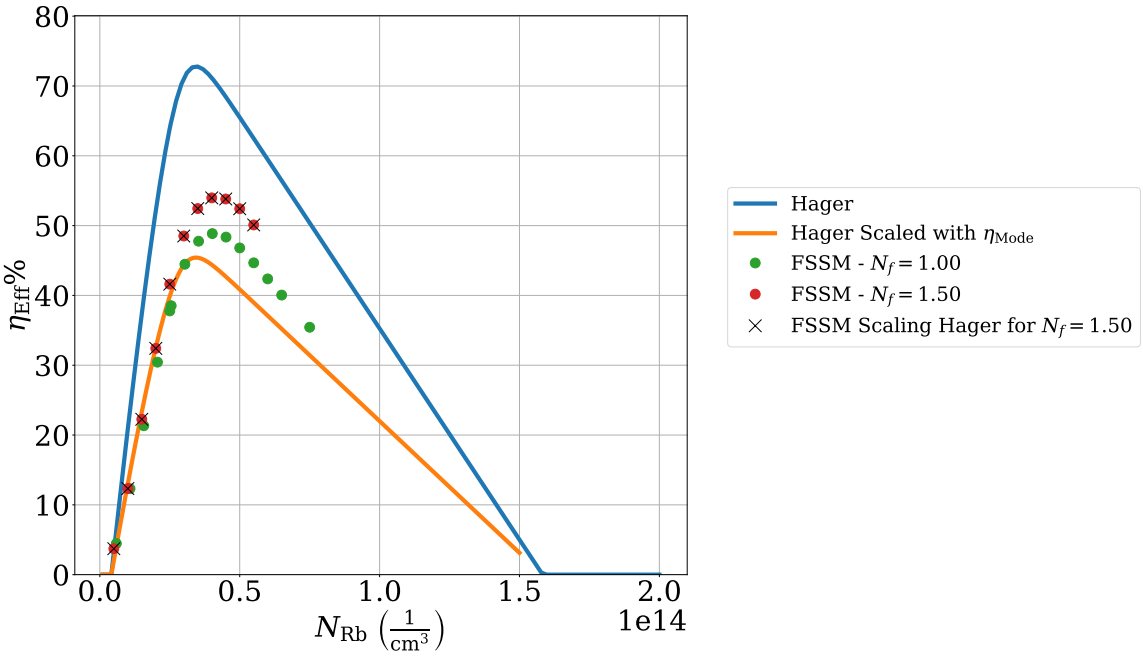

Figure 89. The efficiency of the laser resonator as a function of modifying the rubidium density of gain medium. Many different Fresnel numbers were calculated using the wave-optic gain simulation, as well as the unscaled Hager, and the scaled Hager using the predictive η_{Mode} for the geometric mode within the cavity.

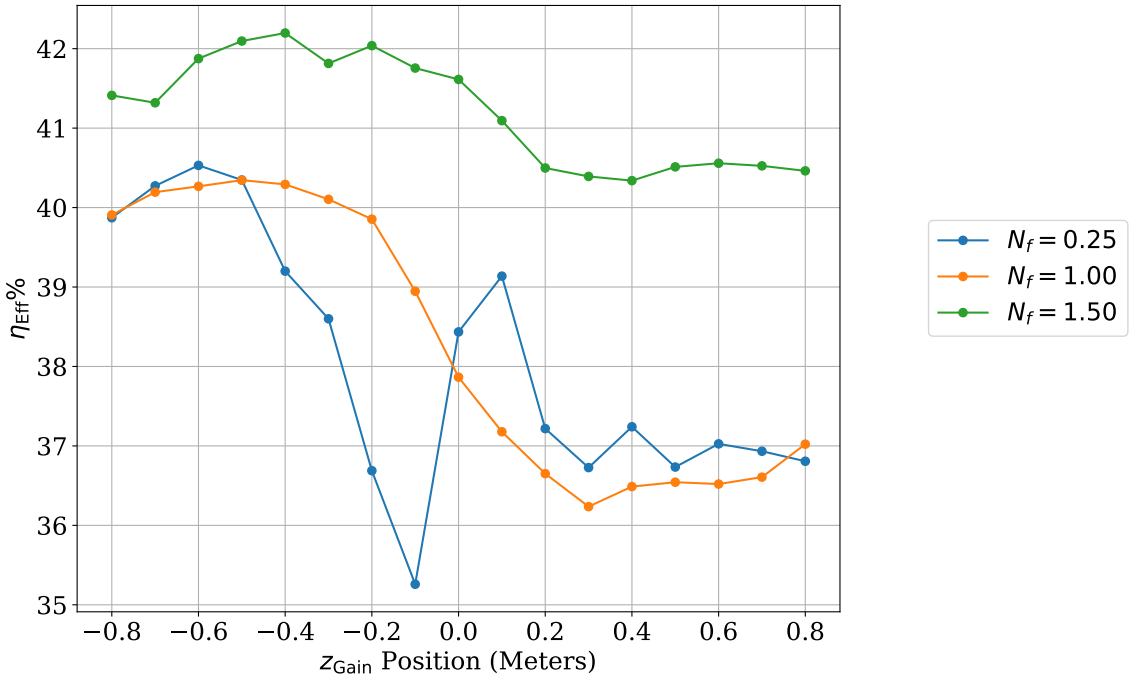

Figure 90. The efficiency of the laser resonator as a function of modifying the gain cell location. Many different Fresnel numbers were calculated using the wave-optic gain simulation.

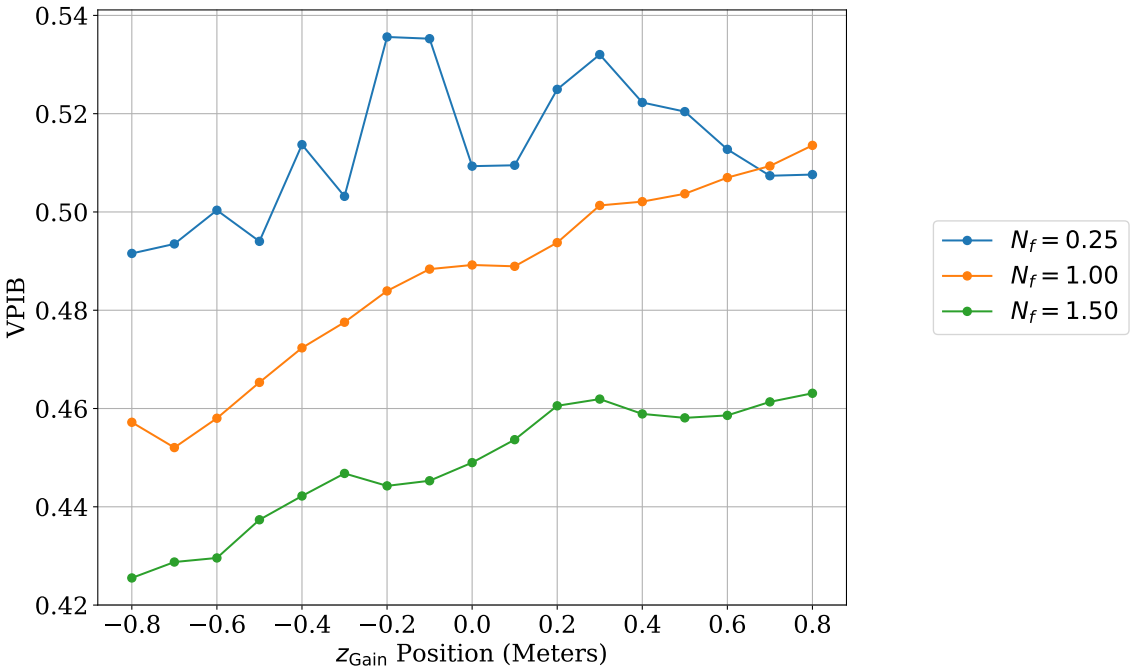

Figure 91. The VPIB of the laser resonator as a function of modifying the gain cell location. Many different Fresnel numbers were calculated using the wave-optic gain simulation.

Bibliography

1. USAF Chief Scientist. Technology Horizons: A Vision for Air Force Science & Technology During 2010-2030. *Technology Horizons*, 1(May):171, 2010.

2. Glen P. Perram. *An Introduction to Laser Weapon Systems*. Directed Energy Professional Society, 2009.

3. A. L. Schawlow and C. H. Townes. Infrared and optical masers. *Physical Review*, 112(6):1940–1949, 1958.

4. P. Rabinowitz, S. Jacobs, and G. Gould. Continuous Optically Pumped Cs Laser. *Applied Optics*, 1(4):513, 1962.

5. A. Sharma, N. D. Bhaskar, Y. Q. Lu, and W. Happer. Continuous-wave mirrorless lasing in optically pumped atomic Cs and Rb vapors. *Applied Physics Letters*, 39(3):209–211, 1981.

6. B.V. Zhdanov, M.K. Shaffer, and R.J. Knize. Diode pumped alkali lasers: History, current state and perspectives. In *2011 Conference on Lasers and Electro-Optics Europe and 12th European Quantum Electronics Conference (CLEO EUROPE/EQEC)*, volume 44, pages 1–1. IEEE, may 2011.

7. William F. Krupke. Diode-pumped alkali laser, 2003.

8. William F. Krupke, Raymond J. Beach, V. Keith Kanz, and Stephen A. Payne. Resonance transition 795-nm rubidium laser. *Optics Letters*, 28(23):2336, dec 2003.

9. Raymond J. Beach, William F. Krupke, V. Keith Kanz, Stephen A. Payne, Mark A. Dubinskii, and Larry D. Merkle. End-pumped continuous-wave alkali vapor lasers: experiment, model, and power scaling. *Journal of the Optical Society of America B*, 21(12):2151, 2004.

10. Gordon D. Hager and Glen P. Perram. A three-level analytic model for alkali metal vapor lasers: part I. Narrowband optical pumping. *Applied Physics B*, 101(1-2):45–56, oct 2010.

11. Gordon D. Hager and Glen P. Perram. A three-level model for alkali metal vapor lasers. Part II: Broadband optical pumping. *Applied Physics B: Lasers and Optics*, 112(4):507–520, 2013.

12. Masamori Endo, Ryuji Nagaoka, Hiroki Nagaoka, Toru Nagai, and Fumio Wani. Output power characteristics of diode-pumped cesium vapor laser. *Japanese Journal of Applied Physics*, 54(12):2–4, 2015.

13. Masamori Endo, Ryuji Nagaoka, Hiroki Nagaoka, Toru Nagai, and Fumio Wani. Wave optics simulation of diode pumped alkali laser (dpal). In Steven J. Davis, Michael C. Heaven, and J. Thomas Schriempf, editors, *High Energy/Average Power Lasers and Intense Beam Applications IX*, volume 9729, page 972907. SPIE, apr 2016.

14. Masamori Endo, Ryuji Nagaoka, Hiroki Nagaoka, Toru Nagai, and Fumio Wani. Scalable pump beam arrangement for diode pumped alkali lasers. In Alexei L. Glebov and Paul O. Leisher, editors, *Components and Packaging for Laser Systems IV*, number February, page 19. SPIE, feb 2018.

15. Masamori Endo, Ryuji Nagaoka, Hiroki Nagaoka, Toru Nagai, and Fumio Wani. Wave-optics simulation of diode-pumped cesium vapor laser coupled with a simplified gas-flow model. *Japanese Journal of Applied Physics*, 57(9):092701, sep 2018.

16. Boris D. Barmashenko and Salman Rosenwaks. Detailed analysis of kinetic and fluid dynamic processes in diode-pumped alkali lasers. *Journal of the Optical Society of America B*, 30(5):1118, may 2013.

17. Boris D. Barmashenko, Salman Rosenwaks, and Karol Waichman. Kinetic and fluid dynamic processes in diode pumped alkali lasers: semi-analytical and 2D and 3D CFD modeling. *SPIE Photonics West 2014-LASE: Lasers and Sources*, 8962:89620C, 2014.

18. Salman Rosenwaks, Boris D. Barmashenko, and Karol Waichman. Semi-analytical and 3D CFD DPAL modeling: feasibility of supersonic operation. *SPIE Photonics West 2014-LASE: Lasers and Sources*, 8962:896209, 2014.

19. Juhong Han, You Wang, He Cai, Wei Zhang, Liangping Xue, and Hongyuan Wang. Algorithm for evaluation of temperature distribution of a vapor cell in a diode-pumped alkali laser system: part I. *Optics Express*, 22(11):13988, jun 2014.

20. Juhong Han, You Wang, He Cai, Guofei An, Wei Zhang, Liangping Xue, Hongyuan Wang, Jie Zhou, Zhigang Jiang, and Ming Gao. Algorithm for evaluation of temperature distribution of a vapor cell in a diode-pumped alkali laser system (part II). *Optics Express*, 23(7):9508, 2015.

21. He Cai, You Wang, Juhong Han, Hang Yu, Kepeng Rong, Shunyan Wang, Guofei An, Hongyuan Wang, Wei Zhang, Liangping Xue, and Jie Zhou. Diode-pumped alkali lasers with a gradient temperature configuration. 10173:101731H, may 2017.

22. Govind P. Agrawal. *Nonlinear Fiber Optics*. Elsevier Inc., Rochester, NewYork, fifth edition, 2013.

23. Athanasios Gavrielides, L.A. (Vern) Schlie, Robert D. Loper, Michael R. Hawks, and Glen P. Perram. Analytic treatment of beam quality and power efficiency in high power transverse flow dpal. *Josa B*, 2017.

24. Anthony E. Siegman. *Lasers*. University Science Books, 1986.

25. George B. Arfken, Hans J. Weber, and Frank E. Harris. *Mathematical Methods for Physicists*. Elsiever, Oxford, seventh edition, 2013.

26. A. G. Fox and T. Li. Resonant Modes in a Maser Interferometer. *Bell System Technical Journal*, 40(2):453 – 488, 1961.

27. Anthony E. Siegman and H Y Miller. Unstable optical resonator loss calculations using the prony method. *Applied optics*, 9(12):2729–2736, 1970.

28. Cheng Yuanying, Wang Youqing, Hu Jin, and Li Jiarong. An eigenvector method for optical field simulation. *Optics Communications*, 234(1-6):1–6, apr 2004.

29. Jason Daniel Schmidt. *Numerical simulation of optical wave propagation*. SPIE, Bellingham, Washington USA, 2010.

30. Joseph W. Goodman. *Introduction to Fourier Optics*. McGraw Hill, New York, second edition, 1996.

31. Anthony E. Siegman and Edward A. Sziklas. Mode Calculations in Unstable Resonators with Flowing Saturable Gain 1:Hermite-Gaussian Expansion. *Applied Optics*, 13(12):2775, dec 1974.

32. Edward A. Sziklas and Anthony E. Siegman. Mode calculations in unstable resonators with flowing saturable gain 2: Fast Fourier transform method. *Applied Optics*, 14(8):1874, aug 1975.

33. J. P. Gordon and H Kogelnik. Equivalence Relations among Spherical Mirror Optical Resonators. *Bell System Technical Journal*, 43(6):2873–2886, nov 1964.

34. Eugene Hecht. *Optics*. Fourth edition, 2001.

35. Peter W. Milonni and Joseph H. Eberly. *Laser Physics*. John Wiley & Sons, Inc, Hoboken, New Jersey, 2010.

36. Anthony E. Siegman. Unstable optical resonators for laser applications. *Proceedings of the IEEE*, 53(3):277–287, 1965.

37. W H Southwell. Virtual-source theory of unstable resonator modes. *Optics Letters*, 6(10):487, oct 1981.

38. W. H. Southwell. Unstable-resonator-mode derivation using virtual-source theory. *J. Opt. Soc. Am*, 3(11):1885–1891, 1986.

39. Joseph T Verdeyen. *Laser Electronics*. Prentice-Hall Series in Solid State Physical Electronics. Prentice Hall, Upper Saddle River, N.J, third edition, 1995.

40. G. D. Boyd and H. Kogelnik. Generalized Confocal Resonator Theory. *Bell System Technical Journal*, 41(4):1347–1369, 1962.

41. Harry Bateman. *Tables of Integral Transforms*, volume 1. McGraw-Hill Book Company, New York, 1954.

42. Mark Fox. *Optical Properties of Solids*. Oxford Master Series in Condensed Matter Physics. Oxford University Press, New York, second edition, 2010.

43. A. Kramida, Yu. Ralchenko, J. Reader, and and NIST ASD Team. NIST Atomic Spectra Database (ver. 5.6.1), [Online]. Available: `https://physics.nist.gov/asd` [2019, July 29]. National Institute of Standards and Technology, Gaithersburg, MD., 2018.

44. Alan Gallagher. Rubidium and Cesium Excitation Transfer in Nearly Adiabatic Collisions with Inert Gases. *Physical Review*, 172(1):88–96, aug 1968.

45. J. F. Sell, M. A. Gearba, B. M. Patterson, T. Genda, B. Naumann, and R. J. Knize. Enhancement of rb fine-structure transfer in ^4he due to three-body collisions. *Optics Letters*, 35(13):2146, jun 2010.

46. Charles R. Mansfield and Edson R. Peck. Dispersion of helium. *Journal of the Optical Society of America*, 59(2):199, feb 1969.

47. David George Voelz. *Computational Fourier Optics*. SPIE, P.O. Box 10 Bellingham, Washington 98227-0010 USA, 2011.

48. T. Sean Ross. *Laser Beam Quality Metrics*. Society of Photo-Optical Instrumentation Engineers, Bellingham, Washington, first edition, 2013.

49. Anthony E. Siegman. New developments in laser resonators. In Dale A. Holmes, editor, *Optical Resonators*, volume 1224, page 2. SPIE, June 1990.

REPORT DOCUMENTATION PAGE

Form Approved
OMB No. 0704–0188

1. REPORT DATE *(DD–MM–YYYY)*	2. REPORT TYPE	3. DATES COVERED *(From — To)*
09–13–2019	Doctorate Dissertation	Sept 2016 — Sept 2019

4. TITLE AND SUBTITLE

Numerical Simulation of Unstable Laser Resonators with a High Gain Medium

5a. CONTRACT NUMBER

5b. GRANT NUMBER

5c. PROGRAM ELEMENT NUMBER

6. AUTHOR(S)

Lloyd, Robert L, Capt

5d. PROJECT NUMBER

5e. TASK NUMBER

5f. WORK UNIT NUMBER

7. PERFORMING ORGANIZATION NAME(S) AND ADDRESS(ES)

Air Force Institute of Technology
Graduate School of Engineering and Management (AFIT/EN)
2950 Hobson Way
WPAFB OH 45433-7765

8. PERFORMING ORGANIZATION REPORT NUMBER

AFIT-ENP-DS-19-S-024

9. SPONSORING / MONITORING AGENCY NAME(S) AND ADDRESS(ES)

Intentionally Left Blank

10. SPONSOR/MONITOR'S ACRONYM(S)

11. SPONSOR/MONITOR'S REPORT NUMBER(S)

12. DISTRIBUTION / AVAILABILITY STATEMENT

DISTRIBUTION STATEMENT A:
APPROVED FOR PUBLIC RELEASE; DISTRIBUTION UNLIMITED.

13. SUPPLEMENTARY NOTES

This work is declared a work of the U.S. Government and is not subject to copyright protection in the United States.

14. ABSTRACT

This research focused on the numeric simulation of unstable laser resonators with high gain media. In order to accomplish the research, the modes and eigenvalues for various bare cavity resonator were computed followed by modes of a resonator in the presence of gain. Using a Fourier Split Step Method in a Fox and Li iteration scheme, different laser outputs for various laser cavities with gain were computed. Various parameters defining positive branch confocal unstable resonators were chosen corresponding to four studies. The four studies focused on modifying laser cavity Fresnel number, gain medium parameters, gain cell position, and gain cell length from a baseline laser cavity geometry. It was observed that the highest laser cavity efficiencies occurred when the laser cavity had a Fresnel number greater than 7 and was positioned at the back larger mirror of an unstable resonator. Longer gain cell lengths were found to correspond to higher beam qualities. Beam quality was found to be inversely related to laser efficiency. A theory for modifying simple laser models based upon a mode volume was derived and supported the results of the gain wave-optic simulations.

15. SUBJECT TERMS

Unstable Resonator,Dissertation,DPAL,Mode-Fill Coefficient,Rubidium

16. SECURITY CLASSIFICATION OF:			17. LIMITATION OF ABSTRACT	18. NUMBER OF PAGES	19a. NAME OF RESPONSIBLE PERSON
a. REPORT	b. ABSTRACT	c. THIS PAGE			Dr. D.E. Weeks, AFIT/ENP
U	U	U	U	193	19b. TELEPHONE NUMBER *(include area code)* (937) 255-3636, x4561; david.weeks@afit.edu